Maritime Radar Target Detection Using Time Frequency Analysis

by

Vichet Duk

B.E. (Electronics and Communications, Honours),
The University of South Australia, 2010

M.E. (Electrical and Electronics),
The University of Adelaide, Australia, 2011

Thesis submitted for the degree of

Doctor of Philosophy

in

Electrical and Electronic Engineering
The University of Adelaide, Australia

July 2018

Supervisors:

Dr. Brian Ng,

School of Electrical & Electronic Engineering,

The University of Adelaide, Australia.

Dr. Luke Rosenberg,

Defence Science and Technology Group, Australia.

School of Electrical & Electronic Engineering,

The University of Adelaide, Australia.

THE UNIVERSITY *of* ADELAIDE

Contents

Publications

Journal Papers

V. Duk, L. Rosenberg and B. Ng, "Target Detection in Sea-Clutter Using Stationary Wavelet Transforms," *IEEE Transactions on Aerospace and Electronic Systems*, vol. 53, issue 3, pp. 1136 - 1146, June 2017.

Conference Papers

V. Duk, B. Ng and L. Rosenberg, "Adaptive Regularisation for Radar Sea Clutter Signal Separation Using a Sparse-Based Method," *International Radar Conference*, Belfast, UK, October 2017.

V. Duk, L. Rosenberg, B. Ng, Matthew Richie, Riccardo Palamà and Hugh Griffiths "Target Detection in Bistatic Radar Sea Clutter Using Stationary Wavelet Transforms," *International Radar Conference*, Belfast, UK, October 2017.

V. Duk, L. Rosenberg and B. Ng, "Target Detection in Sea-Clutter Using Stationary Wavelet Transforms," *NATO Meeting Proceedings SET-239 on Maritime Radar Surveillance from Medium to High Grazing Angle Platforms*, Edinburgh, UK, 25-26 October 2016.

V. Duk, B. Ng, and L. Rosenberg, "The potential of 2D wavelet transforms for target detection in sea-clutter," in *IEEE Radar Conference*, pp. 0901-0906, Arlington, VA, May 2015,

Abstract

Small target detection in sea clutter remains a challenging problem for radar operators as the backscatter from the sea-surface is complex, involving both time and range varying Doppler spectra with strong breaking waves which can last for seconds and resemble targets. The goal of this thesis is to investigate two different time frequency wavelet transforms to filter the sea clutter and improve target detection performance.

The first technique looks at an application of stationary wavelet transforms (SWT) to improve target detection. The SWT decomposes a signal into different components (or sub-bands) which contain different characteristics of the interference (clutter + noise) and target. A method of selecting the sub-band with the most information about the target is then presented using an 'entropy' based metric. To validate the SWT detection scheme, real radar data recorded from both an airborne and a ground based radar systems are analysed. A Monte-Carlo simulation using a cell averaging constant false alarm rate detector is implemented to demonstrate and quantify the improvement of the new scheme against unfiltered data.

The second technique utilises a sparse signal separation method known as basis pursuit denoising (BPD). Two main factors contribute to the quality of the separation between the target and sea-clutter: choice of dictionary that promotes sparsity, and the regularisation (or penalty) parameter in the BPD formulation. In this implementation, a tuned Q-factor wavelet transform (TQWT) is used for the dictionary with parameters chosen to match the desired target velocity. An adaptive method is then developed to improve the separation of targets from sea-clutter based on a smoothed estimate of the sea clutter standard deviation across range. A new detection scheme is then developed and the detection improvement is demonstrated using a Monte-Carlo simulation.

Statement of Originality

I certify that this work contains no material which has been accepted for the award of any other degree or diploma in my name, in any university or other tertiary institution and, to the best of my knowledge and belief, contains no material previously published or written by another person, except where due reference has been made in the text. In addition, I certify that no part of this work will, in the future, be used in a submission in my name, for any other degree or diploma in any university or other tertiary institution without the prior approval of the University of Adelaide and where applicable, any partner institution responsible for the joint-award of this degree.

I give permission for the digital version of my thesis to be made available on the web, via the University's digital research repository, the Library Search and also through web search engines, unless permission has been granted by the University to restrict access for a period of time.

I acknowledge the support I have received for my research through the provision of an Australian Government Research Training Program Scholarship.

	18 January 2018
Signed	Date

Acknowledgments

My PhD journey has been the experience of a life time. From the beginning, I have been very fortunate to be surrounded by many wise and supportive mentors. Their counsel has enhanced my PhD journey making it smoother and very satisfying.

Firstly, I wish to sincerely thank my supervisors, Dr Brian W.-H. Ng and Dr Luke Rosenberg for this enormous opportunity and for entrusting me to undertake this complex project. With their guidance, encouragement, enthusiasm, and support throughout my research, I have become a far more skilled researcher. Their expertise lifted my understanding of both theory and application. Thank you both also for taking time off to assist and guide my work, even after-hours when we were often at different time zones and thanks to your families for their forbearance. I am very fortunate to have you both on my team.

Thank you to Dr. Luke Rosenberg's wife, Dr. Kathrine Rosenberg, for letting me stay at their beautiful home during a conference in Crystal City, Arlington, USA and for hosting meetings at your home in Adelaide on various occasions. It was a pleasure to spend time with you and your children (Tahlia, Liam and Nicholas).

I would also like to thank the Defence Science and Technology (DST) Group for the PhD scholarship and various other funding throughout the project including travelling support. My thanks also go the University of Adelaide for the facilities and helpful staff.

With additional funding from the DST Group and the Adelaide University Graduate centre, I was able to experience a 3-month research program at the University College London (UCL) in London. At UCL, I had the privilege to work with Professor Hugh Griffiths, Dr Matthew Ritchie, Dr Ricardo Palamà and various PhD students in the radar group. I also met Professor Simon Watts at UCL who offered advice and support. I thank them for the opportunity and special thanks go to Dr Matthew Ritchie for making my stay at UCL very pleasant.

My friends and colleagues at the University of Adelaide: Garrison Gao, Robert Moric, Si Tran Nguyen Nguyen, Waddah A. Al-Ashwal, Yuexian Wang and Chow Yii Pui provided advice and encouragement throughout my PhD journey along with Nghia Nguyen Trong, Wendy Suk Ling Lee, Siti Nailah Mastura Zainarry, Madhulika Tripathi, Amir Ebrahimi, Sam Darvishi and various other visiting students from China such as Jing Xu and Qing Sun. I will miss the lunch break gatherings, sharing of ideas and thoughts at the school. I apologise if I have omitted the names of others who helped me along the way.

Special thanks to my family (parents and my 6 brothers and sisters) in Cambodia, my extended family in Melbourne, Australia and to my dear friends Chris, Winston, Nash and Zhongyu for their support, encouragement, generosity and their eternal tolerance of my eccentricities.

Last but not least, I thank my foster father, Ron Davies, whose unconditional love, support, encouragement and belief in me enabled me to achieve not only this PhD but all my endeavours since commencing undergraduate study. Without your support in every aspect, I would not have achieved as much as I have.

Thesis Conventions

The following conventions have been adopted in this Thesis:

Typesetting

This document was compiled using LaTeX2e. TeXstudio was used as text editor interfaced to LaTeX2e while Inkscape was used to produce schematic diagrams and other drawings.

Referencing

The IEEE style has been adopted for the referencing.

System of units

The units comply with the international system of units recommended in an Australian Standard: AS ISO 1000–1998 (Standards Australia Committee ME/71, Quantities, Units and Conversions 1998).

Spelling

Australian English spelling conventions have been used, as defined in the Macquarie English Dictionary (A. Delbridge (Ed.), Macquarie Library, North Ryde, NSW, Australia, 2001).

Abbreviations

List of Acronyms in the Thesis

1D, 2D	One, Two Dimensional
ADC	Analogue to Digital Converter
AMP	Approximate Message Passing
BPD	Basis Pursuit Denoising
CA-CFAR	Cell Averaging Constant False Alarm Rate
CAMP	Complex Approximate Message Passing
MCA	Morphological Component Analysis
CCDF	Complementary Cumulative Distribution Function
CFAR	Constant False Alarm Rate
CNR	Clutter to Noise Ratio
CNR_r	Clutter to Noise Ratio plus Rayleigh power
CPI	Coherent Processing Interval
CWT	Continuous Wavelet Transform
DWT	Discrete Wavelet Transform
EM	ElectroMagnetic
FFT	Fast Fourier Transform
GPS	Global Position Satellite
GPSDO	Global Position Satellite Disciplined Oscillators
HH	Horizontally transmitted and Horizontally received polarisation
HV	Horizontally transmitted and Vertically received polarisation
IF	Intermediate Frequency
ISTA	Iterative Shrinkage-Thresholding Algorithm
LS	Least Squares
MGA	Medium Grazing Angle
ML	Maximum-Likelihood
MoM	Method of Moments
NetRAD	Netted RADar
PDF	Probability Density Function
PSD	Power Spectral Density

RCS	Radar Cross Section
RF	Radio Frequency
SALSA	Split variable Augmented Lagrangian Shrinkage Algorithm
SNR	Signal to Noise Ratio
SIR	Signal to Interference Ratio
STFT	Short Time Fourier Transform
STD	Standard Deviation
SWT	Stationary Wavelet Transform
TQWT	Tunable Q-factor Wavelet Transform
T/R	Transmit/Receive
UAV	Unmanned Aerial Vehicle
UCL	University College London
UoA	University of Adelaide
UCT	University of Cape Town
VH	Vertically transmitted and Horizontally polarisation
VV	Vertically transmitted and Vertically received polarisation
WT	Wavelet Transform

Nominal Radio Frequency Bands

HF	3 MHz - 30 MHz
VHF	30 MHz - 300 MHz
UHF	300 MHz - 1 GHz
P-band	300 MHz - 350 MHz
L-band	1 GHz - 2 GHz
S-band	2 GHz - 4 GHz
C-band	4 GHz - 8 GHz
X-band	8 GHz - 12 GHz
Ku-band	12 GHz - 18 GHz
K-band	18 GHz - 27 GHz
Ka-band	27 GHz - 40 GHz
V-band	40 GHz - 75 GHz
W-band	75 GHz - 110 GHz
mm-band	110 GHz - 300 GHz

Symbols

List of Symbols in the Thesis

a	Wavelet transform (WT) scale parameter
a_0	Integer number relating to wavelet scale
α	Tuneable Q-factor wavelet transform (TQWT) low-pass scaling parameter
$\mathbf{A}$	Degradation operation (or dictionary) of a transform
A_k	WT approximate sub-band
$\tilde{A}_k$	Reconstructed WT approximate sub-band
A_e	Antenna aperture effective area
b	Translation parameter of a continuous wavelet transform (CWT)
B	Signal bandwidth
b_0	Integer number relating to time shift
β	TQWT high-pass scaling parameter
β_{bi}	Bistatic angle
c	Speed of light
C_ψ	Admissibility condition function
Δ_t	Time interval
Δ_ω	Frequency interval
D_k	WT detail sub-band at scale (or level) k
$\tilde{D}_k$	Reconstructed detail sub-band at level k
$\mathbf{e}$	Unknown noise (or error term)
E	Complex-value backscatter
E_b	Entropy (absolute value) of a reconstructed sub-band with zero mean
E_i	In-phase backscatter component
E_q	Quadrature backscatter component
η	Constant (used for determining penalty parameter)
F	Target fluctuation
$f(t)$	Time domain signal or function
$F(\omega)$	Spectal or frequency domain signal

f_c	Filter cut-off frequency
f_r	Received target frequency
f_t	Transmitting (or carrier) frequency
G	Antenna gain
γ	Threshold
γ_b	Maximum entropy of reconstructed sub-band: b
$\Gamma(.)$	Gamma function
g_a	Impulse response of the analysis high-pass filter
G_a	z-domain impulse response of the analysis high-pass filter
g_s	Impulse response of the synthesis high-pass filter
G_s	z-domain impulse response of the synthesis high-pass filter
G_r	Antenna (receiving) directive gain
G_t	Antenna (transmitting) directive gain
$g(x_q)$	Probability density function (PDF) of the data x_q
H_0	Interference only hypothesis
H_1	Target with interference hypothesis
h_a	Impulse response of the analysis low-pass filter
H_a	z-domain impulse response of the analysis low-pass filter
h_s	Impulse response of the synthesis low-pass filter
H_s	z-domain impulse response of the synthesis low-pass filter
HH_k	High-pass filtering along row and column (or detail) sub-band of the 2 dimensional (2D) stationary WT (SWT) at level-k
$\tilde{HH}_k$	Reconstructed HH_k sub-band at level-k
HL_k	High-pass filtering along row and low-pass filtering along column (or vertical) sub-band of the 2D SWT at level-k
$\tilde{HL}_k$	Reconstructed HL_k sub-band at level-k
$H(X)$	Entropy of a discrete random variable, X
j	Imaginary unit of a complex-value function or signal
k	Constant (decomposition level of discrete wavelet transforms (DWT))
k_r	Influence factor due to Rayleigh component
K	Constant (target Swerling case)
$K_v(.)$	Modified Bessel Function
L	Loses in radar equation (including two-way propagation loss)
L_1	Finite absolute value
L_2	Finite energy

l_q	Lower limits of a histogram bin
$\langle\,\rangle$	Average value or mean operator
$\langle\,,\,\rangle$	Inner product
λ	Penalty parameter
λ_0	A constant offset for the penalty parameter
λ_c	Wavelength
LH_k	Low-pass filtering along row and high-pass filtering along column (or horizontal) sub-band of the 2D SWT at level-k
$\tilde{LH}_k$	Reconstructed LH_k sub-band of the 2D SWT at level-k
LL_k	Low-pass filtering along row and column (or approximate) sub-band of the 2D SWT
$\tilde{LL}_k$	Reconstructed LL_k sub-band of the 2D SWT
l_q	Lower limits of a histogram bin
M	Sample in slow time (pulses or looks)
M_r	Sample in fast time (or in range)
μ_ω	Mean frequency
μ_t	Mean time
ν	Shape parameter of a PDF
$\|\cdot\|_1$	ℓ_1-norm, the sum of absolute values of the vector elements
$\|\cdot\|_2$	ℓ_2-norm, the sum of the element squares and referred to as the 'energy'
ω	Angular frequency
$P(\,)$	Probability density function
P_A	Interference PDF
p_c	Mean clutter power
P_d	Probability of detection
P_fa	Probability of false alarm
p_n	Thermal noise mean power
p_q	Probability of a histogram bin
p_r	Rayleigh mean power from the K+Rayleigh model
P_r	Radar received signal power
ψ	Wavelet function
Ψ	Fourier transform of ψ
ϕ	Scaling function
$\mathbf{\Phi}$	Matrix (or dictionary) corresponding to the TQWT
P_t	Radar transmitted power
P_T	Interference and target PDF

Q	Q-factor of TQWTs
Q_E	Number of histogram bin interval
R	Radial distance
$\mathbf{R}$	Signal residue after Basis Pursuit Denoising (BPD)
$\mathbb{R}$	Real number
$\mathbb{R}^+$	Real positive number
r	Redundancy factor of TQWTs
R_r	Receiving range from a target
R_t	Transmitting range to a target
s	Summation of the target power
S	Target SIR over M pulses in square law detector
σ_r	Standard deviation at range bin r^{th}
t	Fast time
t_0	Time delay for a reflected target
A^T	Transpose of a vector or matrix A
T_w	Width of the window function
u_q	Upper limits of a histogram bin
v	Target velocity
V_k	Vector subspace at scale k
σ	Radar cross section
W_f	CWT coefficients
W_k	Wavelet subspace at scale k
w_q	Width of the histogram bin for the q^{th} term (bin)
x	Input signal (or radar backscatter)
$\mathbf{X}$	Target signal after BPD
$X(\omega)$	Frequency domain of signal x
x_0	Variance of speckle radar return with zero mean
x_r	Rayleigh mean power
y	Speckle envelope
$\mathbf{Y}$	Radar echoes consisting of target $\mathbf{X}$ and residue $\mathbf{R}$
$\mathbf{y}$	Under-determined linear system
$Y(\omega)$	Frequency domain of signal y
z	Radar backscatter intensity
$\mathbb{Z}$	Integer

List of Figures

List of Tables

Chapter 1

Introduction

THIS introductory chapter provides a brief overview of current maritime radar research challenges and common techniques for target detection in sea-clutter. Signal processing methods using time-frequency techniques are outlined. Chapter summaries and contributions of the thesis are then given.

1.1 Overview

Radar is an acronym for **Ra**dio **D**etection **A**nd **R**anging which was initially used to detect objects and measure their range. It was originally invented during World War II for defence purposes such as an early warning and surveillance using radio (or electromagnetic) waves as a replacement for visual detection [84, 104, 107, 124]. Radar is able to detect targets in a dark environment and at longer distances which is not possible with optical sensors. With modern and advanced electronic technology, radar has been further developed for other defence purposes such as missile guidance, target classification and imaging in real time. For the civilian domain, radar has become an important and commonly used technology with applications including weather forecasting, vehicle speed measurement, air traffic control and self-driving cars. It is also used in space exploration and in the health care industry for fall detection [7, 57].

For surveillance of the seas and oceans, radar can be used for emergency search and rescue operations, tracking people smugglers, measuring sea conditions and coastal monitoring. Moreover, ship navigation is made safer with this type of radar especially when travelling at night or in limited invisibility. It is also very important for defence purposes in a country such as Australia which is surrounded by sea.

The recorded radar echoes from an illuminated patch of the sea surface is known as sea-clutter. The sea-surface consists of various components including breaking waves, wind waves and gravity waves or swell. The dynamic variation of the surface components and the interactions between the sea-surface and the incident electromagnetic waves are complex. Moreover, various components in the measured radar echoes can exhibit target-like characteristics. Therefore, detection of small targets in sea-clutter can be challenging and is still an active research area [4, 47, 64, 87, 124].

In maritime radar operations, target detection is typically implemented in either the range / time or range / frequency domains. Detection in the range / time domain does not require phase information and is known as non-coherent detection, while detection in the range / frequency domain utilises the phase information and is known as coherent detection. Due to sea-surface variations, the frequency (Doppler) spectrum of sea-clutter spreads broadly and varies in range. As a result, non-coherent detection is more commonly used for maritime radar target detection.

In non-coherent detection, a detection is declared if the radar backscatter is greater than a set threshold. The threshold is usually adaptive and the desired false alarm rate is constant. A common and widely used non-coherent detection scheme is a sliding window cell-averaging

false alarm rate (CA-CFAR) algorithm, whose threshold is varied with the local clutter around the cell under test. To determine the threshold in the CA-CFAR algorithm, an amplitude statistical model (expressed as a probability density function (PDF)) is often used to represent the background radar backscatter. A well-matched model enables a more accurate setting of the threshold and can achieve the desired false alarm level. If there is a mismatch, the detection scheme will perform badly with targets being missed or the number of false alarms becoming too high. In this case, maritime radar target detection can be unreliable [4, 87, 94, 119, 124].

There have been many efforts to accurately model the PDF of the background sea-clutter. Some common models include the log-normal [113], Weibull [44] and K-distribution [52]. However, in many cases, they are still unable to capture the high magnitude and long tail components of the sea-clutter [93].

The main contributor to the long tail in the sea-clutter PDF is sea-spikes [87]. Sea-spikes are characterised by high intensity returns caused by breaking waves on top of the sea-surface. There are two types of breaking waves: some lasting for a short time before disappearing and others persisting for seconds. Those belonging to the second type are commonly mistaken for targets as they exhibit many of the same characteristics [64, 87, 124]. This thesis proposes different approaches to improve maritime radar target detection. Time-frequency methods based on wavelet transforms are used to process the sea-clutter prior to performing target detection, to reduce the impact caused by sea-spikes and to improve the detection performance.

1.2 Thesis Motivation

The sea-surface fluctuates with changes in the environment due to wind, currents and other naturally occurring phenomena. The sea-clutter characteristics therefore vary with time, resulting in non-stationary returns.

To improve the performance of small target detection in non-stationary sea-clutter, a number of signal processing techniques have been investigated. These include frequency [88, 127], joint time-frequency [28, 35, 37, 75, 77] and fractal analysis [13, 14, 63, 69]. In the frequency domain, fast moving targets can easily be distinguished and detected. However, the sea-clutter has a broad Doppler spectrum which can mask the target [88, 127].

The non-stationary nature of sea-clutter has led researchers to use joint time-frequency analysis for target detection. Time-frequency analysis methods include the short time Fourier transform (STFT) [46], wavelet transform (WT) [26, 67, 68, 72] and the Wigner-Ville distribution [118,

130]. The short time Fourier transform processes small segments in time with a fixed window. The wavelet transform, on the other hand, uses window functions that vary with frequency and represents a signal at different scales (resolutions). The wavelet transform can then be used to filter unwanted components in the signal while preserving the important information [68, 81]. These properties make the wavelet transform more suitable for analysing non-stationary sea-clutter [29]. Wavelet transforms have been used for signal processing in various applications to extract time-frequency information of non-stationary signals [27, 67, 76]. In radar signal analysis, the WT has been used to suppress interference and enhance small target detection [29, 39, 112, 114, 121, 133].

Another method which has been used to enhance sea-clutter target detection is the fractal analysis. Fractals are associated with the geometrical properties of sea-surface. They were first introduced for radar signal analysis by Lo et al. [63] who proposed that the sea surface can be represented by a fractal set. The method has since been studied further to gain a theoretical basis for the use of the fractals in radar data analysis [12–14]. The fractal dimension of a time series is estimated either using the box dimension or through spectral analysis. The fractal dimension results in variation if there is a target present in the clutter. By setting an appropriate threshold, the target can be detected when the fractal dimension decreases below a certain level [69]. However, the variation of the fractal dimension is quite small when the target is present and variation of fractal dimensions may also be caused by sea-spikes.

Based on the previous research, wavelets offer a more promising method among the time-frequency representations. In this thesis, various wavelet transforms will be used to improve target detection performance in sea-clutter.

1.3 Thesis Outline and Contributions

The goal of this thesis is to use time-frequency analysis with wavelets to improve detection performance of small targets in sea-clutter. In order to develop an effective detection scheme, the differences in sea-clutter and target characteristics must be well understood. Chapter 2 provides an overview of the different components of sea-clutter and how they relate to the sea-surface components. A conventional detection method is then outlined as a benchmark for comparing the new schemes. In Chapter 3, different time-frequency methods are then described.

The new detection schemes are presented in Chapters 4-6 using real radar data from two different radar systems. The first technique uses stationary wavelet transforms (SWT). Once applied to the data, the components of the interference and target (if present) generally have

different distributions across sub-bands. By isolating and reconstructing the sub-band with the strongest signal to interference ratio (SIR), we can improve the detection performance.

Radar target detection in the maritime domain requires the returned backscatter from the target to be distinguishable from the background interference (sea clutter and noise) [124]. Over a short time period, targets typically have a constant radial velocity. Sea clutter on the other hand varies with the environmental conditions and contains a complex time and range varying Doppler spectrum. The second detection technique uses a resonance based sparse signal separation, which has recently been applied to this problem with promising results [36, 43, 75, 77]. Achieving good separation of the target relies on two main factors: an appropriately chosen transform that encourages a sparse representation and the regularisation (or penalty) parameter in the optimisation algorithm. In this work, a resonance based transform, the tuned Q-factor wavelet transform (TQWT), is used as the dictionary with its oscillation tuned to match different target characteristics [99, 100]. Following on from related work [75], we choose appropriate parameters for a target and look further at the selection of the penalty parameter. An adaptive method is proposed to improve the separation of targets from sea-clutter based on a smoothed estimate of the sea clutter standard deviation across range. A new detection scheme is developed and a Monte-Carlo simulation is used to demonstrate the detection improvement.

The main contributions of this thesis are:

- **Stationary wavelet transform sub-band detection**

  A novel method that highlights different components (or sub-bands) of the data is developed. By isolating and reconstructing different sub-bands of the SWT, the SIR of the target is improved. A sub-band selection scheme using 'entropy' as a metric is then implemented to select the sub-band with the most information about the target. The new detection scheme is then validated with real radar data and a large detection improvement is achieved over unprocessed data. A comparison of performance using both 1 dimensional (1D) and 2 dimensional (2D) SWTs is also performed. It is found that the 1D SWT provides better relative detection performance than the 2D SWT. This contribution is investigated and demonstrated in Chapter 4.

- **Bistatic detection analysis using stationary wavelet transforms**

  We apply the SWT detection scheme developed in Chapter 4 to simultaneously compare the monostatic and bistatic data with different 'bistatic angles'. The improved detection results using a different radar system confirms the robustness of the scheme. The analysis and required modifications to the scheme are demonstrated in Chapter 5.

- **Sparse signal separation using a tuned Q-factor wavelet transform**
  We develop a novel detection scheme based on a sparse signal separation technique using a tuned Q-factor wavelet transform (TQWT). The sparse signal separation is achieved using a method known as basis pursuit denoising (BPD), where a TQWT is used as the dictionary with parameters chosen to match the desired target velocity. An adaptive method is developed to improve the separation of targets from sea-clutter based on a smoothed estimate of the sea clutter standard deviation across range. A detection scheme is then demonstrated using a Monte-Carlo simulation. This contribution is presented in Chapter 6.

1.4 Chapter Summaries

- **Chapter 2 - Maritime Radar Background**
  This chapter describes the operation of maritime radar and the different components of the sea-clutter. The PDFs of both sea-clutter and targets are discussed and the non-coherent cell averaging constant false alarm rate (CA-CFAR) detection scheme is outlined. The chapter also includes details of two radar data sets. The first was recorded by the Defence Science and Technology (DST) Group using the Ingara radar system on two consecutive trials in 2004 and 2006. The second data set was collected in 2010 by a team from the University College London (UCL) and the University of Cape Town (UCT) using the NetRAD radar system. The data from those systems and trials are used for testing the proposed detection methods.

  The main contribution of the chapter is to present a condensed summary of the relevant background on maritime radar, sea-clutter analysis and modelling, a conventional CFAR detection algorithm and the radar data sets.

- **Chapter 3 - Time Frequency Analysis**
  This chapter provides a description of relevant time-frequency analysis techniques including the Fourier transform, short time Fourier transform, wavelet transform and the tuned Q-factor wavelet transform. The Fourier transform is suitable for analysing stationary signals, but is not suitable for non-stationary sea-clutter. Instead, time-frequency analysis techniques such as wavelet transforms should be used. Similarly, the tuned Q-factor wavelet transform can tune the window function to a desired shape and fluctuation, offering better analysis of the non-stationary signal.

The main contribution of the chapter is to provide a condensed summary of the relevant background on time-frequency techniques used in the subsequent chapters.

- **Chapter 4 - Target Detection in Sea-Clutter Using Stationary Wavelet Transforms**
  This chapter investigates target detection using both 1D and 2D SWTs. Each decomposition level of the SWT produces multiple sub-bands which can highlight or suppress different features of the sea-clutter. The chapter also explores and incorporates information across different levels of the SWT decomposition to further improve the detection performance. To determine which sub-band contains the most information about a target, an efficient indication scheme using entropy is proposed. The scheme is used to guide the choice of sub-bands in the proposed detector. A Monte-Carlo simulation is used to demonstrate the detection improvement.

  The main contribution of this chapter is the development of a new detection scheme using SWTs. The first part investigates the detection performance using 1D and 2D SWTs. The second part of the chapter proposes a scheme for selecting which wavelet sub-band contains the most information about the target without prior knowledge of the target velocity. The new scheme provides improved detection performance over the unprocessed data with a range of target velocities.

- **Chapter 5 - Target Detection in Bistatic Radar Sea Clutter Using Stationary Wavelet Transforms**
  In this chapter, the new SWT detection method derived in the previous chapter is modified to suit the NetRAD bistatic radar data. The chapter also gives a comprehensive analysis and detection comparison between monostatic and bistatic data from the NetRAD system.

  The main contributions of this chapter are to examine the robustness of the SWT detection scheme on different data sets and to provide an analysis of detection performance from both monostatic and bistatic data.

- **Chapter 6 - Target Detection in Sea Clutter Using Resonance Based Sparse Signal Separation**
  In this chapter, a resonance-based sparse signal separation method using the TQWT is introduced. Using appropriate parameters of the TQWT matched to the target velocity, the chapter investigates the impact of the regularisation (or penalty) parameter in the BPD algorithm. An adaptive penalty parameter is then proposed which dynamically adapts to the sea-clutter. A large improvement in the detection is demonstrated with a Monte-Carlo simulation.

The main contribution of this chapter is the development of a new detection scheme based on a resonance based sparse signal separation algorithm with an adaptive penalty parameter. Using Monte Carlo simulations, the new scheme shows improved detection performance.

- **Chapter 7 - Conclusion**
  This chapter summarises the main contributions and achievements presented in the thesis. Future work to further improve small target detection in sea-clutter is also described.

Chapter 2

Maritime Radar Background

THIS chapter provides background to the thesis and covers an overview of radar, the different characteristics of sea-clutter, sea-clutter modelling and a non-coherent detection method known as the cell-averaging constant false alarm rate algorithm. The chapter also includes details of two radar data sets. The first was collected by the Defence Science and Technology Group using the Ingara radar system on two consecutive trials in 2004 and 2006. The second data set was collected in 2010 by a team from the University College London, UK and the University of Cape Town, South Africa using the NetRAD radar system. The data from these two radar systems are used for testing the proposed detection methods.

2.1 Radar Introduction

2.1.1 Radar Fundamentals

Radar is the process of emitting radio frequency (RF) waves (or signals) toward a scene. Part of that energy will then reflect back when the signal encounters an object. Since the electromagnetic wave travels at the speed of light, c, the time required for the total two-way path is $t_0 = \frac{2R}{c}$. If there is a target as shown in Figure 2.1, the range is given by

$$R = \frac{ct_0}{2}. \tag{2.1}$$

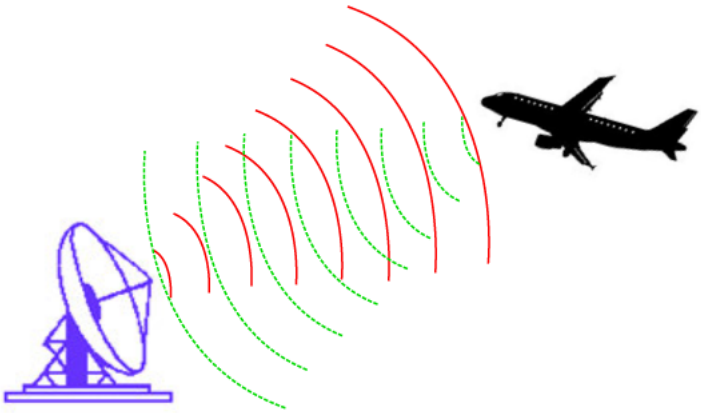

Figure 2.1. Illustration of radar emitting EM waves (red) and receiving (green) after reflecting off a target at a range, R.

In the returned signal, there always exists background interference. If this is stronger than the target signal, detection can be difficult. Interference is defined as any unwanted signals received by the radar system including [84]:

- Noise (internal to the radar and external),
- Reflections from unwanted sources (also known as clutter),
- Unintentional RF energy from other sources,
- Intentional RF energy (known as jamming) including noise or false targets.

Radar applications include remote sensing, air-traffic control, law enforcement and highway safety, ship safety and navigation, emergency search and rescue and space operations [104]. For surveillance or remote-sensing applications, radars typically operate between 1-18 GHz which is in the microwave frequency region [59, 84, 104].

2.1.2 Radar System Block Diagram

A basic block diagram of a radar is shown in Figure 2.2. It consists of an antenna, transmitter, receiver, duplexer and signal processing / detection processor [59]. The RF energy is emitted by the transmitter through the antenna into free space. The duplexer, which contains a circulator or transmit/receive (T/R) switch, isolates the operation between the system transmitter and receiver. The receiver amplifies and samples the received signal via an analogue to digital converter. The output is then fed into the signal processor and detection stage. The focus areas of this thesis are the blocks shaded in grey.

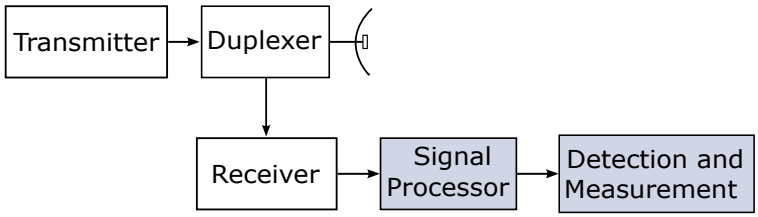

Figure 2.2. Illustration of the major elements in a monostatic radar system. The elements highlighted in dark grey are the focus areas of this thesis.

2.1.3 Radar Range Equation

The radar range equation is used to determine the returned power. The received signal power, P_r, is given by [104, 124]:

$$P_r = \frac{P_t G_t}{4\pi R_t^2} \times \frac{1}{L} \times \frac{\sigma}{4\pi R_r^2} \times A_e \tag{2.2}$$

where the term $\frac{P_t G_t}{4\pi R_t^2}$ is the power density (or power per unit area) at distance R_t from the radar and P_t is the transmitted power with gain G_t. The term L covers all losses in the radar and the two-way propagation loss. The term $\frac{\sigma}{4\pi R_r^2}$ is the effective scattering of the target radar cross section (RCS) σ. The RCS of an object is commonly a complex function of aspect angle,

frequency, and polarisation [28, 64, 84]. And finally, A_e is the effective area where the power is collected at the receiving antenna.

For a radar having wavelength λ_c and antenna aperture effective area A_e (in square metres), the antenna gain is given by:

$$G_t = \frac{4\pi}{\lambda_c^2} A_e. \tag{2.3}$$

The radar equation for monostatic radar having a common antenna for both transmitting and receiving then becomes:

$$P_r = \frac{P_t G_t^2 \lambda_c^2 \sigma}{(4\pi)^3 R^4 L}. \tag{2.4}$$

2.1.4 Doppler Shift

For a monostatic radar, the transmitter and receiver are at the same location and do not move with respect to one another. If a scatterer in the radar illuminated area travels with velocity v towards the radar, then the radar transmitted frequency f_t and received frequency f_r has the relation:

$$f_r = \left(\frac{1 + v/c}{1 - v/c}\right) f_t, \tag{2.5}$$

which is known as the Doppler shift [84].

2.2 Maritime Radar and Sea Clutter

Maritime radars can be airborne or operated from a cliff top or a surface-ship as shown in Figure 2.3. For defence purposes, they are used to safeguard the coastline and detect people smugglers, illegal fishing and drug runners. For the civil operations, they are used primarily for shipping navigation to avoid collisions with other vessels and for search and rescue operations.

The dielectric constant of sea water is high and depending on the radar operating frequency, the reflections from the sea are generally strong. The sea-surface backscatter has been extensively studied to gain insights of its complex nature. However, the analysis is difficult due to unpredictable changes of the sea-surface.

2.2.1 Sea Surface Components

Sea clutter is influenced by the evolving nature of the ocean surface and the environment [64, 94, 124]. The main components can be categorised into gravity waves and capillary waves [94, 124].

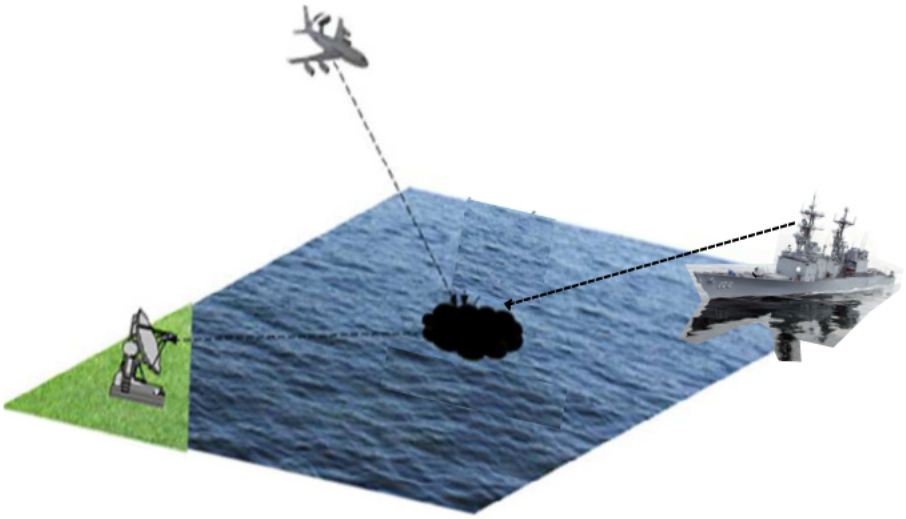

Figure 2.3. Maritime radar platforms.

- The gravity waves are large scale structures which are controlled by the gravity force and these types of waves can travel long distances with long wavelengths. Long [64] states that the large scale waves on the ocean surface are comprised of two components: sea and swell. Sea waves are composed of relatively steep, short-crested waves produced and driven by wind. Swell, on the other hand, is the wave system that persists after the wind has abated. They have sinusoidal-like waves with large wavelength and do not necessarily travel in the same direction as the wind [64, 124].

- Capillary waves are the result of tension on the sea-surface creating surface ripples. These type of waves have much shorter wavelengths on the order of a few centimetres or less [64]. Capillary waves are mainly driven by the local wind whose energy is being pushed onto the ocean surface causing surface stress and short crested waves to break. The wave length then increases, resulting in wind waves that increase with fetch and duration [124, 131].

The sea-state can be categorised in terms of the wave height [64, 124]. One of the popularly used scales is the Douglas sea-state shown in Table 2.1.

Table 2.1. Douglas sea state in metric units. The table is reproduced from [94].

Sea state	Description	Wave Height (m)	Wind Speed (m/s)	Fetch (km)	Duration (h)
1	Smooth	0.0-0.3	0.0-3.1	-	-
2	Slight	0.3-0.9	3.1-6.2	93	5
3	Moderate	0.9-1.5	6.2-7.7	222	20
4	Rough	1.5-2.4	7.7-10.3	278	23
5	Very rough	2.4-3.7	10.3-12.9	370	25
6	High	3.7-6.1	12.9-15.4	556	27
7	Very high	6.1-12.7	15.4-25.7	926	30
8	Precipitous	>12.2	>25.7	1296	25

2.2.2 Sea Surface Normalised Radar Cross Section

The sea clutter is generally characterised by the normalised radar cross section (NRCS). The NRCS will vary depending on the grazing-angle, wind direction, sea-state, radar frequency and waveform. Since the sea-clutter is always present in maritime radar operations, it is important to understand the characteristics of the clutter returns in order to develop effective signal processing strategies and detection schemes.

Sea-Surface Scattering Models

The characteristics of radar backscatter are greatly influenced by the sea surface components and there has been a number of theoretical models proposed to describe them. Capillary waves are typically associated with Bragg resonance which occurs when the radar wavelength matches the wavelength of the surface waves. However, this model does not explain the effects of the swell and breaking waves [124].

The two-scale composite surface model is an extension to this model and is based on geometric and perturbation theory which comprises both large and small scale components of the surface roughness [48, 116, 132].

To justify the two-scale model, Valenzuela and Laing [115] proposed a physical description of the sea-surface using hydrodynamic models. Their explanation was that short gravity and capillary waves are superimposed on longer wavelength gravity waves, with the scattering changing with the local surface slope relative to the radar.

Sea Spikes

A number of theories have been proposed to understand the dynamics of sea-clutter having non-Bragg scattering [38, 54, 61, 128]. Commonly, this type of scattering is referred to as sea spikes which are primarily associated with breaking waves. Ward et al. [124] describe sea clutter with spiky behaviour as having three main types of scattering events: Bragg resonant-scattering, whitecap scattering and specular (burst) scattering. The whitecap scattering often lasts for seconds and is referred to as 'persistent' sea spikes, while specular scattering often appears for a short period of time and is referred to as 'discrete' sea-spikes. Moreover, the specular sea-spikes are likely to have a narrow Doppler spectrum and be stronger in the horizontal polarisation when looking into the waves.

Another definition by Lee [60] is that there are three possible factors contributing to non-Bragg scattering. The first includes a wave which is about to break and has a much longer wavelength than the Bragg resonance wave. The second is when there is a breaking wave and the return is large. The last factor is due to attenuation in the VV polarisation caused by Brewster angle damping which results in the HH polarisation having a greater contribution than multipath scattering and shadowing from large wave crests over wave troughs.

2.3 Probability Distribution

For a coherent radar, the backscatter is captured in complex form with in-phase and quadrature components. However for non-coherent detection, the phase information is lost because only the envelope (or magnitude) of the received signal is used. When implementing the detection, a statistical (or probability density function (PDF)) model is commonly used to represent the sea-clutter amplitude or intensity distribution [124].

There have been a number of models presented in the literature with different degrees of success [90] including the Rayleigh, Log-normal, Weibull, K, Pareto and K-distribution with a Rayleigh component (K+Rayleigh). The radar return from many small structures is referred to as speckle. Together with the thermal noise, the radar return is defined by a Gaussian distribution:

$$P(E_i, E_q | x_0, p_n) = \frac{1}{\pi(x_0 + p_n)} \exp\left[\frac{-(E_i^2 + E_q^2)}{x_0 + p_n}\right] \qquad -\infty \leq E_i, E_q \leq \infty \tag{2.6}$$

where x_0 is the speckle mean power and p_n is the thermal noise power and E_i and E_q are the in-phase and quadrature samples at the receiver. The envelope of the returned components is

$E = \left(E_i^2 + E_q^2\right)^{\frac{1}{2}}$ and is represented by a Rayleigh distribution:

$$P(E|x_0, p_n) = \frac{2E}{x_0 + p_n} \exp\left[\frac{-E^2}{x_0 + p_n}\right]; \qquad 0 \leq E \leq \infty \tag{2.7}$$

where the average value of E is $\langle E \rangle = \frac{\sqrt{\pi(x_0+p_n)}}{2}$ and the mean square is $\langle E^2 \rangle = x_0 + p_n$.

Typically a square law is used for the detection analysis where the power (or intensity), $z = E^2$ is used and the speckle distribution becomes exponential,

$$P(z|x_0, p_n) = \frac{1}{x_0 + p_n} \exp\left[-\frac{z}{x_0 + p_n}\right] \qquad 0 \leq z \leq \infty. \tag{2.8}$$

In many detection schemes, the performance generally improves by summing the intensity over a number of pulses or looks. If we assume M is the number of independent looks, then

$$z = \sum_{m=1}^{M} y_m^2. \tag{2.9}$$

The received power is then characterised by a gamma PDF,

$$P(z|x_0) = \frac{z^{M-1}}{(x_0 + p_n)^M \Gamma(M)} \exp\left[-\frac{z}{x_0 + p_n}\right] \tag{2.10}$$

where $\Gamma(.)$ is the gamma function.

2.3.1 Compound K-Distribution

The K-distribution was first introduced by Jakeman and Pusey [52] in 1976 in the field of lasers and later Ward [123] applied the model to sea-clutter in 1981. The distribution consists of two main components contributing to the sea-surface fluctuations. The first is speckle, the scattering from small structures on the sea surface. The second component is texture and is related to the swell and long gravity waves. The speckle is commonly described as resulting from many random scatterers which exhibit Gaussian statistics [124]. The PDF of these returns is modelled by a Rayleigh distribution in the magnitude domain or an exponential distribution in the intensity domain as shown in Equation (2.8). For a K-distribution, the texture x_0, is modelled by a gamma distribution,

$$P(x_0) = \frac{b^\nu}{\Gamma(\nu)} x_0^{\nu-1} \exp(-b x_0), \quad b, \nu > 0 \tag{2.11}$$

where ν is the shape, $b = \frac{\nu}{p_c}$ is the scale and p_c is the mean clutter power. If thermal noise is ignored ($p_n = 0$) then the K-distribution is given by

$$P(z) = \int_0^\infty P(z|x_0)P(x_0)\mathrm{d}x_0 \tag{2.12}$$

$$= \frac{2b^{\frac{\nu+1}{2}} z^{\frac{\nu-1}{2}}}{\Gamma(\nu)} K_{\nu-1}\left(2\sqrt{bz}\right). \tag{2.13}$$

where $K_{\nu-1}(.)$ is the modified Bessel Function of the second kind with order $\nu - 1$. For the K-distribution of sea-clutter with thermal noise, the overall PDF becomes:

$$P(z) = \frac{2zb^\nu}{\Gamma(\nu)} \int_0^\infty \frac{x_0^{\nu-1}\exp(-bx_0)}{x_0 + p_n} \exp\left(\frac{-z}{x_0 + p_n}\right) \mathrm{d}x_0, \quad -\infty < z < \infty \tag{2.14}$$

However in many cases, the model does not fit the data well in the tail of the distribution which is possibly due to the existence of sea-spikes [4, 31, 42, 89, 94, 124]. Other distributions have therefore been proposed including the KA [73], KK [31, 91], K+Rayleigh [93] and Pareto [42, 89] with different degrees of improvement.

2.3.2 K+Rayleigh Distribution

Rosenberg et al. [93] extended the K+noise distribution to capture both noise and any extra Rayleigh components. Moreover, the K-distribution with Rayleigh component (K+Rayleigh distribution) is shown to represent the data extremely well for medium grazing angle clutter compared to both the Pareto and the K-distribution plus noise. The experimental results are illustrated in [93]. The K+Rayleigh distribution has an additional Rayleigh component, p_r, with the speckle mean given by $x_0 = x_r + p_r$. Equation (2.8) can then be written as

$$P(z|x_r) = \frac{1}{x_r + p_n + p_r} \exp\left[\frac{-z}{x_r + p_n + p_r}\right]. \tag{2.15}$$

To calculate the compound integral in Equation (2.13), the integration is then performed with the modified speckle mean level x_r instead of the speckle, x_0. The scale $b_r = \frac{\nu_r}{p_c}$ where $\nu_r > 0$ shape of the K+Rayleigh distribution. The PDF of the K+Rayleigh distribution has no closed-form expression and is solved by integrating Equation (2.13) with respect to the modied speckle mean level, x_r instead of the total speckle x_0.

The influence of the extra Rayleigh component can be measured by computing the ratio of the mean of the Rayleigh component to the mean of the gamma distributed component of the clutter (p_c) and is defined by

$$k_r = \frac{p_r}{p_c}. \tag{2.16}$$

2.3.3 Parameter Estimation

For the K-distribution, the parameters to estimate are the scale and shape. A high shape parameter implies that the data is less spiky [35, 124]. Various methods can be used to estimate the shape parameter including constrained maximum-likelihood (ML) [1, 56], a least squares model fit, method of moments (MoM) [124] and zlogz [15]. The least squares and constrained ML estimators are computationally slow, while the MoM method is computationally fast and simple but may be inaccurate if the estimated shape parameter is small [15]. The zlogz estimator was shown to have a faster computation time than the constrained ML and least squares method. Moreover, the zlogz method is more accurate than MoM technique. Note that the zlogz estimator will be used in the thesis with a least squares model fit used in some cases when the zlogz returns a negative shape due to an insufficient number of samples.

The zlogz estimator for the shape of K+noise distribution is determined by numerically solving the following equation for $\hat{v}$ [15, 97]:

$$\frac{\langle z \log z \rangle}{\langle z \rangle} - \langle \log z \rangle - \frac{1}{M} = \frac{e^{\hat{v}/CNR} G_{\hat{v}+1}(\hat{v}/CNR)}{1 + 1/CNR} \tag{2.17}$$

where $\langle\,\rangle$ is the mean operator, CNR is the clutter to noise ratio and $G()$ is the generalised exponential integral function. For the case when noise power is unknown, $p_n = 0$ and the shape in Equation (2.17) becomes an effective shape [15],

$$\frac{\langle z \log z \rangle}{\langle z \rangle} - \langle \log z \rangle - \frac{1}{M} = \frac{1}{\hat{v}}. \tag{2.18}$$

The parameter estimation of the K+Rayleigh distribution requires the sum of the noise power and Rayleigh power to be estimated in addition to the shape. In Equation (2.17), the CNR is substituted with the clutter to noise plus Rayleigh power, CNR_r, using the following relationship for the distribution moments:

$$CNR_r = \frac{p_c}{p_n + p_r} = \frac{1}{\frac{1}{\sqrt{\hat{v}_r r}} + 1} \tag{2.19}$$

where

$$r = \frac{M\langle z^2 \rangle}{(M+1)\langle z \rangle^2}. \tag{2.20}$$

The shape parameter of the K+Rayleigh can now be numerically computed from Equation (2.17). Note that if the noise mean power is not known, the clutter power can be

estimated by $p_c = \langle z \rangle - \widehat{(p_n + p_r)}$, where the noise plus Rayleigh mean power is estimated using the moment relationship in [124].

For illustration, the K, K+noise and K+Rayleigh distributions are fitted to the HH polarisation of the Ingara radar outlined in Section 2.5.1. The original data is denoted by the blue line, while the K, K+noise and K+Rayleigh distributions are denoted by the red, black-dot and magenta lines respectively. It can be observed that the K+Rayleigh distribution fits better than the K and K+noise distributions, especially in the tail region. The K and K+noise distributions are similar and almost sit on top of each other. In this case, the noise has minor impact on the K distribution fitting. For this result, K and K+noise distribution shapes are estimated as 2.9 and 2.7 respectively. For the K+Rayleigh fit, the shape is 0.5. The noise mean power was determined from the radar data when the transmitter was turned off and is given by $p_n = -36.6$ dB. After the K+Rayleigh fit, the residual Rayleigh mean power, $p_r = -24.6$ dB and the ratio of the Rayleigh mean power to the mean of the data, $k_r = 0.5$.

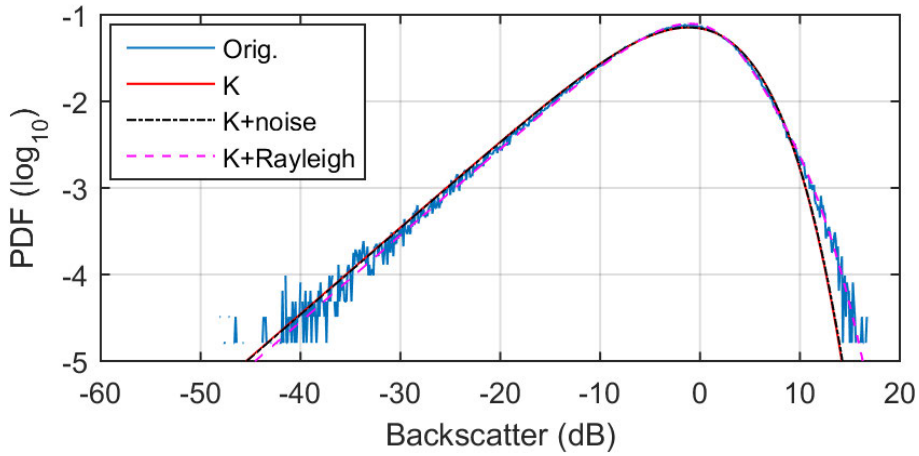

Figure 2.4. Illustration of K+noise and K+Rayleigh distributions fitted to the Ingara HH polarisation: (—) original data, (—) K, (---) K+noise and (- - -) K+Rayleigh distribution.

2.4 Radar Target Dection

Target detection is one of the main functions in radar operation. The detection decision is typically determined by comparing the amplitude of the radar backscatter to a threshold which might be pre-set or adaptively computed at the time of operation. The RCS from targets and sea-clutter are variable and the detection is generally studied in a statistical manner [124]. This section describes the principle of target detection and the distributions used to model the target and interference.

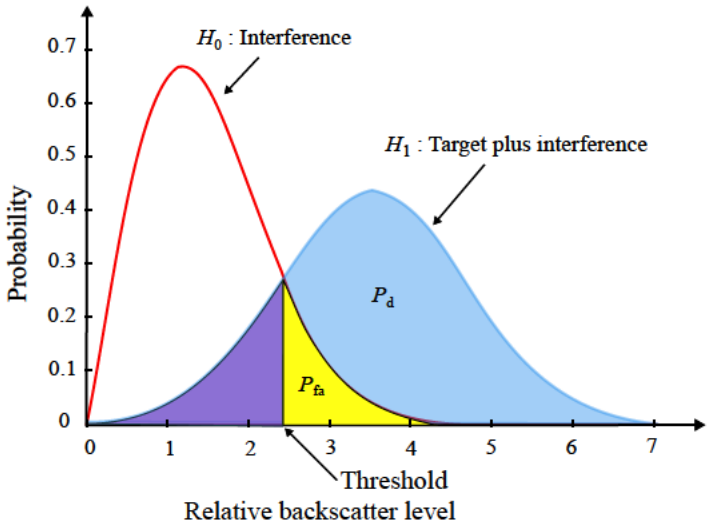

Figure 2.5. This illustrates target detection based on amplitude or intensity. The areas under the red and blue lines represent the distribution of interference and target plus interference, respectively. The probability of detection, P_d (light blue area) and probability of false alarm (yellow area) vary with the threshold.

2.4.1 Detection Principle

The principle of the detection is shown in Figure 2.5. It is based on two hypotheses: the first is when the backscatter contains only interference (clutter plus noise) and is denoted by H_0. The second hypothesis, denoted by H_1, is the case when the backscatter consists of both target and interference. Ideally, we want the two PDFs to have smallest overlap so that the probability of detection is high and the probability of false alarm is at the desired level.

The first step in the design of a detector is to find a suitable statistical model for the interference. A user will then choose a probability of false alarm, P_{fa} and the threshold for the required false alarm rate can be determined. Let P_A denote the PDF of the interference background and P_T

denote the PDF of the interference and target. As shown in Figure 2.5, if γ is the threshold, we can express the probability of detection as,

$$\begin{aligned} P_{\mathrm{d}}(\gamma) &= \mathrm{Prob}(z > \gamma | H_1) \\ &= \int_{\gamma}^{\infty} P_{\mathrm{T}}(\mathrm{z})\, \mathrm{dz} \end{aligned} \tag{2.21}$$

and the probability of false alarm

$$\begin{aligned} P_{\mathrm{fa}}(\gamma) &= \mathrm{Prob}(z > \gamma | H_0) \\ &= \int_{\gamma}^{\infty} P_{\mathrm{A}}(z)\, \mathrm{dz}. \end{aligned} \tag{2.22}$$

$P_{\mathrm{fa}}(\gamma)$ is also known as the complementary cumulative distribution function (CCDF).

A constant RCS can be represented by a Swerling case 0 or Marcum model whose magnitude is constant for all time [124]. A common target fluctuation is defined by the chi-square distribution [103, 124]:

$$P(s|S,K) = \frac{s^{F-1}}{\Gamma(F)} \left(\frac{F}{S}\right)^{F} \exp\left(-\frac{Ks}{S}\right) \tag{2.23}$$

where the parameter F is defined as the target fluctuation parameter, s, is the sum of the target powers normalised by the local clutter-plus-noise power and S is M times the average signal to interference ratio (SIR) in a square law detector [90]. Note that the original Swerling models represented the target alone and were not normalised by the local clutter-plus-noise [124]. Equivalent Swerling models for the fluctuating target can be derived by varying the value of F:

- Swerling case 1: $F = 1$
- Swerling case 2: $F = M$
- Swerling case 3: $F = 2$
- Swerling case 4: $F = 2M$

Some Swerling cases share similar characteristics. For cases 1 and 2, the target has a Rayleigh (or exponential in power) fluctuation representing several objects/reflectors fluctuating independently. This is the case when the target is relatively large, compared to the radar wavelength [109]. The RCS of Swerling case 1 has a slow fluctuation and is assumed to be constant during a single scan (group of pulses) with changes from scan to scan. The Swerling case 2, on the other hand, has a fast fluctuation which varies from pulse to pulse. For cases 3

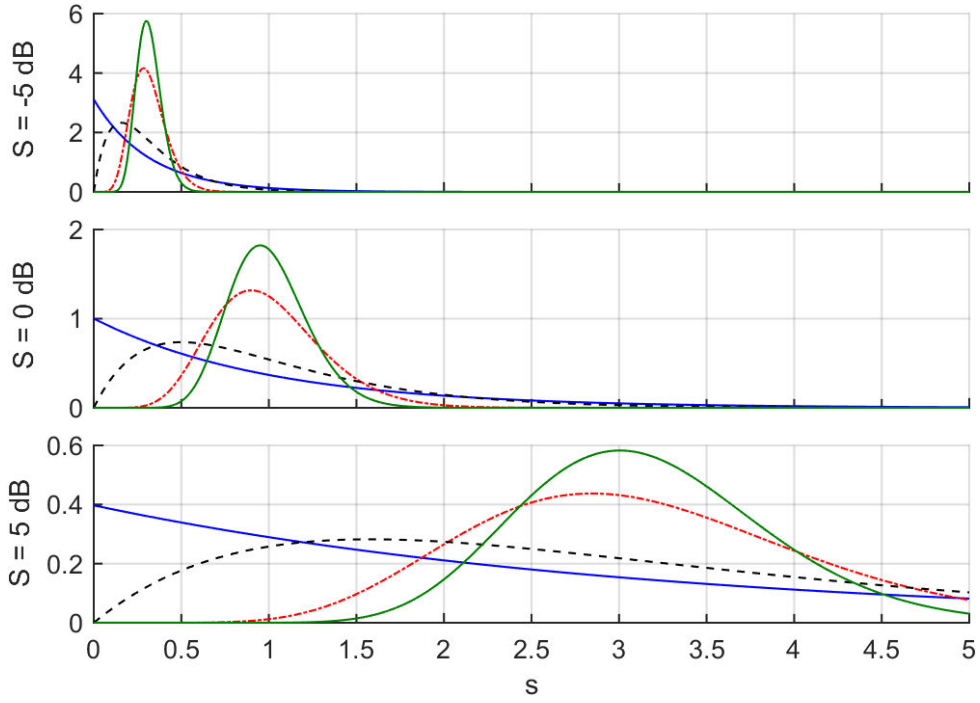

Figure 2.6. Target Swerling PDFs for the number of looks $M = 10$ and three values of target SIR (S = -5 dB (top), S = 0 dB (middle), and S = 5 dB (bottom)): (—) case 1, (- - -) case 2, (- - -) case 3, (—) case 4 [90].

and 4, the target models are represented by a chi-square distribution with 4 degrees of freedom and the target RCS is less random, compared to the first two cases. The target RCS is large in these cases with many small reflectors [18, 71, 109].

The distributions of the 4 Swerling cases representing the target RCS fluctuation are shown in Figure 2.6 for the number of looks, $M = 10$, and three different values of target SIR: -5 dB (top), 0 dB (middle) and 5 dB (bottom). The Swerling-1 and Swerling-2 are denoted by blue and red dash-dot lines while the Swerling-3 and Swerling-4 are denoted by black dash and green lines. The distribution of the Swerling-2 and 4 are narrower due to the fast changes of the target RCS. When the target SIR increases, the distributions shift to the right.

2.4.2 Constant False Alarm Rate Detection

In the previous discussion, a fixed threshold has been used to achieve the specified probability of false alarm. However, interference levels vary making it more difficult to achieve a constant false alarm rate. To overcome this, the radar detector has to adapt to the environment in real time which may be achieved by varying the threshold adaptively.

There are many constant false alarm rate (CFAR) detection schemes in the literature, including the cell averaging CFAR (CA-CFAR), greatest of CFAR, smallest of CFAR, ordered statistic CFAR, trimmed mean CFAR and the censored mean CFAR [124]. The CA-CFAR algorithm is the most popular and widely used scheme, where the data on both sides of the cell under test (CUT) are used [88, 125–127].

The CA-CFAR detection scheme is shown in Figure 2.7 with a sliding window algorithm typically applied along range. If the CUT is surrounded by M_r cells along the range direction with a gap of G guard cells, the adaptive threshold, γ, is given by

$$\gamma = \frac{T}{M_r}\left(\sum_{m=-M_r/2-G}^{-G-1} x(m) + \sum_{m=G+1}^{M_r/2+G} x(m)\right). \tag{2.24}$$

where T is threshold multiplier and is related to the desired P_{fa}. The probability of detection, P_{d} is given by:

$$P_d = \int_0^\infty \int_\gamma^\infty P(z)P(\gamma|T)\mathrm{d}z\,\mathrm{d}\gamma \tag{2.25}$$

where $P(z)$ is interference with target distribution and $P(\gamma)$ is the threshold distribution [124].

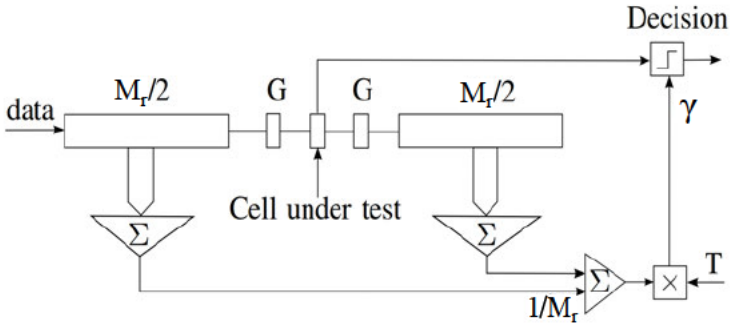

Figure 2.7. Cell-averaging CFAR detection algorithm: $\frac{M_r}{2}$ is the number of cells on both sides of the cell under test; G is the number of guard cells; T is the threshold multiplier and γ is the threshold.

The threshold multiplier, T, is a value which is set to achieve the desired probability of false alarm (P_{fa}). Two methods are used to compute the threshold multiplier in this thesis. The first is based on fitting a model to the PDF of the test statistic, while the second method is to directly measure the value from the selected data block. To determine the threshold multiplier from a model, a large sample size is required to ensure a good fit. The trend of the model can then be followed to get a value which meets the desired P_{fa}. To achieve a reasonable sample size, different blocks of data in time from before and and after the data block under test are used. These additional samples are assumed to have the same statistics as the analysed data block.

The direct measurement in the second method gives a more accurate estimation of the desired P_{fa} and the detection performance. However, it requires analysis when there is no target in the data block. The model fitting method is used for target detection in the medium grazing angle data in Chapter 4, while the second method is implemented in Chapters 5 and 6. The choice of the methods does not greatly impact the detection performance because the selected model used in the detection generally characterises the interference very well [93].

2.4.3 Monte-Carlo Simulation

Radar detection performance is generally measured via analysis of the probabilities of detection and false alarm in various interference scenarios [90]. However, often this is not possible and Monte-Carlo simulation is instead used to evaluate the performance. To quantify the detection performance, the Monte-Carlo simulation is implemented by injecting a simulated target into a number of range bins of the data. At each iteration, the target SIR is varied over a defined range with the detection performance determined in relation to the SIR variation.

2.5 Experimental Data

In the thesis, two experimental data sets are used. The first data set was collected at medium grazing angles using the Ingara radar system developed and maintained by the Defence Science and Technology (DST) group, Australia [25, 58]. The second data set comes from the NetRAD radar system [4, 5, 47, 85].

2.5.1 Ingara Sea Clutter Data

The Ingara radar is an X-band system operated with a pulse repetition frequency (PRF) of 575 Hz and a 200 MHz bandwidth, giving 0.75 m range resolution. During the trial, the radar antenna was housed beneath a Beech 1900C aircraft as shown in Figure 2.8. The trials were conducted in two distinctly different regions to achieve a range of environmental conditions. The first ‘sea clutter trial’ (SCT04) was located 100 km to the South of Port Lincoln at the edge of the South Australian continental shelf over an 8 day period in 2004. The second ‘maritime sea-clutter trial’ (MAST06) occurred in 2006 in littoral and open ocean conditions near Darwin in the Northern territory.

During the trial, radar backscatter was collected over 360° of azimuth and between 15° and 45° in grazing as shown in Figure 2.9. The aircraft flew around a nominated point of interest in an

Figure 2.8. Beech 1900C aircraft used for the Ingara sea-clutter trials.

anti-clockwise direction while the radar beam was continuously illuminating the same patch of sea-surface.

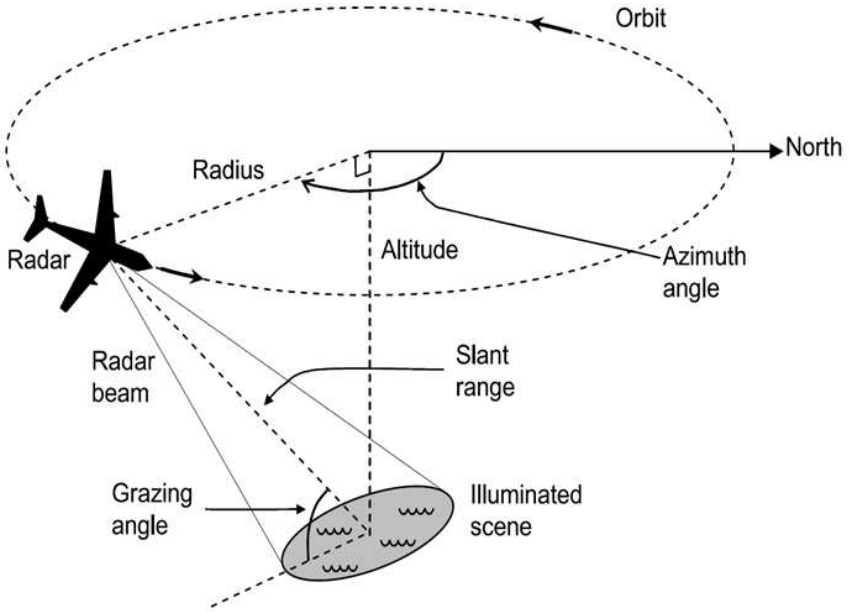

Figure 2.9. Demonstration of a trial geometry where the data is collected in a circular spotlight mode [25].

The dataset used in this thesis is dual polarised data from the 2016 trial. It comprises two subsequent runs where the radar first transmitted with a horizontal (H) polarisation and then with a vertical (V). Both runs received both H and V simultaneously. Prior to analysis of the sea-clutter, pre-processing was applied to the received backscatter. This included hardware

corrections, motion compensation, correction for grazing angle variation, elevation beampattern removal, and data calibration [82]. The mean noise power of the radar was also measured when the transmitter was turned off. Then to obtain the equivalent noise level post-processing, a new signal was created with the same dimension as the clutter plus noise and pre-processed the same as the clutter plus noise.

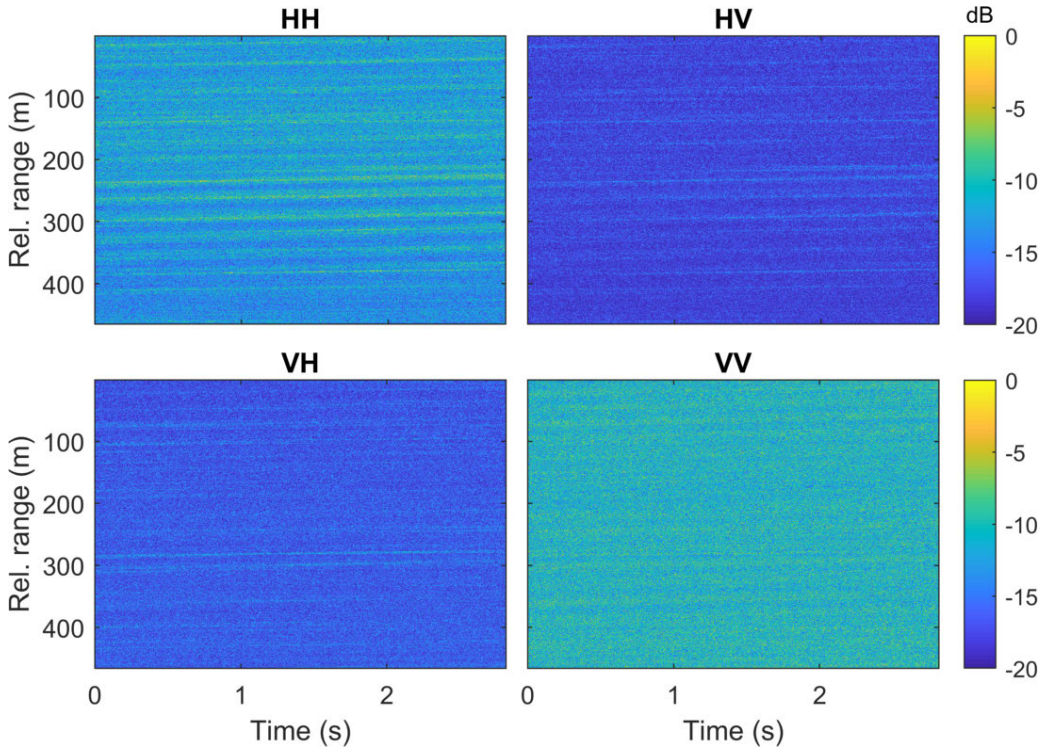

Figure 2.10. Ingara range / time intensity images: HH (top left), VH (top right), VH (bottom left) and VV (bottom right).

For illustration, a 2 s data block has been chosen from the upwind direction covering 430 m with grazing angles between $30.5° - 35.5°$. Figures 2.10 and 2.11 show the data: HH (top left), VH (top right), VH (bottom left) and VV (bottom right). Figure 2.10 shows the variation of the data in the range / time intensity domain. Figure 2.11 shows the variability in the power spectral density (PSD) or Doppler spectrum for a coherent pulse interval (CPI) of 64 pulses.

It can be observed that that the backscatter intensities appear strong especially in the VV polarisation. Sea-spikes on the other hand appear as strong white lines and are more predominantly seen in HH polarisation. In the PSD domain, the sea-spikes vary in range and some spread almost the entire data bandwidth.

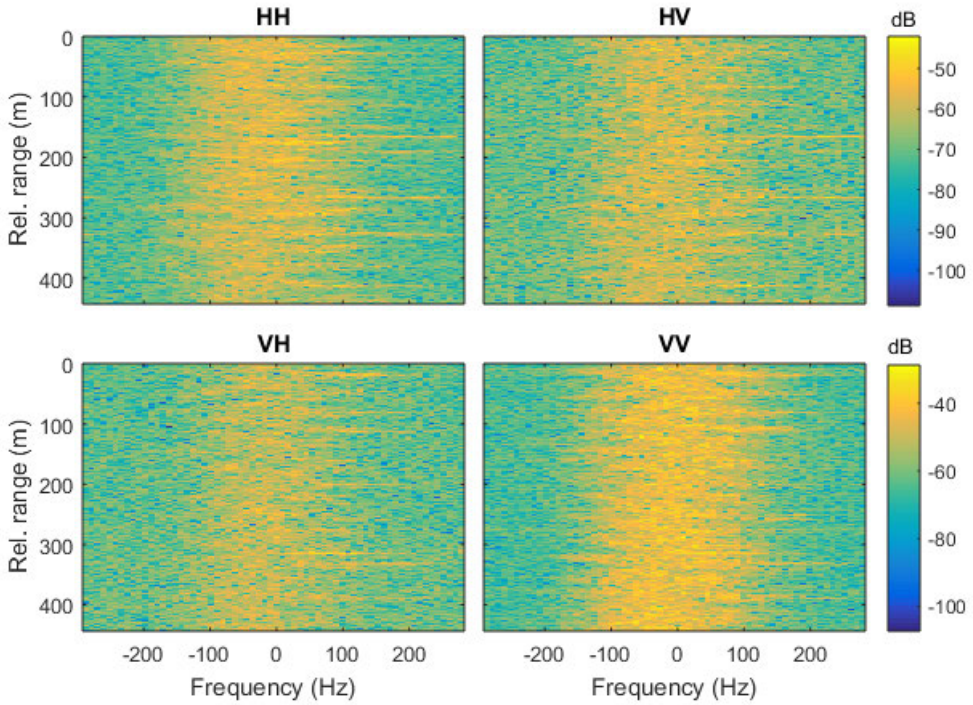

Figure 2.11. Ingara range / frequency images (dB): HH (top left), VH (top right), VH (bottom left) and VV (bottom right).

2.5.2 NetRAD Bistatic Sea Clutter Data

The Ingara radar previously described is a monostatic system where the transmitter and receiver share a common antenna. When more than one receiving antenna is used, the system is known as a bistatic or multistatic system. There has been a considerable interest in bistatic radar over the past decade to see if it offers potential advantages over monostatic radar [4, 47, 64].

The NetRAD is a multistatic radar system developed by a team from the University College London (UCL), UK and the University of Cape Town (UCT), South Africa. It is a ground-based pulsed-Doppler coherent multistatic system consisting of three identical radar nodes [4]. Multistatic operation required the transmitter and receiver antennas to be situated apart. Therefore, GPS disciplined oscillators (GPSDOs) and a 5 GHz wireless link were used for synchronisation and data communication [95, 96]. The radar has a centre frequency of 2.4 GHz, a 45 MHz bandwidth and 1 kHz pulse repetition frequency (PRF). The radar system can operate with either horizontal or vertical polarisations.

The data used in this thesis was recorded during a series of trials in October 2010 on the coast of South Africa near the Cape Point area. The wind direction was from the North with a speed that increased during the trials from 10.18 m/s to 12.3 m/s, while the wave height varied between

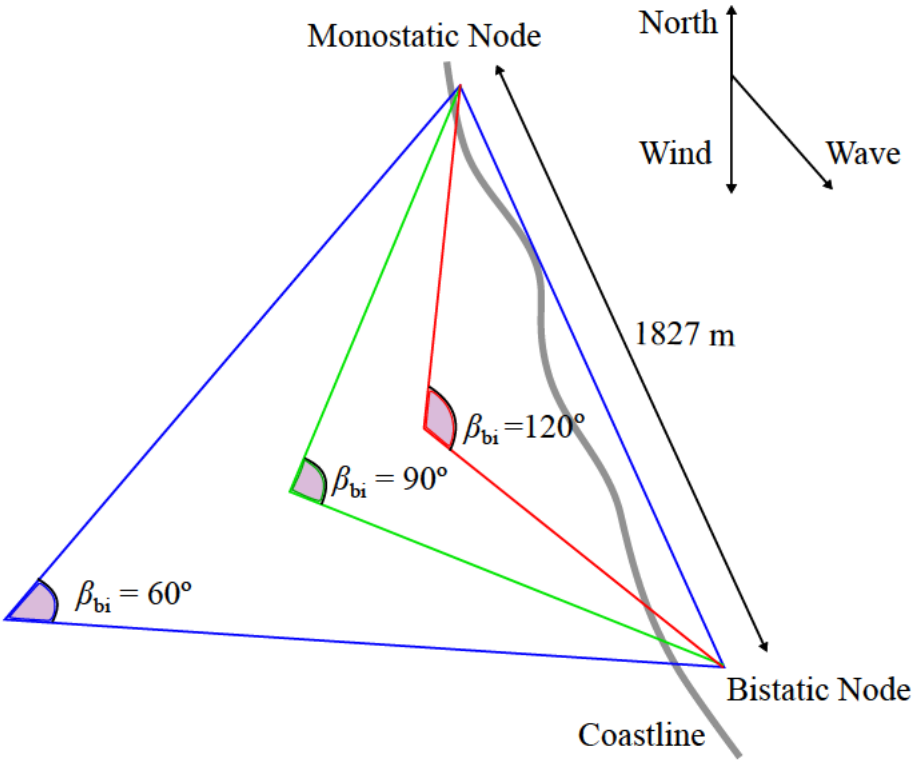

Figure 2.12. Geometry of the NetRAD radar trial for three different "bistatic" angles: 60°, 90° and 120°.

3.28 m to 4.2 m. This corresponds to a Douglas sea state 5. In this particular trial, only two nodes were used. One node was monostatic while the other node received only. Both nodes were looking cross-wind with the waves travelling towards the receiver of the bistatic node. Three bistatic angles were measured, 60°, 90° and 120°.

To achieve these different bistatic angles, the look direction of the radars (antennas) were changed. For the sea-clutter collections, the radar system had a baseline that ran North-West to South-East with a separation between the two nodes of approximately 1827 m. Figure 2.12 shows the trial geometry. By fixing the radar locations, the radar illuminates different patches of the sea and direct comparison of bistatic angles may be difficult.

Figure 2.13 shows an example of the data in intensity for 130 s (or 130000 pulses) for both monostatic and bistatic data recorded with a bistatic angle $\beta_{bi} = 60°$ and HH polarisation. Figure 2.14 is the PSD of the data using the first 128 pulses in the CPI. The top plots are monostatic and the bottom plots are the corresponding bistatic data. Figure 2.13 shows the

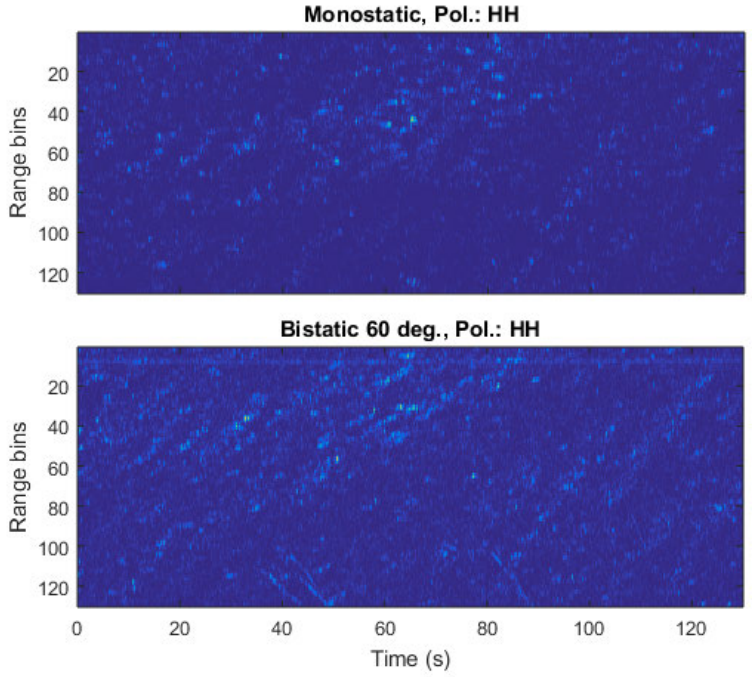

Figure 2.13. Illustration of NetRAD HH polarised data recorded at 60° bistatic angles for both monostatic (top) and bistatic (bottom). The bright spots in both configurations are corresponding to breaking waves on the sea surface.

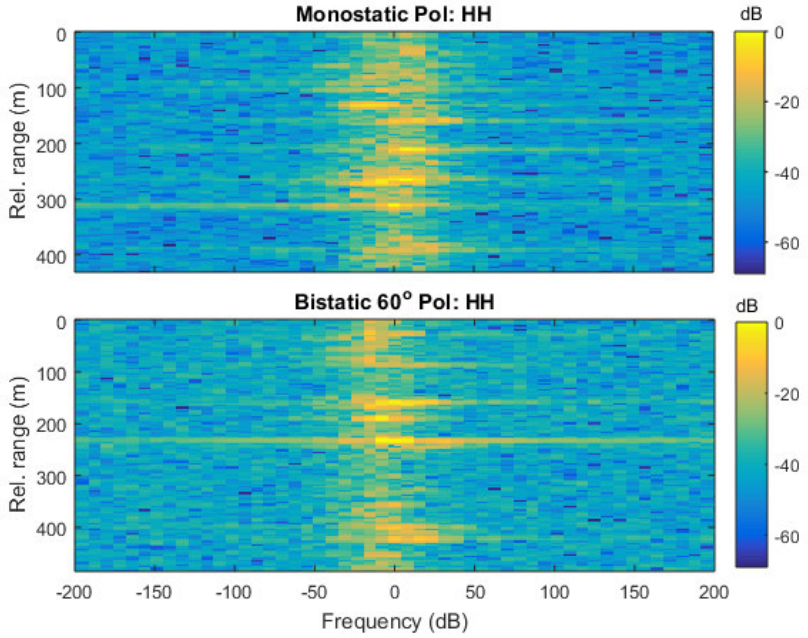

Figure 2.14. The PSD for the first 0.12 second of the monostatic and bistatic NetRAD data shown in Figure 2.13.

sea structure with sea waves moving toward the bistatic receivers. Some breaking waves are also seen as bright white in the data and appear at multiple range bins. These bright colour components are observed throughout the data in both monostatic and bistatic data sets.

2.6 Conclusion

In this chapter, the fundamentals of maritime radar have been introduced. The important aspects of sea-clutter were outlined, including sea-spikes which exhibit the same characteristics as a target, and cause problems in radar target detection. The chapter also described the conventional detection algorithm using a CA-CFAR scheme. Two methods were discussed to determined the threshold multiplier, one based on modelling the sea clutter distribution while the other is based on direct measurement of the processed data. Monte-Carlo simulation was also presented as a technique to measure the detection performance.

The final part of the chapter described two different data sets. The first was recorded from an aeroplane at medium grazing angles while the second data set was recorded at low grazing angles using a bistatic radar system. These two data sets are used for the analysis and validation of the new detection algorithms in this thesis.

Chapter 3

Time Frequency Analysis

THIS chapter outlines the background theory of time-frequency analysis in preparation for their application in later chapters. A number of time-frequency techniques are discussed including the short time Fourier transform and various types of wavelet transforms. The main signal processing techniques for analysing sea-clutter are then outlined.

3.1 Introduction

One of the earliest and still widely used methods for signal analysis is the Fourier transform. For the case of radar signal processing, the Fourier transform underpins a wide range of applications. It is used for imaging to reveal signal spectral components embedded within the radar returns and can be useful for target detection. By employing Doppler processing for sea-clutter, different sea-clutter characteristics can be studied in the frequency domain.

Any target present in the radar backscatter can be distinguished from the clutter if its amplitude is sufficiently high compared to the surrounding data or it moves at a faster velocity relative to the clutter. However, the target is often located in the endo-clutter region and it is difficult to distinguish from the clutter.

Due to the motion of sea-surface components, the sea-clutter can vary considerably over time and range as shown in Figure 2.11 in Chapter 2. Moreover, clutter statistics at the edges of the clutter spectrum are particularly non-Gaussian and vary from range bin to range bin [92,93,124] resulting in sea-clutter that is range and time varying.

To better analyse and understand sea-clutter, we need analytical tools that compute the frequency spectrum as time evolves; these techniques are generally known as time-frequency transforms. Some examples of time-frequency transforms include the short time Fourier transform and various wavelet transforms. They are discussed in this chapter as they are relevant to the target detection schemes in later chapters.

In this chapter, we will start by looking at the Fourier transform in Section 3.2 and the short time Fourier transform in Section 3.3. The chapter then looks at the continuous wavelet transform and the discrete version with the concept of multi-resolution analysis in Section 3.4. A non-decimated version of the discrete wavelet transform, namely the stationary wavelet transform, is then studied in Section 3.4.4. Finally, the tuned Q-factor wavelet transform is outlined in Section 3.5 and the conclusion of the chapter is given in Section 3.6.

3.2 Fourier Transform

The Fourier transform is widely used for signal analysis in many engineering and scientific applications. It decomposes any signal into a set of sinusoids at different frequencies by transforming the original *time* domain signal $f(t)$ to the *spectral* or *frequency* domain $F(\omega)$,

$$F(\omega) = \int_{-\infty}^{\infty} f(t) \exp\left(-j\omega t\right) \, \mathrm{d}t, \tag{3.1}$$

where $\omega = 2\pi f$ is the angular frequency. The inverse Fourier transform reconstructs the original signal from the spectral domain, and is defined as

$$f(t) = \frac{1}{2\pi} \int_{-\infty}^{\infty} F(\omega) \exp(j\omega t)\, \mathrm{d}\omega. \tag{3.2}$$

The Fourier transform pair $f(t)$ and $F(\omega)$ are constrained by the uncertainty principle which states that if a signal is confined to a time interval Δ_t of $f(t)$ then its Fourier transform is confined to the small frequency interval Δ_ω of $F(\omega)$ according to

$$\Delta_t^2 \Delta_\omega^2 \geq \frac{1}{4} \tag{3.3}$$

where

$$\Delta_t^2 = \frac{\int_{-\infty}^{\infty} (t-\mu_t)^2 |f(t)|^2\, \mathrm{d}t}{\int_{-\infty}^{\infty} |f(t)|^2\, \mathrm{d}t},$$

$$\Delta_\omega^2 = \frac{\int_{-\infty}^{\infty} (\omega-\mu_\omega)^2 |F(\omega)|^2\, \mathrm{d}\omega}{2\pi \int_{-\infty}^{\infty} |F(\omega)|^2\, \mathrm{d}\omega}$$

and μ_t and μ_ω are the mean time and mean frequency, respectively. It is thus impossible to have arbitrarily fine resolution in both frequency and time domains simultaneously. Improvement in one domain necessarily comes at a detriment to the other. Time-frequency transforms have therefore been introduced to enable different representations of the data and to trade-off time and frequency resolution. Some examples of time frequency transforms include the short-time Fourier transform and the wavelet transform. They are outlined in the subsequent sections.

3.3 Short Time Fourier Transform

The short-time Fourier transform (STFT) was first introduced by Gabor [46] and is a standard approach to analysing signals with time-varying frequency components. The STFT takes small time segments, over which the signal can be assumed stationary and applies a Fourier transform. The operation is defined as

$$STFT(t,\omega) = \int f(t')w(t'-t) \exp\left(-j\omega t'\right)\, \mathrm{d}t' \tag{3.4}$$

where $f(t')$ is the original time signal and $w(t'-t)$ is the window function shifted by $t \leq T_w$ (T_w is the width of the window function). The squared magnitude of the STFT is the power spectral density of the signal in the localised time window. By applying the method over many segments, the results are shown in a 2D representation or 'spectrogram'.

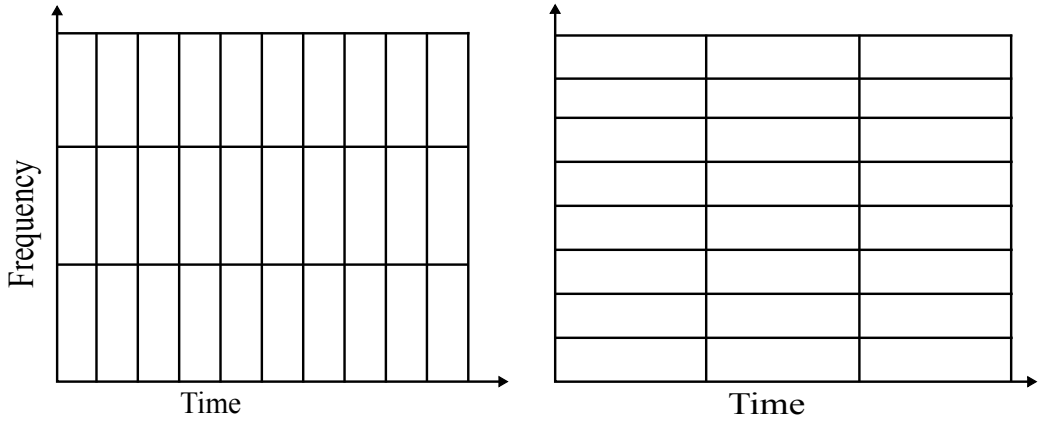

Figure 3.1. Time frequency resolution (or plane) of the STFT. The time and frequency resolution are fixed in both time and frequency. Left: good time resolution, right: good frequency resolution.

Window functions in a STFT have a fixed width in time and frequency which limits the obtainable time-frequency resolution. Due to the uncertainty principle, a fine resolution in time (small time window) necessarily implies coarse resolution in frequency (large frequency window) and vice versa [23]. Figure 3.1 shows the trade off between frequency and time resolution. When analysing a signal with a discontinuity or chirp and fast changing spectral content, it is difficult to specify an appropriate window size with a constant window. To overcome this disadvantage, wavelet transforms with different scales can be used instead [27, 68, 108]. This allows a window width that adapts to the bandwidth of the analysed signal.

3.4 Wavelet Transform

Wavelet transforms (WT) are another widely used time-frequency representation [27, 68, 72, 108]. The WT has been used for signal processing in various applications to obtain compact representations of non-stationary signals. They have an ability to represent signals at multiple scales, or *resolutions*, with different time windows, thus offering a very different partitioning of the time frequency plane compared with the traditional Fourier transform and STFT [26]. For WTs, the analysing functions are dilated (to achieve frequency localisation) and shifted (time localisation) versions of the same template function, called the wavelet function $\psi(t)$.

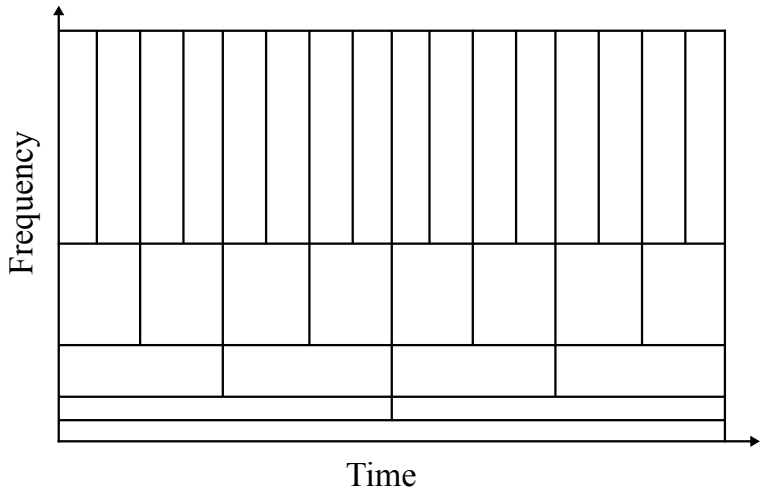

Figure 3.2. Time frequency resolution (or plane) of the WT. The tiling resolution varies with frequency contents: finer frequency resolution for lower frequencies.

3.4.1 Continuous Wavelet Transform

For continuous time signals, the WT is a set of inner products between the dilated and shifted wavelet functions and the signal. The continuous wavelet transform (CWT) of a signal $f(t) \in L_2(\mathbb{R})$ is defined as

$$\begin{aligned} W_f(a,b) &= \langle f(t), \psi_{a,b}(t) \rangle \\ &= \int_{-\infty}^{\infty} f(t) \psi^*_{a,b}(t)\, \mathrm{d}t \end{aligned} \tag{3.5}$$

where $\langle\ ,\ \rangle$ and * denote the inner product and complex conjugate, respectively. ψ is the wavelet function, whose scaled and shifted versions are described by

$$\psi_{a,b}(t) = \frac{1}{\sqrt{a}} \psi \left(\frac{t-b}{a} \right), \tag{3.6}$$

where the parameter $b \in \mathbb{R}$ is the *translation* and $a \in \mathbb{R}^+$ is the *dilation (or scale)* parameter. Translation represents a time shift, while dilation or scale relates to the frequency.

In Equation (3.6), the width of the mother wavelet is controlled by the scale a. By reducing the value of a, the width in time is shorter and therefore $\psi_{a,b}$ covers a wider frequency range and similarly when a is increased, the width is longer. As shown in Figure 3.2, the time and frequency scales of the wavelet transform are different. However, the area of the boxes remain the same, satisfying the uncertainty principle in Equation (3.3). The $\frac{1}{\sqrt{a}}$ term is included in the equation to ensure that the wavelet functions have the same energy at all scales.

For ψ to be a valid wavelet and to ensure perfect reconstruction, it must meet the admissibility condition:

$$C_\psi = \int_{-\infty}^{+\infty} \frac{|\Psi(\omega)|^2}{|\omega|} \mathrm{d}\omega < \infty, \tag{3.7}$$

where Ψ represents the Fourier transform of the wavelet. A corollary of Equation (3.7) is

$$\Psi(0) = \int_{-\infty}^{+\infty} \psi(t)\mathrm{d}t = 0. \tag{3.8}$$

The signal can then be reconstructed back to time domain via an inverse continuous wavelet transform,

$$f(t) = \frac{1}{C_\psi} \int_0^\infty \int_{-\infty}^\infty W_f(a,b)\psi_{a,b}(t)\mathrm{d}b\frac{\mathrm{d}a}{a^2} \tag{3.9}$$

The CWT in Equation (3.5) has a bandpass characteristic where the wavelet function ψ has a bandpass impulse response. In addition, the value of $|\Psi|$ in Equation (3.7) decreases rapidly for $|\omega| \to 0$ and $|\omega| \to \infty$ [70]. To cover the whole frequency spectrum of the signal, an infinite number of wavelet functions are used for the decomposition. However, for a finite number of scales, there always exists a low frequency region of the signal which cannot be represented by the wavelet functions. When a lower bound in the wavelet analysis is implemented, a scaling function, $\phi(t)$ (or low-pass filter) is introduced to capture the low-frequency region [27, 67, 76]. This scale function is complementary to the wavelet function and must also satisfy the admissibility condition,

$$\int_{-\infty}^{+\infty} \phi(t)\mathrm{d}t = 1. \tag{3.10}$$

3.4.2 Discrete Wavelet Transform

The CWT is highly redundant and is computationally slow [27, 79]. One option to overcome this is to use a discrete version of the CWT [79]. For the discrete wavelet transform (DWT), the parameters a and b of the wavelet function in Equation (3.5) are discretised:

$$a \equiv a_0^k \text{ and } b \equiv a_0^k m b_0; \quad \text{for} \quad k, m \in \mathbb{Z}$$

where a_0 and b_0 are a pair of integers with $a_0 > 1$ and $b_0 > 0$ [27]. The widths of the same wavelet function vary with different k values where k is known as the decomposition level or scale in the DWT. The wavelet function in Equation (3.6) then becomes:

$$\psi_{k,m}(t) = a_0^{-k/2}\psi(a_0^{-k}t - mb_0). \tag{3.11}$$

The wavelet transform is usually implemented with the dyadic scaling factor ($a_0 = 2$ and $b_0 = 1$),

$$\psi_{k,m}(t) = 2^{-k/2}\psi(2^{-k}t - m) \tag{3.12}$$

and the set of DWT coefficients $D_k(m)$ for the signal $f(t)$ is defined as

$$D_k(m) = \langle f(t), \psi_{k,m}(t) \rangle. \tag{3.13}$$

The coefficients $D_k(m)$ represent the signal $f(t)$ in the transform domain with respect to the wavelet $\psi_{k,m}(t)$ using dyadic scaling. In this thesis, we only consider orthogonal wavelets, with the wavelet function $\psi_{k,m}(t)$ also used for signal reconstruction. For a given set of DWT coefficients $D_k(m)$, the wavelet signal reconstruction of any signal spanning $L_2(\mathbb{R})$ is given by:

$$f(t) = \sum_{k=-\infty}^{\infty} \sum_{m=-\infty}^{\infty} D_k(m)\psi_{k,m}(t). \tag{3.14}$$

In practice, the infinite scales are truncated and $f(t)$ is approximated by a series of scaling functions $\phi_{k,m}(t)$. Let V_k, $k \in \mathbb{Z}$ be the subspaces containing low-pass signals. As k increases, V_k corresponds to a coarser approximation and the summation of subspaces at coarser resolutions result in a more detailed resolution:

$$V_k = V_{k+1} \oplus W_{k+1}, \tag{3.15}$$

where $\oplus$ is a direct sum and W_{k+1} is the wavelet subspace which fills in the missing detail in between V_k and V_{k+1}. The sequence of subspaces V_k satisfy the following properties.

(i) A nested sequence of subspaces:

$$\cdots \subset V_{k+1} \subset V_k \subset V_{k-1} \subset \cdots. \tag{3.16}$$

(ii) A scaling property: if a signal $f(t)$ is scaled by a factor of two (i.e. $f(t) \to f(2t)$), the scaled signal $f(2t)$ is an element of a larger subspace and vice versa:

$$f(t) \in V_k \Leftrightarrow f(2t) \in V_{k-1}. \tag{3.17}$$

(iii) Signal approximation: the projection of a signal $f(t) \in L_1(\mathbb{R})$ onto the subspace V_k produces a sequence of functions or sub-bands, $f_k(t)$. The signal $f(t)$ is then approximated by the sequence $f_k(t)$,

$$\lim_{k \to -\infty} f_k(t) = f(t), \quad f(t) \in L_2(\mathbb{R}), \quad f_k(t) \in V_k \tag{3.18}$$

Using the scaling property in (ii), one can show that the subspace V_k is spanned by scaled and time-shifted versions of the scaling function $\phi(t)$,

$$V_k = \text{span}\{\phi(2^{-k}t - m), m \in \mathbb{Z}\}. \tag{3.19}$$

Therefore, the sub-band signals $f_k(t) \in V_k$ at a scale k are given by

$$f_k(t) = \sum_{m=-\infty}^{\infty} A_k(m)\phi_{k,m}(t) \tag{3.20}$$

where $A_k(t) = \langle f(t), \phi_{k,m}(t)\rangle$ and $\phi_{k,m}$ is given by

$$\phi_{k,m}(t) = 2^{-k/2}\phi(2^{-k}t - m). \tag{3.21}$$

The overall missing details are the summation of subspaces between successive scales:

$$L_2(\mathbb{R}) = \cdots \oplus W_{-1} \oplus W_0 \oplus W_1 \oplus \cdots \tag{3.22}$$

where

$$W_k = \text{span}\{\psi(2^{-k}t - m), m \in \mathbb{Z}\}, \quad k \in \mathbb{Z} \tag{3.23}$$

is the detail (or wavelet subspace) at scale k.

In practice, the DWT coefficients of the signal $f(t)$ are commonly computed using two-channel filter banks via the scaling $\phi_{k,m}(t)$ and wavelet $\psi_{k,m}(t)$ functions. For illustration, assume that $k = 0$ is the finest resolution of the signal $f(t)$ and the projection of the signal onto $\phi_{0,m}(t)$ or $\phi(t - m) \in V_0$, $m \in \mathbb{Z}$ is the linear combination of the next coarser subspaces: $V_0 = V_1 \oplus W_1$ from the definition given in Equation (3.15). The relation between the scaling and wavelet functions for $k = 0$ are characterised by

$$\phi_{0,m}(t) = \sum_{n=-\infty}^{\infty} h_a(2n - m)\phi_{1,m}(t) + \sum_{n=-\infty}^{\infty} g_a(2n - m)\psi_{1,m}(t), \quad m, n \in \mathbb{Z} \tag{3.24}$$

where $h_a(n)$ are the coefficients of the scaling function and act as a low pass filter, while $g_a(n)$ are the coefficients of the wavelet function which behaves as a high pass filter. In this case, the wavelet function $\psi(t)$ is generated from the iterative filtering with $h_a(n)$ and $g_a(n)$.

If a known sequence $A_0(m)$ are the scaling coefficients of the discrete-time signal representing the function $f(t)$,

$$\begin{aligned} f(t) &= \sum_{m=-\infty}^{\infty} A_0(m)\phi_{0,m}(t) \\ &= \sum_{m=-\infty}^{\infty} A_0(m)\left(\sum_{n=-\infty}^{\infty} h_a(2n-m)\phi_{1,m}(t) + \sum_{n=-\infty}^{\infty} g_a(2n-m)\psi_{1,n}(t)\right) \\ &= \sum_{n=-\infty}^{\infty} \underbrace{\sum_{m=-\infty}^{\infty} A_0(m)h_a(2n-m)}_{A_1(n)}\,\phi_{1,m}(t) + \sum_{n=\infty}^{\infty} \underbrace{\sum_{m=-\infty}^{\infty} A_0(m)g_a(2n-m)}_{D_1(n)}\,\psi_{1,m}(t). \end{aligned} \tag{3.25}$$

This is the first level decomposition using the DWT. The first term represents the low-resolution approximation where A_1 is the approximate sub-band of the signal at the first level. The second term contains the detail of the signal and hence D_1 is referred to as the detail sub-band.

For a k-level decomposition, the nested subspace of the function $f(t)$ is given by $V_0 = V_k \oplus W_k \oplus W_{k-1} \oplus \cdots \oplus W_1$. This is known as multi-resolution analysis where the very coarse approximation is iteratively refined as shown in Equation (3.25). In this case, the approximate sub-band is further decomposed using the same set of analysis filters. Figure 3.4 shows the multiple level of a DWT (top) and its frequency band (bottom). Each sub-band maintains half of the frequency band of the previous sub-band. By extending the previous discussion, it can be shown that the set of approximation A_k and detail D_k sub-bands are computed as follows:

$$A_k(n) = \sum_{m=-\infty}^{\infty} A_{k-1}(m)h_a(2n-m), \tag{3.26}$$

$$D_k(n) = \sum_{m=-\infty}^{\infty} A_{k-1}(m)g_a(2n-m), \tag{3.27}$$

where $k = 0, 1, 2, \cdots, K$. The transform depth K is a user-chosen parameter and depends on the application. The wavelet $D_k(n)$ and approximate $A_k(n)$ sub-bands are successively computed from $A_{k-1}(n)$. For a K-level decomposition, there will be K detail and one approximate sub-band.

To achieve perfect reconstruction, $g_a(n)$ and $h_a(n)$ are *complementary* which means that the information which is not maintained in one is stored in the other and the frequency bands of any decomposed signals are divided into low- and high-frequency signals as shown in the bottom part of Figure 3.3. Aliasing caused by the overlapping region is designed to have opposite phase and are cancelled out in the reconstruction.

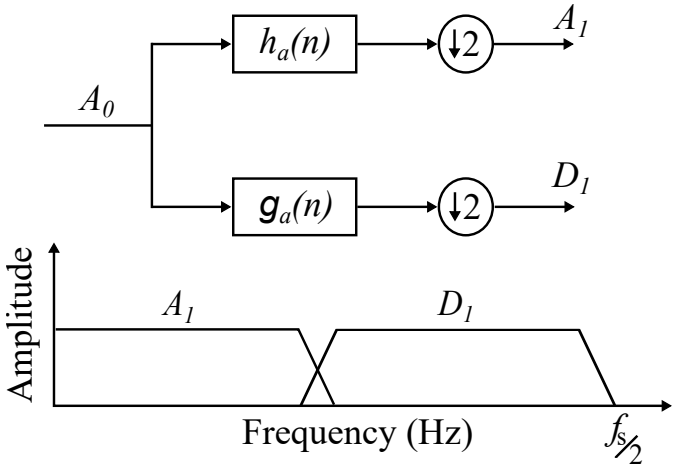

Figure 3.3. Signal analysis using two channel filter banks (top) with the sub-band frequency band (bottom). A_1 and D_1 are the approximate and detail sub-bands, respectively and f_s is the sampling frequency.

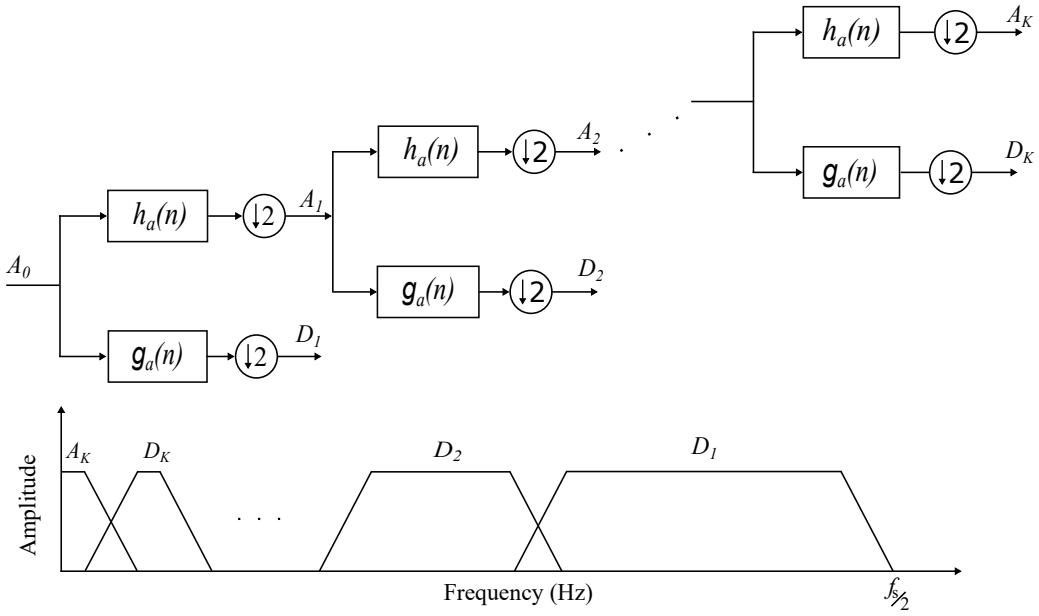

Figure 3.4. Multi-level decomposition of the DWT and sub-band frequencies using two channel filter banks. K is the level of decomposition and f_s is the sampling frequency.

The reconstruction process of the DWT is analogous to the decomposition. The sets of DWT coefficients are filtered in reverse,

$$A_k(m) = \sum_{n=-\infty}^{\infty} A_{k+1}(n)h_s(m-2n) + \sum_{n=-\infty}^{\infty} D_{k+1}(n)g_s(m-2n), \tag{3.28}$$

where $h_s(n)$ and $g_s(n)$ are the low-pass and high-pass synthesis filters, respectively.

For discrete time systems, the samples are obtained by sampling the signal $f(t)$ which is assumed to be 'finest' approximation of the continuous function. For DWT analysis, the

convention is to use the samples of the signal as the wavelet coefficients at the intrinsic scale, i.e. $f(nt_s) = A_0(m)$. While this relationship is strictly not true as the scaling functions are usually not interpolating functions, the approximation nevertheless retains the desirable time-frequency properties of the wavelet transform.

Equation (3.28) is the generalised DWT signal reconstruction. Figure 3.5 illustrates the multi-level reconstruction of the DWT. The coefficients of the approximate A_K and detail D_K sub-bands are up-sampled and then fed to the synthesis filters, low-pass $h_s(n)$ and high-pass, $g_s(n)$, respectively. Summing the two outputs at each level exactly reproduces the finest scale signal at the previous level. This can be iterated through multiple levels.

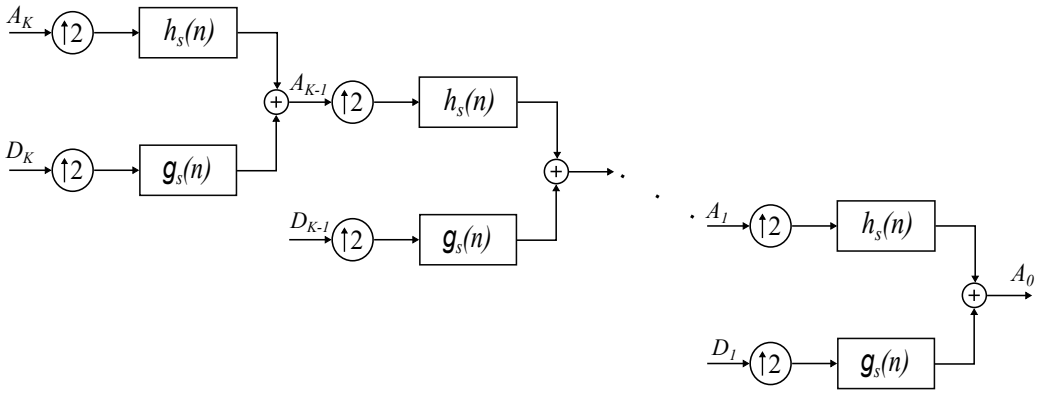

Figure 3.5. Multi-level signal reconstruction of the DWT using two channel synthesis filter banks.

3.4.3 2D Discrete Wavelet Transform

The 1D discrete wavelet transform can also be extended to 2D wavelet analysis. The concept is widely used for image manipulation concerning storage, de-noising, digital forensics and circulation over the internet where the size of the image is important. The 2D DWT, illustrated in Figure 3.6 is computed by performing 1D DWTs along rows and columns of the 2D signal [67]. A one-level 2D DWT produces coefficients which are grouped into 4 separate sub-bands (approximation, horizontal, vertical and diagonal). To avoid confusion, the one level approximate sub-band in the 2D DWT is labelled LL_1, the horizontal sub-band is denoted by LH_1 while vertical and diagonal sub-bands are denoted by HL_1 and HH_1, respectively.

The coefficients in the approximate sub-band LL_1 is a lower resolution version of the original 2D data and is equivalent to applying a low-pass filter along the rows and columns of the data. The LL_1 sub-band contains the majority of the energy for most data sources. It follows that

omitting the coefficients of this sub-band during reconstruction will cause the biggest distortion to the original data. The horizontal sub-band LH_1 is the result of applying a low-pass filter along the rows and then a high-pass filter along the columns, so it emphasises high frequency information along the columns and removes them from the rows. Visually, this results in horizontal edges appearing more pronounced. Similarly, due to the different application of low-pass and high-pass filters along the rows and columns, the vertical HL_1 sub-band leads to an emphasis of vertical edges while HH_1 emphasises diagonal edges.

Note that due to the downsampling process in the DWT computation, the sizes of the 4 sub-bands are reduced to half of the original size in both dimensions. For example, if we have an $(N \times N)$ matrix or image, then each of the 4 sub-bands has a size of $(\frac{N}{2} \times \frac{N}{2})$. This is shown in Figure 3.7.

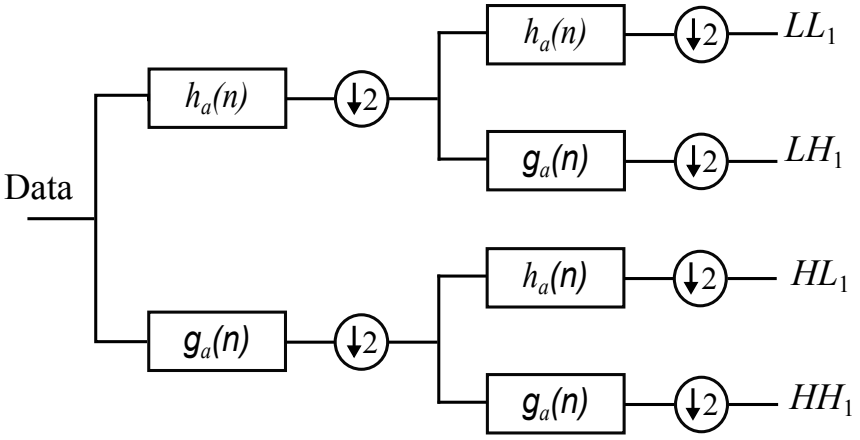

Figure 3.6. Signal decomposition block diagram using the 2D DWT. $h_a(n)$ and $g_a(n)$ are complementary low- and high-pass filters, respectively.

3.4.4 Stationary Wavelet Transform

Downsampling in the DWT leads to a non-expansive representation, which is crucial for storage-sensitive applications such as image compression. However, reducing the sampling rate can potentially create problems such as aliasing and may create undesirable artefacts when the signal is reconstructed from processed coefficients [105]. To avoid the problem, a non-decimated version of the wavelet transform, the stationary wavelet transform (SWT), can be used [80, 105]. The time-invariant properties in a non-decimated wavelet transform is important for statistical analysis and applications such as detection or parameter estimation of electroencephalogram (EEG) signals [20].

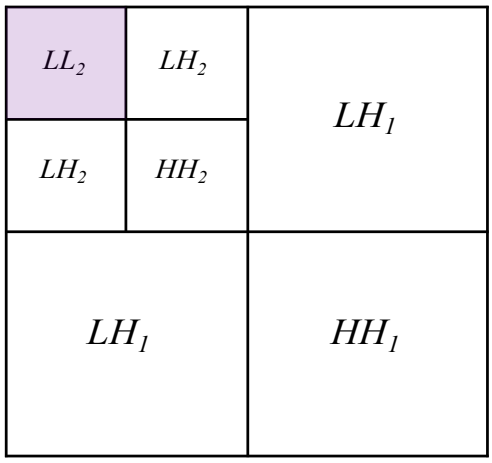

Figure 3.7. Two level image decomposition using the 2D SWT: Approximation sub-band (LL), horizontal detail sub-band (LH), vertical detail sub-band (HL) and diagonal sub-band (HH).

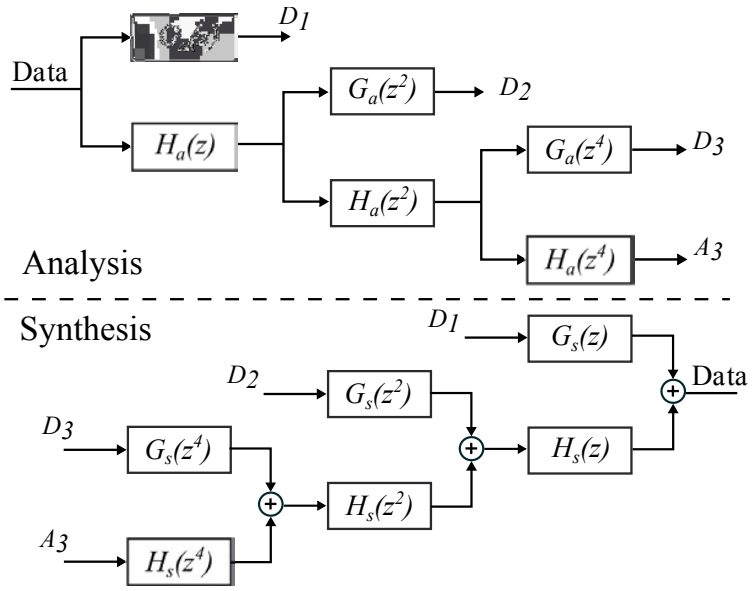

Figure 3.8. Stationary multi-level analysis and synthesis filtering: $H_a(z), G_a(z), H_s(z)$ and $G_s(z)$ are the frequency response of the low- and high-pass analysis and synthesis filters, respectively.

The computation of the SWT is similar to the DWT, where the two sets of filters are applied to the data to produce two sub-bands. The change of sampling rates are discarded during decomposition and reconstruction as shown in Figure 3.8 and as a result, the two sub-bands contain the same number of samples as the original data. Although the sampling rates of the data remain the same, the SWT retains the key multi-resolution property by upsampling the k-th level analysis filters by a factor 2^k. The four filters (h_a, g_a, h_s and g_s) are represented by their equivalent transfer functions, G_a, H_a, G_s and H_s in the z-domain.

The downside of this approach is that it carries higher computational cost and produces a redundant representation of the original data [80]. The 2D version of the SWT is analogous to the 2D DWT, in separately applying the equivalent filters along rows and then columns.

3.5 Tuned Q-factor Wavelet Transform

The tuned Q-factor wavelet transform (TQWT) is a fully-discrete transform which retains the perfect reconstruction property and can be implemented with fast Fourier transforms (FFT). With an adjustable Q-factor in the TQWT, some additional advantages are achieved over the DWT. The TQWT is able to sample the time-frequency plane more densely in both time and frequency and can achieve higher frequency resolution with a high Q-factor [100]. It is exactly invertible and is a fully-discrete approximation of the CWT. The dyadic WTs (e.g. DWT) have a fixed, low Q-factor, while the TQWT allows a user to vary the Q-factor to suit an analysed signal.

Similar to the DWT, the tuned Q-factor wavelet transform (TQWT) is implemented using two-channel multi-rate low- and high-pass filter banks, denoted by $H_a(z)$ and $G_a(z)$, respectively [100]. As shown in Figure 3.9, the filtered signal goes through a process of time scaling. If f_s is the sampling rate of the analysed signal x, then the low-pass scaling (LPS) produces the A_1 sub-band with sampling rate αf_s and preserves only the low frequency components of the signal. For high-pass scaling (HPS), the high frequency component of the analysed signal is preserved and the D_1 sub-band has sampling rate βf_s.

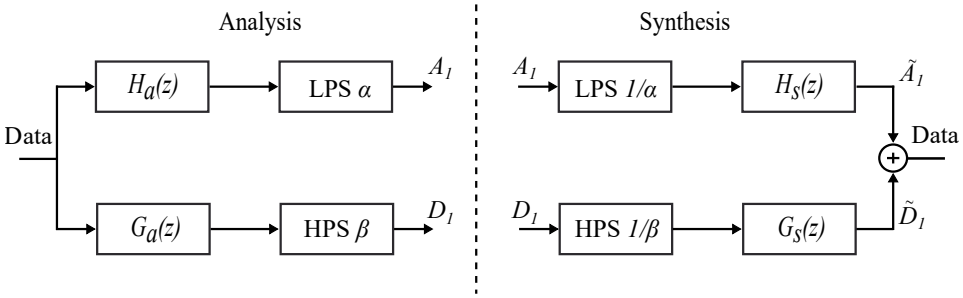

Figure 3.9. Tuned Q-factor wavelet transform using analysis and synthesis filter banks. A_1 and D_1 are the approximate and detail sub-bands while $\tilde{A}_1$ and $\tilde{D}_1$ are its reconstruction; H_a, G_a, H_s and G_a are the low- and high-pass analysis and synthesis filter responses, respectively and α and β are the low- and high-pass scaling factors, respectively.

To ensure that TQWT will not be overly redundant, the scaling factors, α and β are chosen to satisfy the condition,

$$0 < \beta \leq 1 \quad \text{and} \quad 0 < \alpha < 1.$$

To achieve perfect reconstruction and for the filter responses to be well localised (or oversampled), the scaling factors must satisfy

$$\alpha + \beta > 1 \tag{3.29}$$

and then the reconstructed approximate $\tilde{A}_1$ and detail $\tilde{D}_1$ sub-bands are combined,

$$\begin{aligned} Y(\omega) &= Y_{\tilde{A}_1}(\omega) + Y_{\tilde{D}_1}(\omega) \\ &= X(\omega). \end{aligned} \tag{3.30}$$

For a multi-level decomposition using the TQWT, the two channel filter bank is iteratively applied to the low-pass channel of the analysed signal. The 3-level decomposition of the TQWT is illustrated in Figure 3.10. The TQWT detail sub-band is denoted by $D_k(n)$ where $1 \leq k \leq K$ for a K-level decomposition. The first detail sub-band $D_1(n)$ is the result of high-pass filter. The sampling rate of the sub-band at level-k is $\beta\alpha^{k-1}f_s$ [100]. If one performs K-levels of decomposition, there are $(K+1)$ sub-bands (i.e K detail and one approximate sub-band).

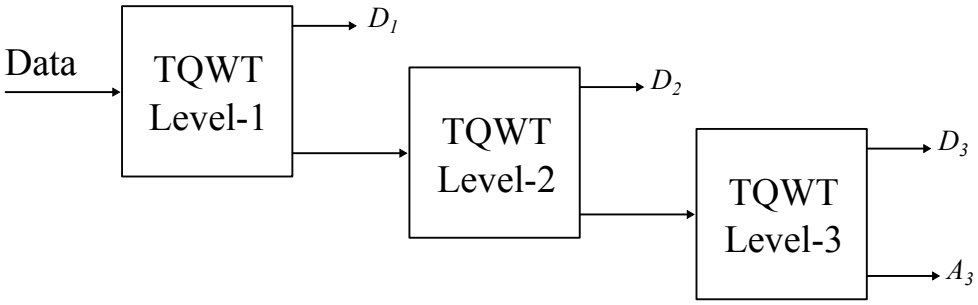

Figure 3.10. Multi-level decomposition of the TQWT for a 3 level decomposition: D_1, D_2 and D_3 are the detail sub-bands and A_3 is the approximation sub-band at level-3.

In the TQWT, varying α and β will also change the filter frequency responses. This is an advantage where one can tune the bandpass of the filter to a desired frequency range of interest for analysing a signal. The scaling parameters can also be expressed as:

$$\beta = \frac{2}{Q+1} \quad \text{and} \quad \alpha = 1 - \frac{\beta}{r}$$

where $r = \beta/(1-\alpha)$ is the oversampling rate (or redundancy) of the wavelet transform. The Q-factor is defined in terms of its centre frequency, f_c, and bandwidth, B, of the filter response,

$$Q = \frac{f_c}{B}. \tag{3.31}$$

As shown in Figure 3.11, the response is non-zero in the interval $f_1 = \frac{1}{2}(1-\beta)\alpha^{k-1}f_s$ and $f_2 = \frac{1}{2}\alpha^{k-1}f_s$. The centre frequency, f_c, at level-k is approximately the average of f_1 and f_2,

$$\begin{aligned} f_c &= \frac{1}{2}(f_1 + f_2) \\ &= \alpha^{k-1} f_s \left(\frac{2-\beta}{4}\right) \end{aligned} \tag{3.32}$$

and the null to null bandwidth, B, is given by

$$\begin{aligned} B &= \frac{1}{2}(f_2 - f_1) \\ &= \frac{1}{4}\beta\alpha^{k-1} f_s. \end{aligned} \tag{3.33}$$

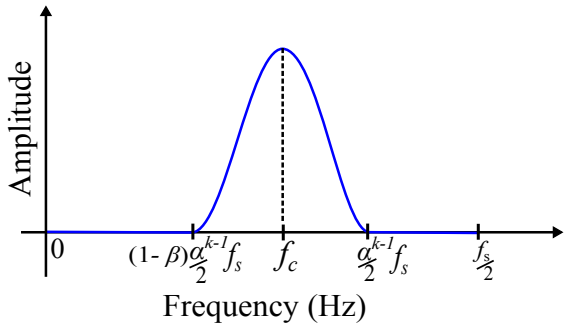

Figure 3.11. Filter frequency response of a sub-band representing the bandpass spectrum of a filter. The spectrum is limited by an interval with centre frequency, f_c. f_s is the sampling frequency.

In summary, the TQWT requires three important parameters. The Q-factor determines the 'oscillatory' nature of the wavelet. It can be varied to suit different properties of the analysed signal. For a low Q-factor, the wavelets (or filters) characterise non-sustained oscillations (broad spectrum) while a high Q-factor leads to the wavelet being more oscillatory and better able to characterise a signal with a narrow spectrum. Figure 3.12 illustrates the wavelet in the time domain (bottom row) with its frequency response (top row). For $Q = 1$, the transform becomes the second derivative of a Gaussian (Mexican hat wavelet) as shown in Figure 3.12 (bottom left) and resembles the dyadic WT. A high Q-factor implies that the wavelet is highly oscillatory. In the extreme limit, as Q approaches ∞, the result is a pure sine wave [100].

The second parameter is the redundancy factor ($r > 1$) which controls the frequency transition of the wavelet filters. Greater values of r mean the frequency response of the neighbouring sub-band filter has a greater amount of overlap [99, 100]. The third parameter is K which is the number of levels the TQWT is decomposing. For a K-level decomposition, there will be K detail and one approximate sub-band.

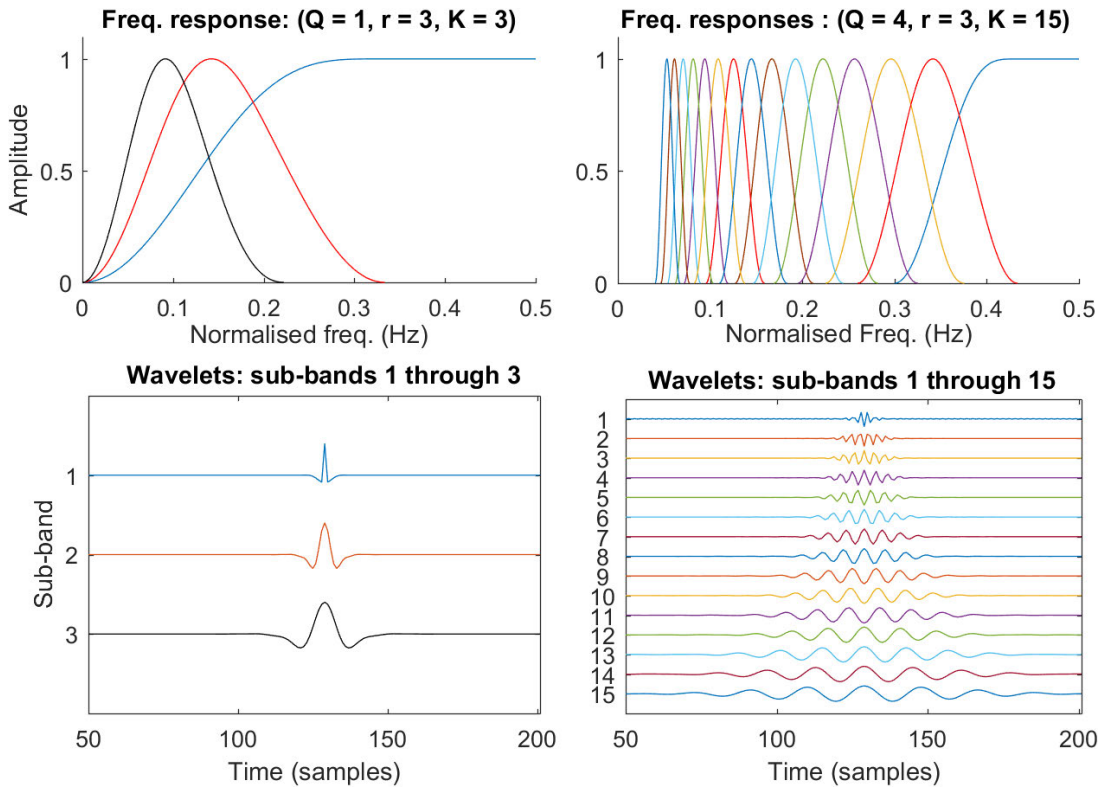

Figure 3.12. The TQWT wavelet and filter responses using parameters (left: $Q = 1, r = 3$ and $K = 3$) and (right: $Q = 4, r = 3$ and $K = 15$).

3.6 Conclusion

In this chapter, various time-frequency transforms have been discussed. The Fourier transform is a versatile tool which is suitable for stationary signals. However, many naturally occurring signals such as radar sea-clutter are non-stationary. To facilitate better analysis of these types of signals, time-frequency tools such as wavelets can be used.

The DWT is desirable for many applications such as image processing because of its fast computation and multi-resolution properties. However, downsampling in the DWT leads to a shift-variant transform which can potentially produce artefacts. To avoid these problems, a shift-invariant transform, the SWT, was proposed as an alternative.

The final part of this chapter outlined another time-frequency transform, namely the TQWT. The tuneable Q-factor of the TQWT allows a user to adjust the resonance of the wavelet to the desired frequency for a target. This unique property cannot be achieved with the conventional dyadic WT.

Chapter 4

Target Detection in Radar Sea Clutter Using Stationary Wavelet Transforms

THIS chapter investigates target detection in medium grazing angle X-band sea-clutter using 1D and 2D stationary wavelet transforms (SWT). The SWT decomposes a signal into a series of sub-bands which highlight or suppress different features of the non-stationary sea-clutter. Once they have been individually reconstructed back to the data domain, both the amplitude statistics and their relative detection performance are investigated. To determine which reconstructed sub-band contains the most information about the target, an indication scheme using an 'entropy' based metric is proposed. A Monte-Carlo simulation using a cell-averaging constant false alarm rate algorithm is then implemented to demonstrate and quantify the detection improvement.

4.1 Introduction

In maritime radar target detection, a good statistical representation of the backscatter is important to both minimise false detections and maximise the probability of detection. However, the radar backscatter may contain sea-spikes which can last for seconds and cause false detections [64, 87, 124]. One potential solution to this problem is through the use of time-frequency representations. The goal of this chapter is to investigate how a particular time-frequency technique, the wavelet transform (WT) can potentially reduce the impact of sea-spikes on target detection and improve the detection performance.

There have been a number of studies into the use of WTs to improve target detection in sea-clutter. Ehara et al. [39] proposed two methods to improve the signal to noise ratio (SNR) of the radar echo return. The first is based on the idea that given an optimal scale, the wavelet function can approximate a matched filter and therefore improve target detection. The second method extends this idea by integrating a small range of wavelet coefficients around the optimal scale. This method provides more robustness and was shown to improve the SNR even further. Ball and Tolley [9] proposed an automatic algorithm to determine the optimal scale parameter, which required searching for the peak in the continuous WT coefficients, followed by a de-noising procedure around the optimum scale. They achieved an average SNR improvement of up to 10 dB when compared to a conventional matched filter. Zhang et al. [133] also used WTs for radar target detection and found that removing some of the high frequency 'detail' wavelet coefficients is effective in reducing the noise of radar echoes and thus improve detection performance. In this approach, the discrete wavelet transform (DWT) sub-bands suffer from reduced detail (resolution), so the authors applied an independent component analysis to the wavelet coefficients to improve the performance. However, with a single simulation and limited experimental details, it is unclear whether this approach is effective for a broader range of signals. Another wavelet-based approach was proposed by Davidson et al. [29], who used a continuous WT to identify the dominant scatterers in a given scenario. The authors then applied a 'persistence' statistic to detect slow-moving targets from the surrounding backscatter. Wavelets have also found their way into radar image processing, based on their de-noising ability. Jangal et al. [53] used a DWT and subsequent selective reconstruction (by ignoring some sub-bands) to process range Doppler images of a high-frequency surface wave radar and suppress interference.

In contrast to the existing wavelet-based schemes, this chapter investigates target detection in medium grazing angle X-band sea-clutter using 1D and 2D stationary wavelet transforms (SWT). One level of the SWT produces a series of sub-bands which represents different

features of the non-stationary sea-clutter. Once they have been individually reconstructed back to the data domain, both the amplitude statistics and their relative detection performance are investigated. Higher levels of the SWT decompositions are then explored to further improve the detection performance. To determine which sub-bands contain the most information about the target, an indication scheme based on 'entropy' is proposed.

To quantify the detection improvement, a Monte-Carlo simulation using a cell-averaging constant false alarm rate algorithm (CA-CFAR) is implemented. The comparisons between processed and unprocessed data are investigated with both HH and VV polarisations. To demonstrate robustness of the detection scheme, different target velocities and amplitude fluctuations are also investigated.

This chapter is organised as follows. Section 4.2 outlines the Ingara data used for the experiment and Section 4.3 provides background on the SWT. An analysis of both 1D and 2D SWTs is then provided in Section 4.4. Section 4.5 compares the detection performance using both mean separation and a Monte-Carlo simulation using the CA-CFAR algorithm. The multi-level decomposition of the SWT is then investigated in Section 4.6. Section 4.7 defines 'entropy' and proposes a sub-band indication scheme to select the sub-band with the most information about the target. Section 4.8 demonstrates the detection performance with the proposed scheme. Finally, a summary of the chapter is given in Section 4.9.

4.2 Ingara Data Set

A short summary of the data is outlined here while more detail of the data and trial can be found in Section 2.5.1. The Ingara medium grazing angle sea-clutter data set was collected by the Defence Science and Technology (DST) Group in 2004 and 2006 [25]. During the trials, the backscatter was collected over 360° of azimuth and between $15^\circ - 45^\circ$ in grazing. The X-band radar had a pulse repetition frequency (PRF) of 575 Hz and used a 200 MHz bandwidth giving 0.75 m range resolution. At a slant range of 3.4 km and with a 1° two-way 3 dB azimuth beamwidth, the azimuth resolution was approximately 63 m.

For the experiment in this chapter, the dual polarised data set has been chosen from the 2006 trial with a Douglas sea state between 4 and 5. The polarisation is horizontal and a coherent processing interval (CPI) of 128 pulses (or 0.2 s) is chosen from the upwind direction covering 430 m with grazing angles between $30.5^\circ - 35.5^\circ$.

4.3 Stationary Wavelet Transform

This section provides a short review of the SWT with further details provided in Chapter 3. Wavelet transforms have been used for signal processing in various applications to obtain compact representations of non-stationary signals. They have the ability to represent signals at multiple scales, or *resolutions*, with an adaptive time window, thus offering a different partitioning of the time frequency plane compared to techniques such as the short time Fourier Transform [27, 68, 117]. The analysing functions in wavelet transforms are dilated (by factor a) and shifted (in time by b) versions of the same wavelet function $\psi(t)$,

$$\psi_{a,b}(t) = \frac{1}{\sqrt{a}}\psi\left(\frac{t-b}{a}\right). \tag{4.1}$$

A valid wavelet function must have a bandpass spectrum (zero average), and is thus a set of oscillations over a limited duration in the time domain. The SWT is a translation-invariant transform [74, 80, 105]. It is a non-decimated transform, and has been used successfully in applications which may be sensitive to artefacts that arise from the more popular, decimated version of the WT [20, 74, 80].

High level analysis of the SWT separates the non-stationary sea-clutter data into different sets of detail (projections onto wavelet functions, $\psi_{a,b}(t)$) and approximation (scaling function) coefficients, called *sub-bands*. Each of these coefficients corresponds to a unique region of the time-frequency plane. It is reasonable to expect interference and target returns would produce different distributions of coefficients, thus allowing them to be separated in the coefficient domain.

The SWT signal decomposition algorithm is commonly implemented as cascaded two-channel filter banks, with each filter bank consisting of a pair of complementary low-pass and high-pass filters. The filter bank at level $k > 0$ accepts the approximation sub-band at level $k-1$ as an input and produces detail (D_k) and approximation (A_k) sub-bands at the outputs of the high- and low-pass filters, respectively. The data input is equivalent to the A_0 sub-band, with subsequent levels:

$$A_k(n) = \sum_{m=-\infty}^{\infty} h_a(n-m)A_{k-1}(m), \tag{4.2}$$

$$D_k(n) = \sum_{m=-\infty}^{\infty} g_a(n-m)A_{k-1}(m), \tag{4.3}$$

where $h_a(n)$ and $g_a(n)$ are the impulse responses of the low- and high-pass filters. The process can be reversed to perform reconstruction by

$$A_k(n) = \sum_{m=-\infty}^{\infty} h_s(n-m)A_{k+1}(m) + \sum_{m=-\infty}^{\infty} g_s(n-m)D_{k+1}(m) \tag{4.4}$$

where h_s and g_s are the low- and high-pass synthesis filters, respectively. Since the SWT is a discretised transform, it follows that the dilation factor in Equation (4.1) is $a = 2^k$ and the time index of the analysed signal is $b = 2^k m$. The decomposition and reconstruction processes are illustrated in Figure 4.1.

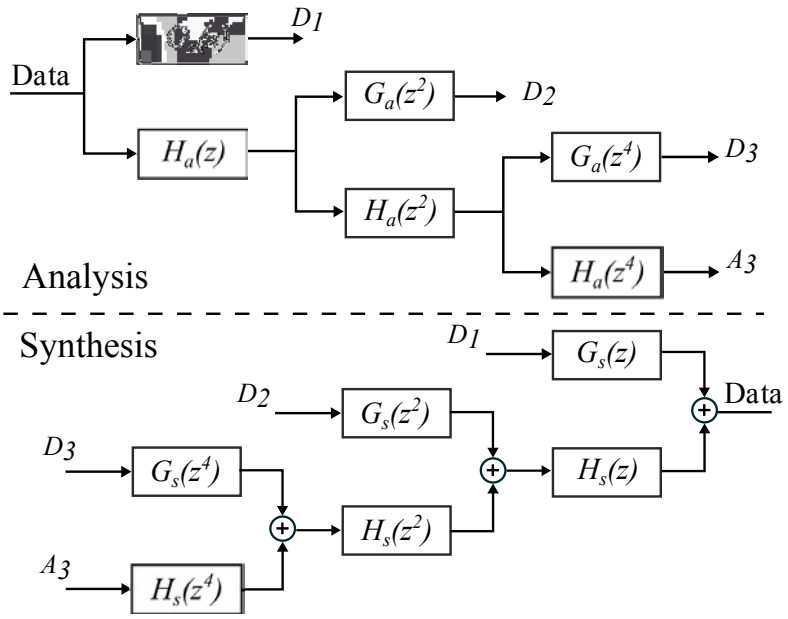

Figure 4.1. Three levels of 1D SWT analysis (top) and synthesis filtering (bottom). $H_a(z), G_a(z), H_s(z)$ and $G_s(z)$ are the transfer functions or z-transform of the complementary analysis and synthesis low- and high-pass filters $h_a(n), g_a(n), h_s(n)$ and $g_s(n)$, respectively.

Breaking waves can be physically large and their corresponding radar backscatter can spread over more than one range bin. Moreover, the backscatter is correlated in both range and time. A 2D SWT is computed by performing 1D transforms along rows and columns separately, as illustrated in Figure 4.2. The result after low-pass filtering is the approximate sub-band (or a lower resolution version) of the original 2D data. For high level decompositions of a 2D SWT, the approximate sub-band is further decomposed in the same manner as the first level. Further explanation of the 2D SWT is given in Chapter 3.

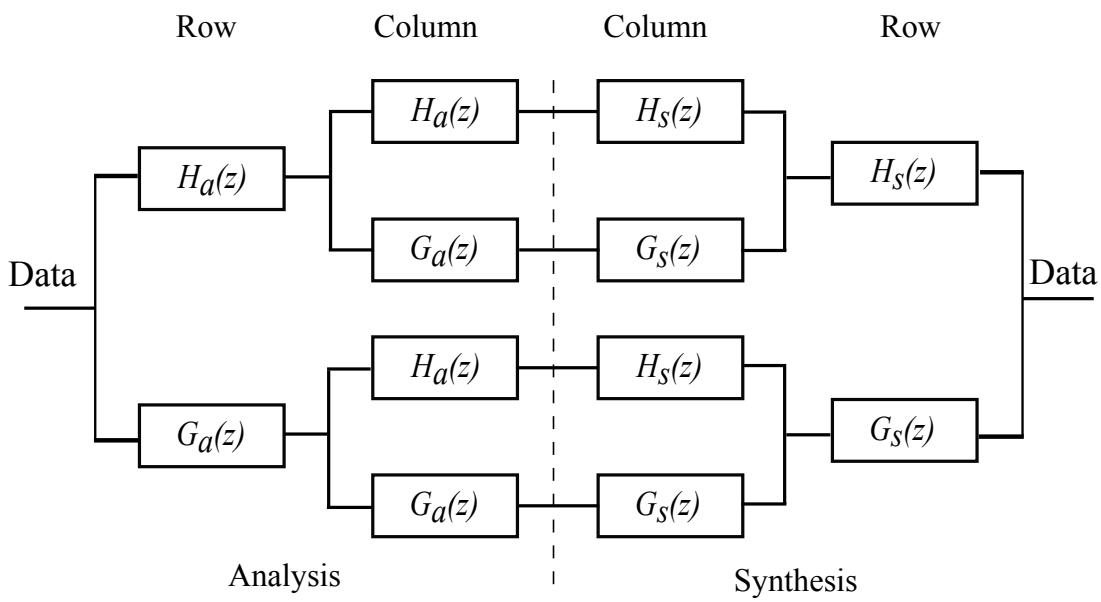

Figure 4.2. Block diagram of the first level signal decomposition and reconstruction using a 2D SWT. $H_a(z), G_a(z), H_s(z)$ and $G_s(z)$ are the transfer functions of the complementary analysis and synthesis low- and high-pass filters $h_a(n), g_a(n), h_s(n)$ and $g_s(n)$, respectively.

4.3.1 Wavelet Selection

Application of the SWT requires selection of a mother wavelet function (or filter). A set of filters $\{h_a, g_a, h_s, g_s\}$ must be designed together to achieve perfect (error-free) reconstruction. The literature describes numerous sets of wavelet filters, each designed to satisfy different properties [3, 68, 111, 112]. Some popular wavelets include Daubechies, Morlet, Mexican hat, Meyer, Biorthogonal and Symlets [27, 68].

Different filters can reveal specific information of a particular signal [3, 68]. A comprehensive survey of the performance of different wavelets is beyond the scope of this thesis. Instead, the popular Daubechies-4 wavelet is chosen for the analysis of the radar backscatter, based on earlier work [53, 62, 112, 121]. The impulse responses for the corresponding filters are shown in Figure 4.3. Wavelets of this family are characterised by short finite impulse response (FIR) filters in the corresponding 2-channel filter bank. One advantage of short FIR filters is reduced ringing which helps with localising fluctuating targets in slow-time and is computationally fast.

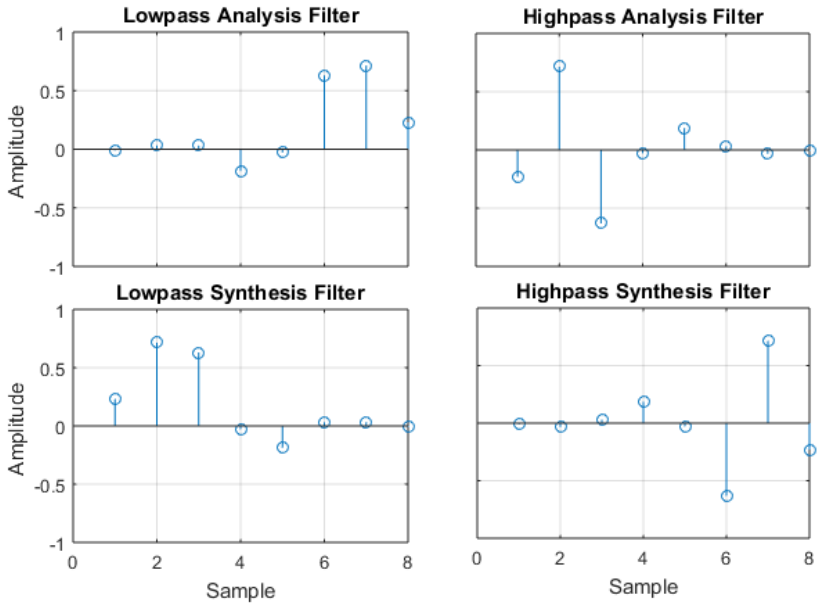

Figure 4.3. The impulse responses of the analysis and synthesis low- and high-pass Daubechies-4 wavelet filters $\{h_a, g_a, h_s, g_s\}$.

4.3.2 Sub-band Reconstruction

The SWT decomposition performed on the data leads to a number of different sub-bands. The components of the interference and target (if present) generally have different distributions of SWT coefficients across sub-bands. This implies that one or more sub-bands have a stronger signal to interference ratio (SIR) than the original data. It is based on this observation that we propose the use of a subset of SWT sub-bands for target detection. In order to combine the information from this subset, we perform a reconstruction back to the original time domain, choosing to retain only those selected sub-bands. This is equivalent to using zero inputs for the rejected sub-bands in the synthesis algorithm.

The *sub-band isolation and reconstruction* procedure is illustrated in Figure 4.4. The approximate reconstructed sub-band, denoted by $\tilde{A}_1$, is the result of low-pass filter and the detail reconstructed sub-band, denoted by $\tilde{D}_1$, is the result of high frequency sub-band. In the frequency domain, the first level decomposition can be interpreted as general low- and high-pass filtering. Figure 4.5 shows the frequency bandwidth of the two reconstructed sub-bands. The $\tilde{A}_1$ reconstructed sub-band retains the low frequency part, while the $\tilde{D}_1$ reconstructed sub-band contains the high frequency part of the data spectrum.

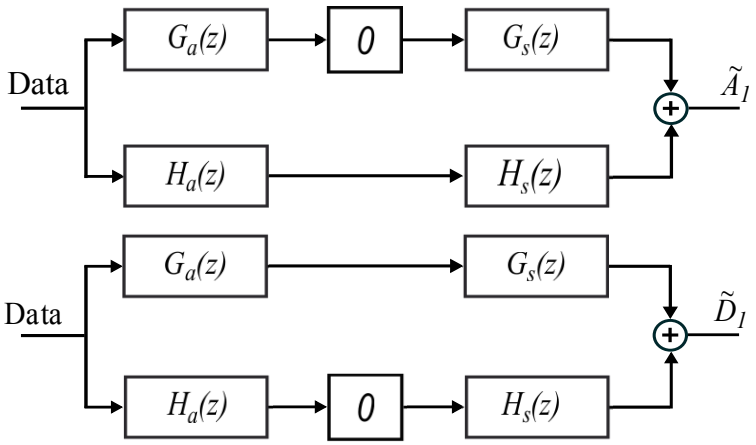

Figure 4.4. Data decomposition with sub-band isolation and reconstruction using the 1D SWT: $\tilde{A}_1$ and $\tilde{D}_1$ are the approximate and detail reconstructed sub-bands of the original data.

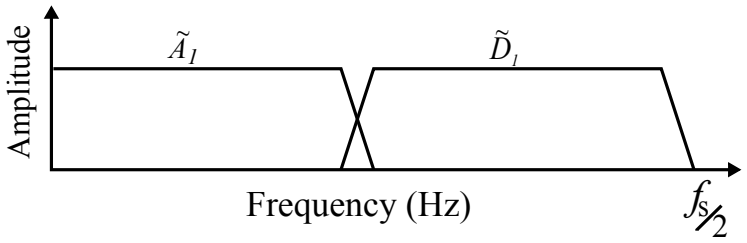

Figure 4.5. The reconstructed sub-band bandwidth from Figure 4.4: low-pass reconstructed sub-band $\tilde{A}_1$ and high-pass reconstructed $\tilde{D}_1$. f_s is the signal sampling frequency and $\frac{f_s}{2}$ is the corresponding Nyquist frequency.

4.4 Sea Clutter Analysis Using SWTs

In this section, both 1D and 2D SWTs are applied to the Ingara sea-clutter using the sub-band isolation and reconstruction method. Various characteristics of sea-clutter are then investigated. The section also illustrates the impact of the SWT with and without a target.

4.4.1 1D SWT Implementation

The first example is a 1D SWT decomposition of the complex (in-phase and quadrature) radar backscatter along range. A single level SWT using the Daubechies-4 wavelet is investigated. The data has a CPI of 128 pulses or time history of about 0.2 seconds. Each of the resultant sub-bands are then isolated (i.e. by setting the others to zero) and individually reconstructed to

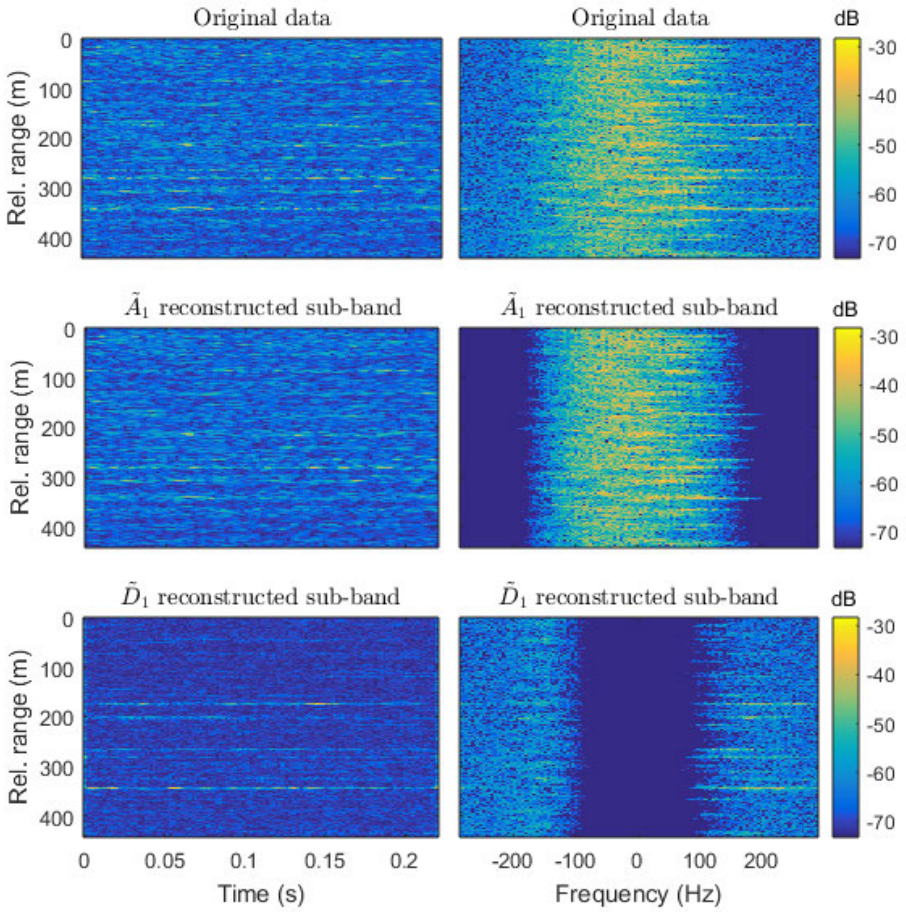

Figure 4.6. Time and frequency (power spectral density (PSD)) domain representations after sub-band isolation and reconstruction of the HH polarisation.

the data domain. As a result, two sub-bands are achieved: approximate and detail reconstructed sub-bands denoted by $\tilde{A}_1$ and $\tilde{D}_1$, respectively. For visualisation, Figure 4.6 shows an example of the 1-level decomposition and sub-band reconstruction using the 1D SWT along slow time. The approximate reconstructed sub-band $\tilde{A}_1$ only retains the low frequency part of the data spectrum while the detail reconstructed sub-band $\tilde{D}_1$ contains the high frequency part.

To quantify the changes in the interference, K and K+Rayleigh distributions have been fitted to the original data and then to each of the reconstructed sub-bands. Figure 4.7 shows these fits to the HH polarisation: original data (top row), reconstructed sub-bands $\tilde{A}_1$ (middle row) and $\tilde{D}_1$ (bottom row). The original data and the reconstructed sub-bands in the time domain are shown in the first column while their PDFs are shown in the second column with the original data shown in blue, the K-distribution in red and the K+Rayleigh distribution in black.

Table 4.1. K and K+Rayleigh distribution parameter estimates of the original and 1D reconstructed sub-bands.

Model		K				K+Rayleigh			
Polarisation		HH	HV	VH	VV	HH	HV	VH	VV
Original Data	CNR (dB)	15.0	8.0	10.7	23.0	15.0	8.0	10.7	23.0
	k_r	-	-	-	-	0.5	0.8	0.8	0.8
	shape	2.9	8.3	9.2	32.0	0.5	0.2	0.2	1.7
Sub-band $\tilde{A}_1$	CNR_r (dB)	-	-	-	-	∞	-5.9	-6.2	-2.8
	shape	3.0	6.1	4.6	50	14.8	0.1	0.07	39.0
Sub-band $\tilde{D}_1$	CNR_r(dB)	-	-	-	-	∞	∞	∞	∞
	shape	0.7	0.9	0.9	0.9	0.7	0.9	0.9	0.9

The results from the experiments reveal that the K-distribution has a mismatch in the tail for each result. The K+Rayleigh distribution, on the other hand, has better fits for the original data and the two reconstructed sub-bands. Notice that when fitting the K+Rayleigh distribution in the detail reconstructed sub-band, there is a mismatch or the ”kink” in the curve around -30 dB. This illustrates that it is hard to represent data with just a few large clutter spikes in it. Despite the mismatch, the K+Rayleigh distribution is still able to fit the tail of the data very well, which is important for threshold estimation in a radar detection scheme.

The spikiness of the original data and the reconstructed sub-bands can be implied from the shape parameters, with higher shape values indicating that the data is less spiky [87, 124]. The shape parameters are estimated using the zlogz estimator described in Section 2.3.3. Table 4.1 shows the estimated parameters for the 4 polarisations (HH, HV, VH and VV). The $\tilde{A}_1$ reconstructed sub-bands typically have larger shape values implying less spiky clutter. However, the $\tilde{D}_1$ reconstructed sub-bands have lower shape values, indicating that the data is spikier. The results are understandable because the detail reconstructed sub-bands retain the high frequency components which contain mostly sea-spikes and noise. There are also some CNR_r values which are ∞ due to the noise plus Rayleigh mean power being estimated as 0.

To test the potential impact of the 1D SWT on targets, the sub-band isolation process is repeated on the data with simulated targets present. They have a constant RCS with a signal to interference ratio (SIR) of 10 dB. Both a stationary and moving target with a velocity of 2.6 m/s are injected into the HH polarisation at relative ranges 214 m and 230 m, respectively as shown in Figure 4.8. The stationary target is located at the centre of the clutter region while the moving target is situated at the exo-clutter of the clutter region (i.e the target moves faster

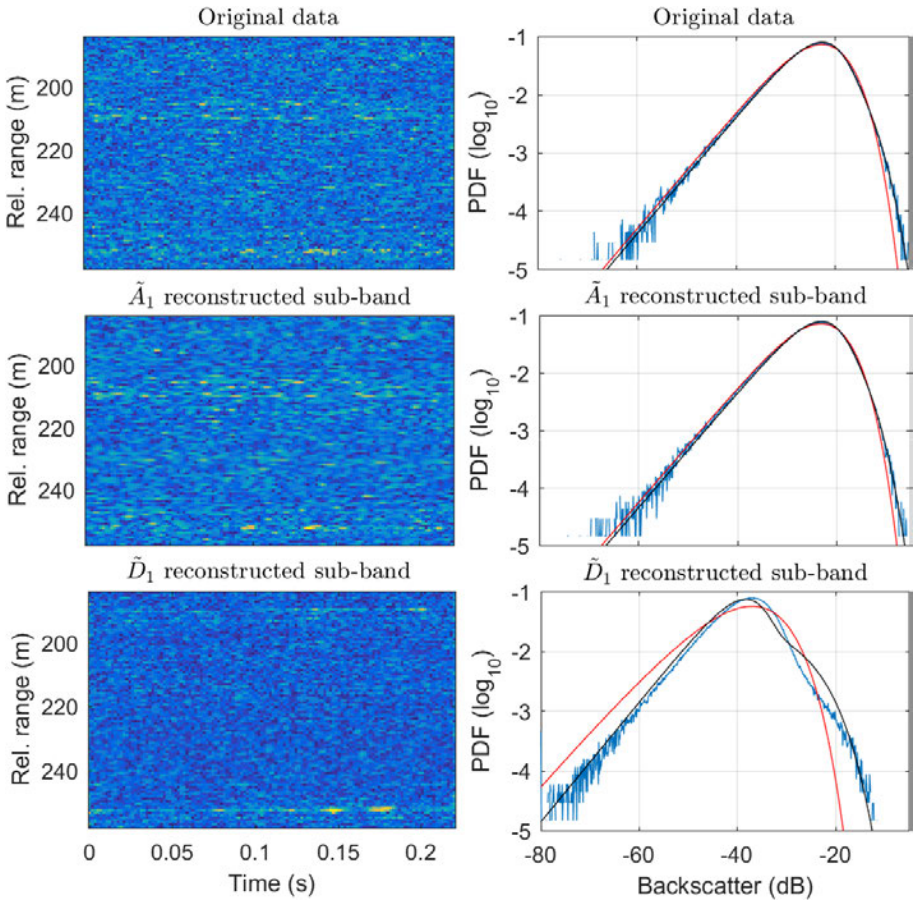

Figure 4.7. Original and reconstructed sub-bands ($\tilde{A}_1$ and $\tilde{D}_1$) are shown on the left and its corresponding PDFs are shown on the right: the original data (blue) with K-distribution (red) and K+Rayleigh (black) distribution.

than sea-waves). The stationary target is maintained in the $\tilde{A}_1$ reconstructed sub-band image, while it is not visible at all in $\tilde{D}_1$. When the target is moving however, this result switches and the target is now clearly visible in the $\tilde{D}_1$ reconstructed sub-band. The moving target appears to be stronger (or brighter) than the original unprocessed data.

4.4.2 2D SWT Implementation

To implement the 2D SWT, a series of SWTs using the same Daubechies-4 wavelet are performed on the 2D radar backscatter in the range / time domain as described in Section 3.4.4. Following the 2D decomposition, 4 sub-bands (LL_1, LH_1, HL_1 and HH_1) are produced. The LL_1 sub-band is the result of low-pass filtering along rows and then columns. LH_1 is the result of low-pass filtering along rows and then high-pass filtering along columns,

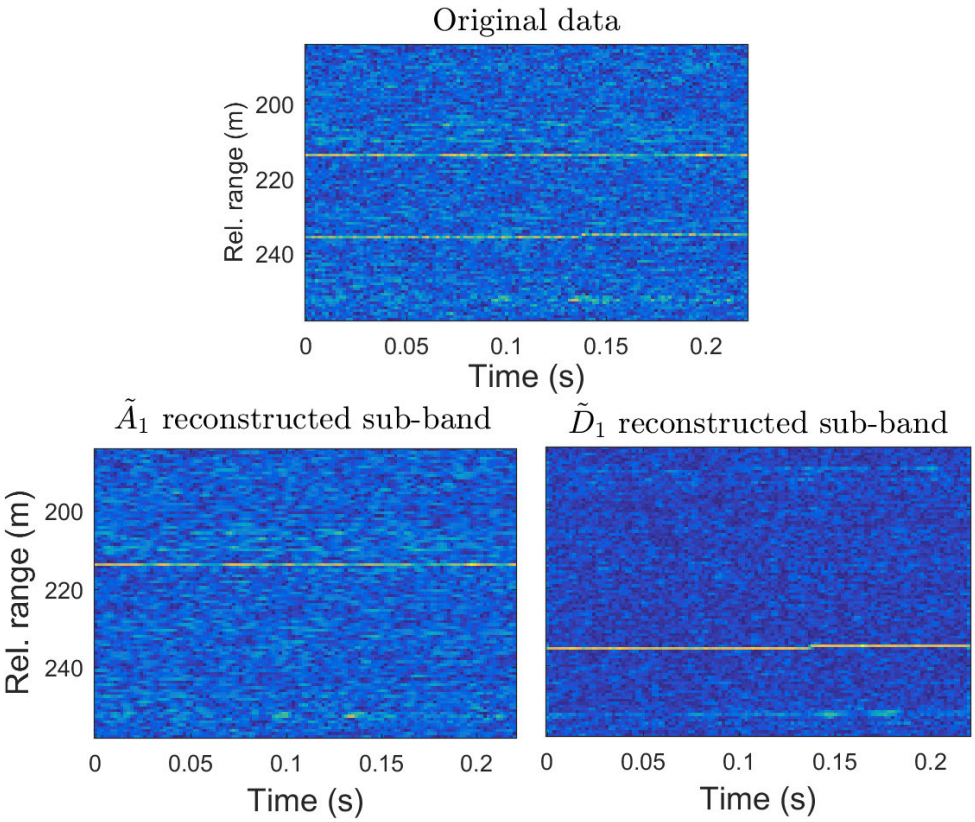

Figure 4.8. Range/time data (top) of the HH polarisation with a simulated stationary and moving target at radial velocity 2.6 m/s in range bins 214 m and 230 m, respectively. The $\tilde{A}_1$ and $\tilde{D}_1$ reconstructed sub-bands are shown in the bottom left and right.

HL_1 is high-pass filtering along rows and low-pass filtering columns and finally HH_1 is high-pass filtering along rows and then columns.

Each of the resultant sub-bands after decomposition are then isolated and individually reconstructed back to the data domain. Four reconstructed sub-bands are achieved and denoted by $\tilde{LL}_1, \tilde{LH}_1, \tilde{HL}_1$ and $\tilde{HH}_1$. These sub-bands are shown in Figure 4.9 and are known as the approximate, horizontal, vertical and diagonal reconstructed sub-bands. The figure shows that each reconstructed sub-band contains some strong components in both range and time. The reconstructed sub-bands also reveal some features which are not seen in the original data. For instance, the $\tilde{LL}$ reconstructed sub-band (top left of Figure 4.9) shows many strong components which are not seen in the original data.

Figure 4.10 also shows the fitting of K and K+Rayleigh distributions for the 4 reconstructed sub-bands. Firstly, these results reveal that the K-distribution fits $\tilde{LL}_1$ and $\tilde{LH}_1$ reasonably well, while there are large mismatches in the tail for $\tilde{HL}_1$ and $\tilde{HH}_1$. The K+Rayleigh distribution, on the other hand, fits the data in all sub-bands well.

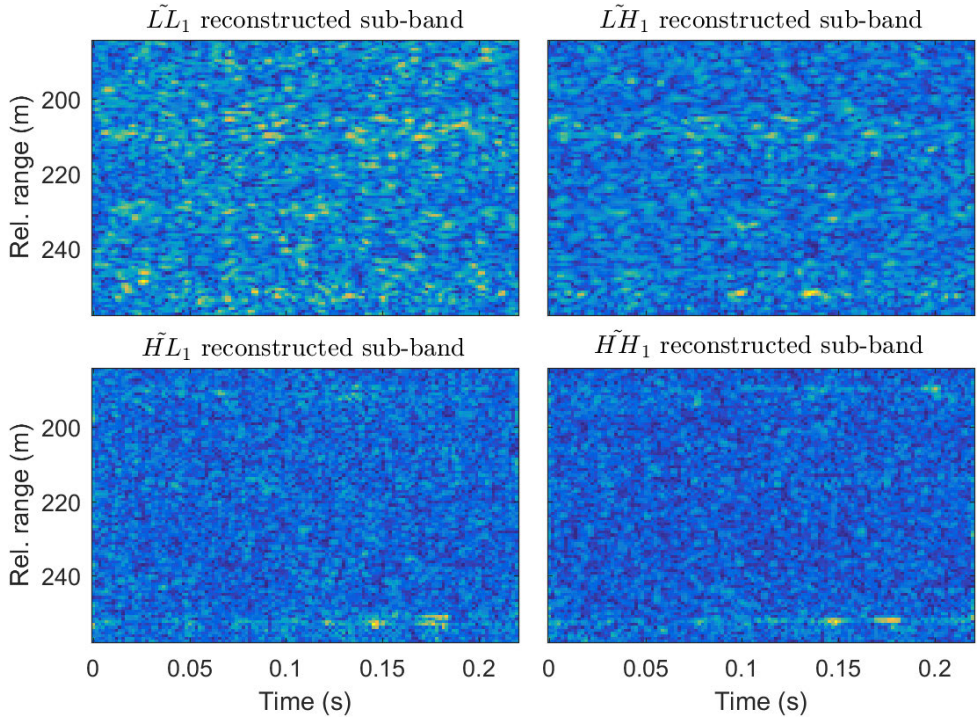

Figure 4.9. Reconstructed sub-bands using the 2D SWT: $\tilde{LL}_1, \tilde{LH}_1, \tilde{HL}_1$ and $\tilde{HH}_1$.

To investigate the variation in the interference after the 2D SWT, the shape parameters are estimated. Table 4.2 shows the shape parameters of the four reconstructed sub-bands when fitting the K and K+Rayleigh distributions. It is found that the overall shape parameters in the $\tilde{LL}$ and $\tilde{LH}$ sub-bands are larger than the original data and the $\tilde{HL}$ and $\tilde{HH}$ sub-bands. With this analysis, there were some cases when the shape estimates of the K+Rayleigh distribution using the zlogz estimator produce poor results. In this case, a least square model fit is used to estimate the shape (see Section 2.3.3 for more detail).

The 2D SWT is also applied to the data with injected targets. The sub-band isolation and reconstruction procedure is then repeated with the constant target RCS having an SIR of 10 dB. Both a stationary and moving target with a velocity of 2.6 m/s are injected into the HH polarisation at relative ranges of 214 m and 230 m, respectively. Figure 4.11 shows the original data (top) and the 4 reconstructed sub-bands. It can be observed that the stationary target is maintained in the $\tilde{LL}_1$ and $\tilde{LH}_1$ reconstructed sub-bands, which are the low-pass sub-bands of the original data. The target is not visible in both high-pass reconstructed sub-bands: $\tilde{HL}_1$ and $\tilde{HH}_1$. When the target is moving this result switches and the moving target is now clearly visible in the $\tilde{HL}_1$ and $\tilde{HH}_1$ reconstructed sub-band images. However, both targets smear vertically across multiple ranges due to the filter processing along columns.

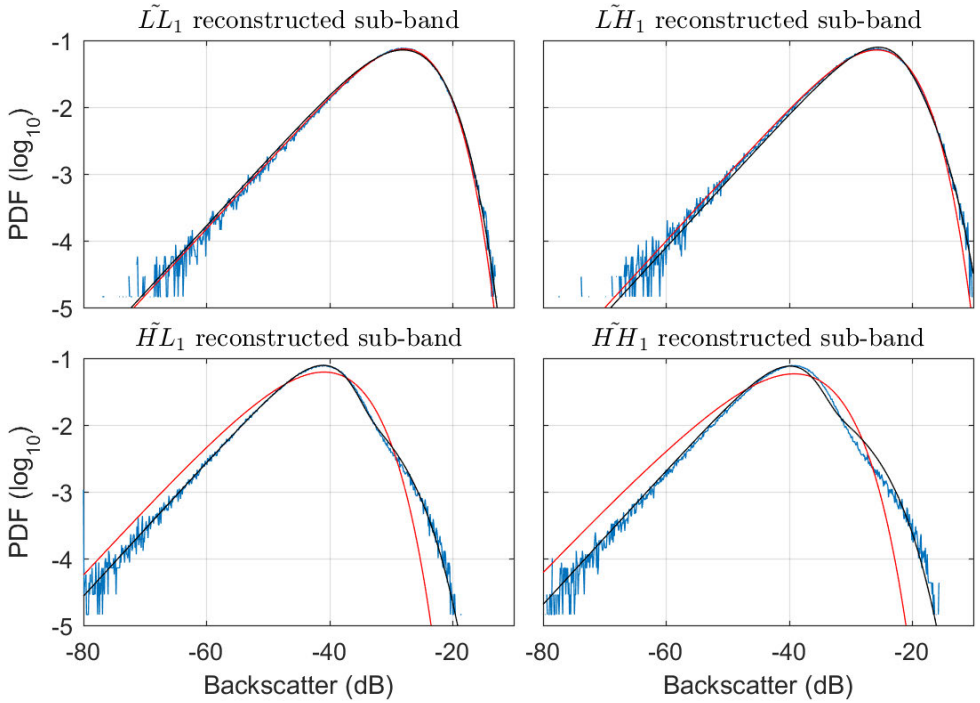

Figure 4.10. PDF fitting of the 4 SWT reconstructed sub-bands ($L\tilde{L}_1, L\tilde{H}_1, H\tilde{L}_1$ and $H\tilde{H}_1$): the interference is represented by blue, while K and K+Rayleigh distributions are shown in red and black, respectively.

4.5 Detection Comparison Using 1D and 2D SWTs

4.5.1 Mean Separation

One method to measure the potential detection improvement is to calculate the mean difference between the interference only and the interference with an injected target. A larger mean or PDF separation indicates that the target is more likely to be successfully detected. In this section, we measure the mean separation for both 1D and 2D reconstructed sub-bands.

For this exercise, a constant target is injected to all range bins of the HH polarisation. The PDFs of the data with and without the target are then plotted. Figure 4.12 shows the PDFs of the original data (top) and $\tilde{A}_1$ and $\tilde{D}_1$ of the 1D SWT in the middle and bottom, respectively. Figure 4.13 shows the 2D SWT for the original data (top) followed by the four reconstructed sub-bands: $L\tilde{L}_1, L\tilde{H}_1, H\tilde{L}$ and $H\tilde{H}$, respectively. The blue line denotes the interference only PDF, the dash red line denotes the stationary target plus interference PDF and the dash-dot black line denotes the moving target plus interference PDF. Note that for the original data, the PDFs

Table 4.2. K and K+Rayleigh estimated parameters of the 2D SWT sub-bands.

Model		K				K+Rayleigh			
Polarisation		HH	HV	VH	VV	HH	HV	VH	VV
Sub-band $\tilde{LL}_1$	CNR_r (dB)	-	-	-	-	∞	-5.4	-5.3	-3.5
	shape	3.1	6.8	4.7	50.0	52.0	0.06	0.04	50.0
Sub-band $\tilde{LH}_1$	CNR_r (dB)	-	-	-	-	∞	∞	∞	∞
	shape	0.7	0.8	0.8	0.9	0.7	0.8	0.8	0.9
Sub-band $\tilde{HL}_1$	CNR_r (dB)	-	-	-	-	22.8	∞	∞	∞
	shape	0.7	0.9	0.9	0.7	0.7	0.9	0.9	0.7
Sub-band $\tilde{HH}_1$	CNR_r (dB)	-	-	-	-	∞	∞	∞	∞
	shape	0.7	0.9	0.9	0.7	0.7	0.9	0.9	0.7

of the stationary and moving targets are identical and for the $\tilde{D}_1, \tilde{HL}$ and $\tilde{HH}$ reconstructed sub-bands, the red lines are on top of the blue lines.

Figure 4.12 shows that the PDF separation for the stationary target is slightly bigger than the unprocessed data in the $\tilde{A}_1$ reconstructed sub-band, while the moving target shows poor separation. These results are reversed for the $\tilde{D}_1$ reconstructed sub-band. There is no separation for the stationary target (the dash red line sits on top of the blue line) while an extremely large separation is observed for the moving target. The results demonstrate the 2-channel filtering of the SWT, where the approximate sub-band contains the low frequency components while the reconstructed detail sub-band contains the high frequency parts. When a target is not in the filtering bandwidth, the reconstructed sub-band will only contain interference.

For the 2D SWT case in Figure 4.13, similar results are achieved. The $\tilde{LL}_1$ and $\tilde{LH}_1$ reconstructed sub-bands provide similar separation to the unprocessed data for the stationary target, while the $\tilde{HL}_1$ and $\tilde{HH}_1$ reconstructed sub-bands provide a large improvement for the moving target.

To quantify the PDF separation for each sub-band of the 1D and 2D SWTs, the relative difference in means between the interference and the target plus interference distributions are computed. Tables 4.3 and 4.4 show the reconstructed sub-band mean separation for both the 1D and 2D SWTs, respectively. The tables reveal that for the stationary target, the biggest mean separation is observed in the $\tilde{A}_1$ reconstructed sub-band while the $\tilde{LL}_1$ and $\tilde{LH}_1$

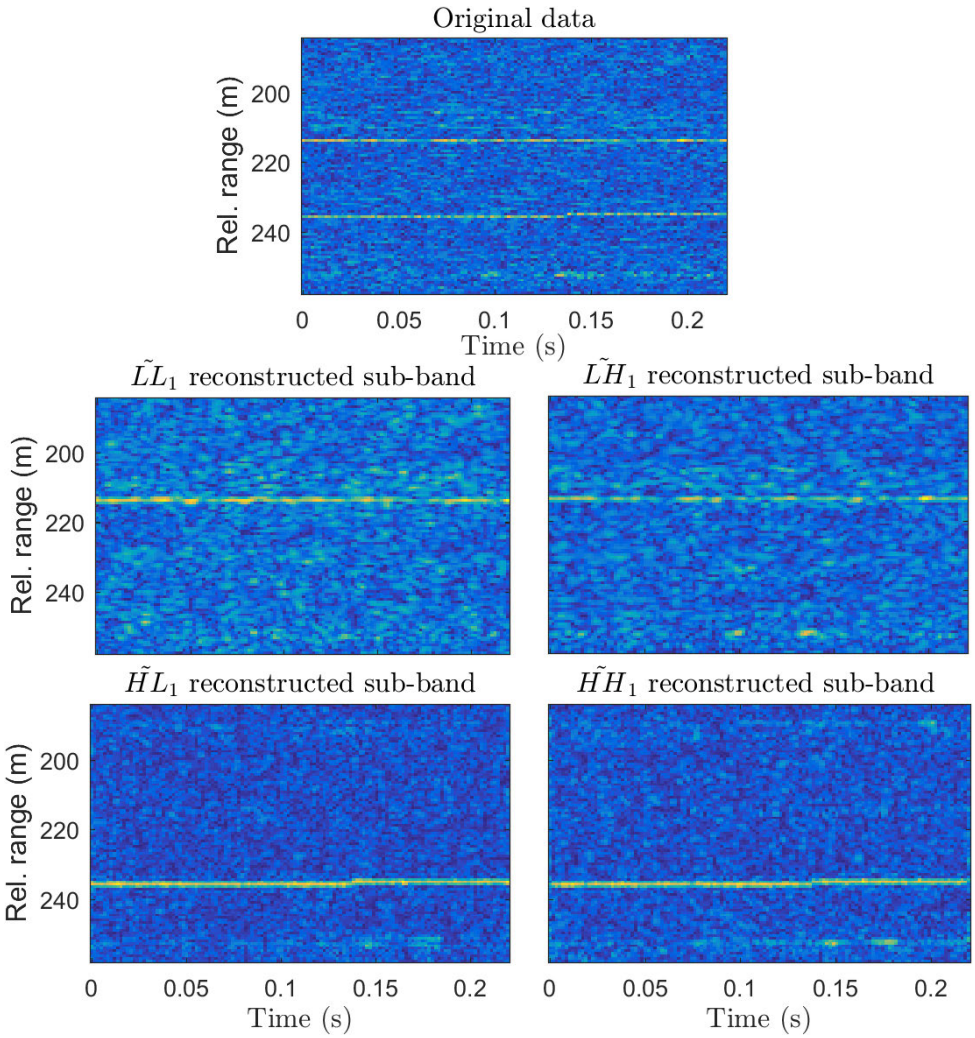

Figure 4.11. 2D SWT of the HH polarisation with two injected targets for the original data (top) and the four reconstructed sub-bands. Top target is stationary and bottom target is moving with 2.6 m/s radial velocity.

reconstructed sub-bands are slightly lower than the unprocessed data. For the moving target, the $\tilde{D}_1$ reconstructed sub-band of the 1D SWT performs best followed by $\tilde{HH}_1$ and $\tilde{HL}_1$ of the 2D SWT, respectively. Based on this analysis, we expect that the 1D SWT will outperform the 2D SWT when used for detection.

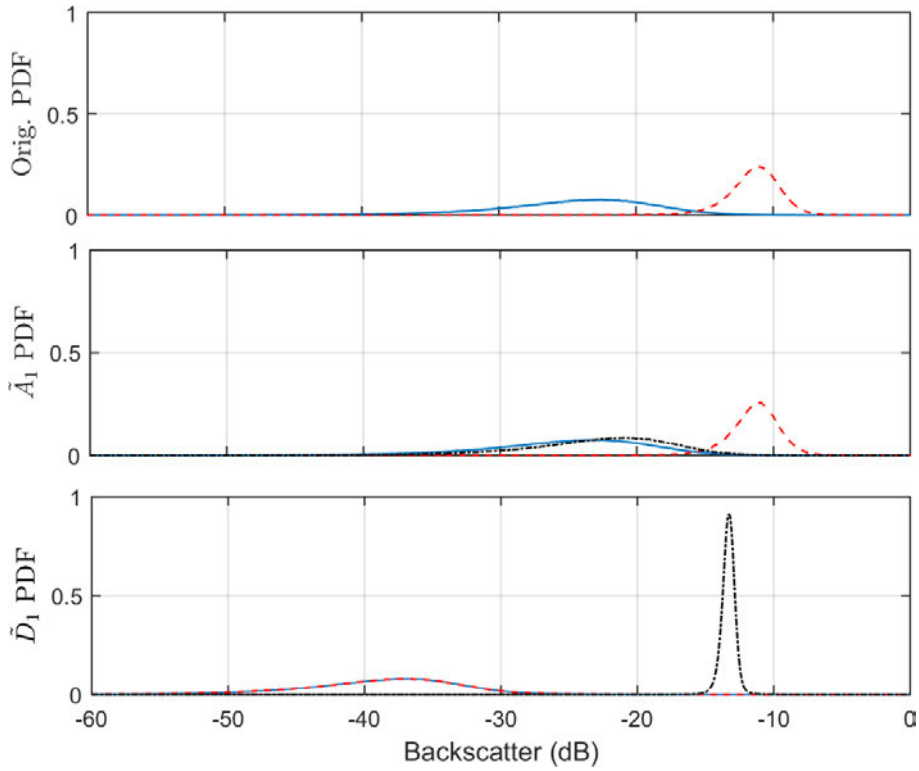

Figure 4.12. PDF separation of the original data and the reconstructed sub-bands of the 1D SWTs for stationary and moving targets in the HH polarisation. The original data PDF is in blue while the PDFs of stationary and moving targets with interference are in dash red and dash-dot black, respectively. For the original data, PDFs of stationary and moving target with interference are the same.

4.5.2 Monte-Carlo Simulation

To further compare and quantify detection performance using the 1D and 2D SWTs, a non-coherent detection scheme is investigated with a Monte-Carlo simulation. This is implemented by repeatedly injecting targets at each range bin of the data. The target SIR is then varied and the detection scheme is run with an adaptive threshold determined by the CA-CFAR algorithm. The probability of detection is then determined by counting the number of detections which cross the threshold. The detection results from the 1D and 2D SWTs are finally compared against unfiltered data.

For this comparison, two constant RCS targets having radial velocities (0 and 2.6 m/s) are illustrated. The data used for comparison comprises a CPI of 128 pulses and 200 range bins. The scheme is applied to each polarisation with HH polarisation being used for the examples. Results for the other polarisations (HV, VH and VV) are given in Appendix A.

CA-CFAR Algorithm

A CA-CFAR algorithm is implemented at the output of each detector with the results compared by looking at the improvement in SIR for a given probability of detection, P_{d}. It is applied along range to determine a threshold which adapts to the local clutter in order to maintain a constant false alarm rate. It is implemented with $G = 2$ guard bins adjacent to the cell under test to avoid target self nulling and $M_r = 32$ range bins to determine the local mean. Refer to Section 2.4.2 for more detail.

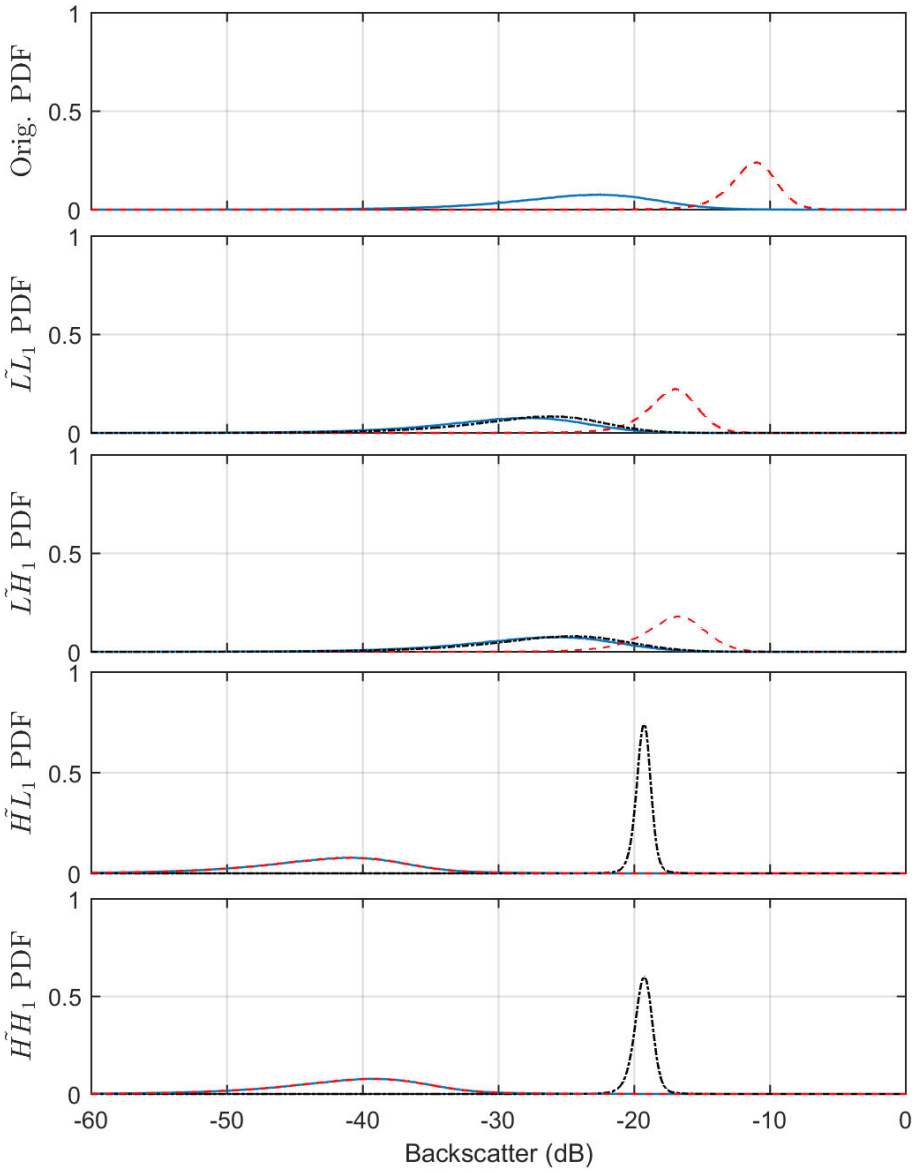

Figure 4.13. PDFs for the original data and the reconstructed sub-bands of the 2D SWT for stationary and moving targets in HH polarisation. The original data PDF is in blue, while the PDFs of stationary and moving targets with interference are in red and black, respectively. For the original data, PDFs of stationary and moving targets with interference are the same.

Table 4.3. Relative difference in means between interference and target plus interference (dB) of stationary and moving targets using the 1D SWT with a velocity 2.6 m/s. Improvements over the unprocessed data are shown in bold.

Polarisation	HH	HV	VH	VV
Original data	10.4	10.4	10.4	10.4
$\tilde{A}_1$ (stationary target)	**10.9**	**11.3**	**11.3**	**10.7**
$\tilde{D}_1$ (stationary target)	0.0	0.0	0.0	0.0
$\tilde{A}_1$ (moving target)	1.6	1.8	1.8	1.6
$\tilde{D}_1$ (moving target)	**21.5**	**17.4**	**17.1**	**24.9**

Table 4.4. Relative difference in means between interference and target plus interference (dB) of stationary and moving targets using the 2D SWT with a velocity of 2.6 m/s. Improvements over the unprocessed data are shown in bold.

Polarisation	HH	HV	VH	VV
Original data	10.4	10.3	10.4	10.4
$\tilde{LL}_1$ (stationary target)	9.9	9.6	10.3	8.9
$\tilde{LH}_1$ (stationary target)	7.9	8.8	8.2	8.2
$\tilde{HL}_1$ (stationary target)	0	0	0	0
$\tilde{HH}_1$ (stationary target)	0	0	0	0
$\tilde{LL}_1$ (moving target)	1.3	1.8	1.4	1.0
$\tilde{LH}_1$ (moving target)	0.9	1.1	1.0	1.0
$\tilde{HL}_1$ (moving target)	**19.8**	**15.3**	**15.7**	**22.2**
$\tilde{HH}_1$ (moving target)	**17.8**	**14.5**	**13.7**	**21.6**

To determine the threshold multiplier, a common technique is to fit a model to the data and extrapolate to the desired P_{fa}. Based on the model fits in Figure 4.7 and 4.10, the K+Rayleigh distribution is used to compute the threshold multiplier [93]. For the detection results here, we have selected a P_{fa} of 10^{-5} which is possible only by extrapolating along the tail of the model. With the threshold multiplier determined prior to the CA-CFAR, the larger value of P ensures that the measured false alarm rate for the original data and each of the reconstructed sub-bands are very close to the desired P_{fa}.

Detection using 1D SWTs

Figure 4.14 shows the detection results for the HH polarisation before and after the 1D SWT detection scheme. The original detection results are shown in blue, while the results for the approximate and detail reconstructed sub-bands are shown in red and yellow, respectively. It can be observed that the stationary target (left) is best detected in the approximate reconstructed sub-band $\tilde{A}_1$ while there is a performance loss in the detail reconstructed sub-band, $\tilde{D}_1$. The performance however is reversed for the moving target (right), which is best detected in the $\tilde{D}_1$ reconstructed sub-band.

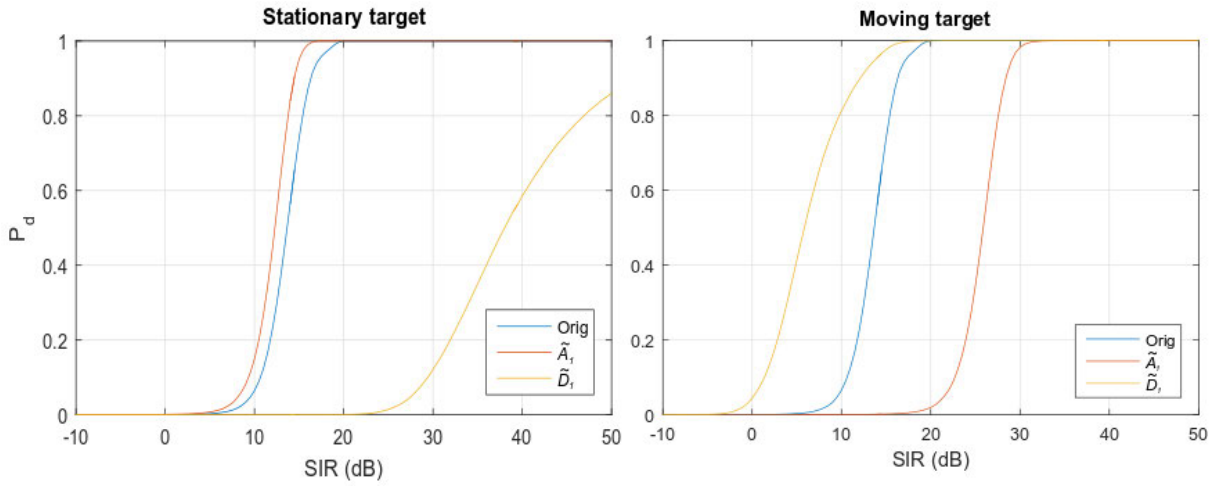

Figure 4.14. The probability of detection using the original and 1D reconstructed sub-bands of the HH polarisation for stationary and moving targets with a P_{fa} of 10^{-5}.

For further comparison, the required SIR to achieve a P_{d} of 0.5 is given in Table 4.5 for all polarisations. This choice is based on extensive literature which uses this level for comparison. For each target velocity, the required SIRs for each sub-band and the original data are recorded with the detection improvements highlighted in bold. Firstly, we can observe that the detection of a moving target in the $\tilde{D}_1$ detail reconstructed sub-bands show a significant improvement of 7.8 and 9.4 dB for HH and VV respectively, while the HV and VH polarisations have an improvement of 5.4 and 4.6 dB. The approximate reconstructed sub-bands show worse performance for the moving target case. Secondly, for the detection of a stationary target, the $\tilde{A}_1$ reconstructed sub-bands show an improvement of between 0.6 dB to 1.6 dB over the conventional detection scheme. The detail reconstructed sub-bands are worse for detection of the stationary target in this case.

Table 4.5. Required SIR for a $P_d = 0.5$ - stationary and moving targets. Improvements are shown in bold.

Polarisation	HH	HV	VH	VV
Original data	13.6	12.5	11.9	11.1
$\tilde{A}_1$ (stationary target)	**12.3**	**10.9**	**10.4**	**10.5**
$\tilde{D}_1$ (stationary target)	38.0	37.2	36.3	35.9
$\tilde{A}_1$ (moving target)	25.9	24.5	23.9	24.1
$\tilde{D}_1$ (moving target)	**5.8**	**7.1**	**7.3**	**1.7**

The detection using the Monte-Carlo simulation is able to quantify the detection improvement and confirm the detection analysis using mean separation described in Section 4.5.1. Both methods demonstrate the 2-channel filtering of the SWT, where the low frequency components are contained in the approximate sub-band, while the high frequency parts are contained in the reconstructed detail sub-band. When a target is not in the filtering bandwidth, the reconstructed sub-band will only contain interference broadly distributed over the frequency spectrum. This results in the target SIR in the reconstructed sub-band being stronger than the SIR of the unprocessed data. Thereby, the detection in the sub-band with the target gives a good detection improvement (i.e the $\tilde{A}_1$ reconstructed sub-band provides a better detection of the stationary target while the $\tilde{D}_1$ reconstructed sub-band gives a better detection of the moving target).

To further investigate the performance of moving targets, the target velocity is varied from 0 to 4.3 m/s. Figure 4.15 shows the detection results when measured at $P_d = 0.5$ for the original (unprocessed) data and the 1D SWT ($\tilde{A}_1$ and $\tilde{D}_1$) for the HH polarisation. The $\tilde{A}_1$ reconstructed sub-band has slightly better detection performance over the unprocessed data for stationary and slow moving targets, but decreases in performance as the target velocity reaches 1.5 m/s. Conversely, the $\tilde{D}_1$ reconstructed sub-band increases in performance when the target velocity is higher than approximately 2 m/s. The maximum improvement of 9.4 dB is achieved in $\tilde{D}_1$ for targets moving faster than 2.8 m/s in the VV polarisation. The figure also shows the transition velocity for the reconstructed sub-bands $\tilde{A}_1$ and $\tilde{D}_1$ which is approximately between 1.5 m/s and 2 m/s. This is the region where the target information is split between the sub-bands of the SWT. As a result, the detection performance in both reconstructed sub-bands is lower than the unprocessed data. In summary, the analysis of the 1D SWT shows that the approximate reconstructed sub-band $\tilde{A}_1$ can better detect stationary and slow moving targets while the detail reconstructed sub-band $\tilde{D}_1$ can be used for targets moving outside the endo-clutter region.

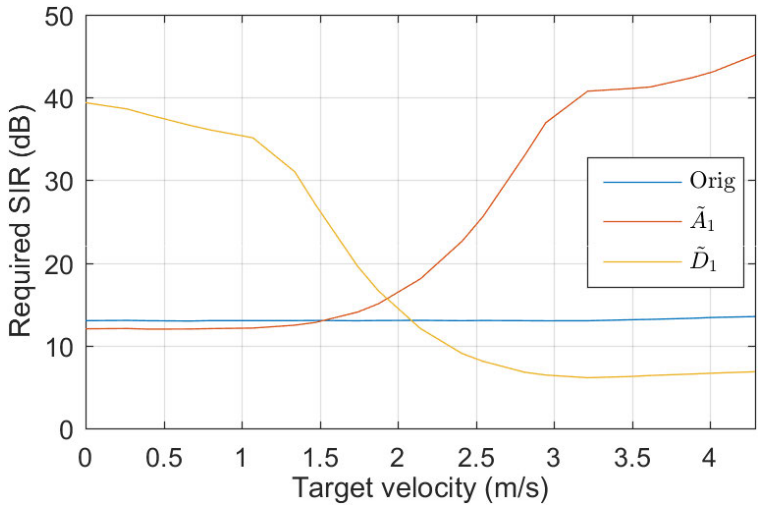

Figure 4.15. Required SIR for the HH polarisation measured at $P_d = 0.5$ using the 1D SWT detection scheme with the variation of the target velocity from 0 to 4.3 m/s.

Detection using 2D SWTs

The Monte-Carlo simulation is now repeated for the 2D SWT detection analysis. Figure 4.16 shows the P_d results of the stationary and moving targets with a radial velocity of 2.6 m/s for the HH polarisation. The required SIR to achieve a P_d of 0.5 is shown in Table 4.6 for the 4 polarisations. For the stationary target, the approximate reconstructed sub-band, $\tilde{LL}_1$ can detect a target about 1 dB better than the unprocessed data in all polarisations, except VV. The results are reversed for the moving target where significant improvement is now achieved in the reconstructed sub-bands, $\tilde{HL}$ and $\tilde{HH}$. The largest improvement over the unprocessed data is found in VV with 8.8 dB followed by the HH, HV and VH polarisations.

By varying the target velocity, the required SIR for a P_d of 0.5 is shown in Figure 4.17 for the HH polarisation. Similarly to the previous results, the $\tilde{LL}_1$ reconstructed sub-band has better detection performance for the stationary and slow moving target but then decreases as the target moves faster than 1.5 m/s. The horizontal $\tilde{LH}$ sub-band performs slightly worse than the unprocessed data. The diagonal $\tilde{HH}_1$ and vertical $\tilde{HL}$ reconstructed sub-bands, on the other hand, show a maximum improvement of approximately 4 and 8 dB, respectively for target velocities greater than 3 m/s. The target information is again split across sub-bands between approximately 1.5 m/s and 2 m/s and hence detection performance in this region is lower than the unprocessed data. There is also an unexpected peak at 1.3 m/s which highlights where sea-spikes are influencing the results. Note that this phenomenon does not greatly impact the other polarisations shown in Appendix A. From the detection analysis, the reconstructed $\tilde{LL}_1$

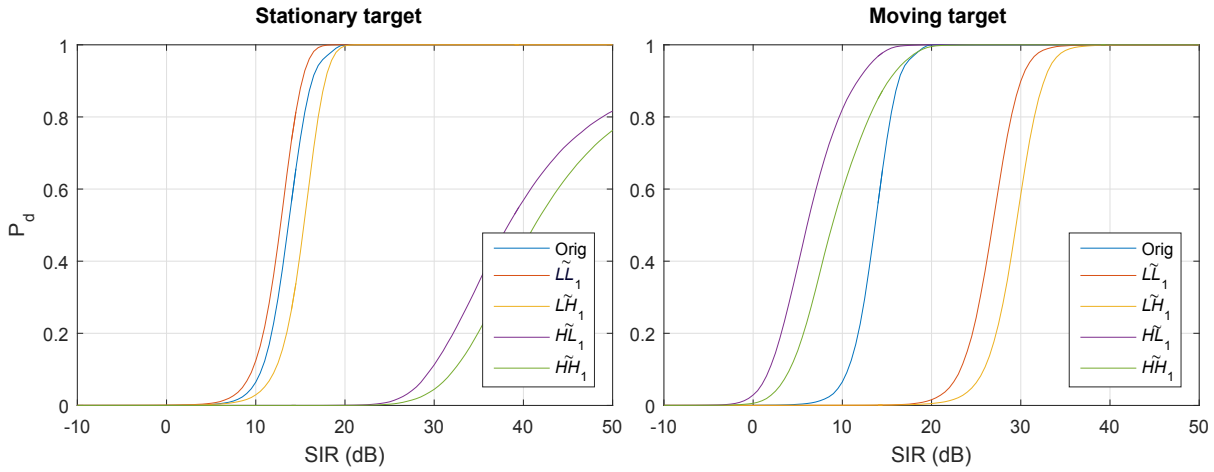

Figure 4.16. The probability of detection using the original and 2D SWT reconstructed sub-bands of the HH polarisation for stationary and moving targets with the P_{fa} of 10^{-5}.

sub-band would be selected for the detection of stationary and slow moving targets, with the $\tilde{HL}_1$ reconstructed sub-band for fast moving targets.

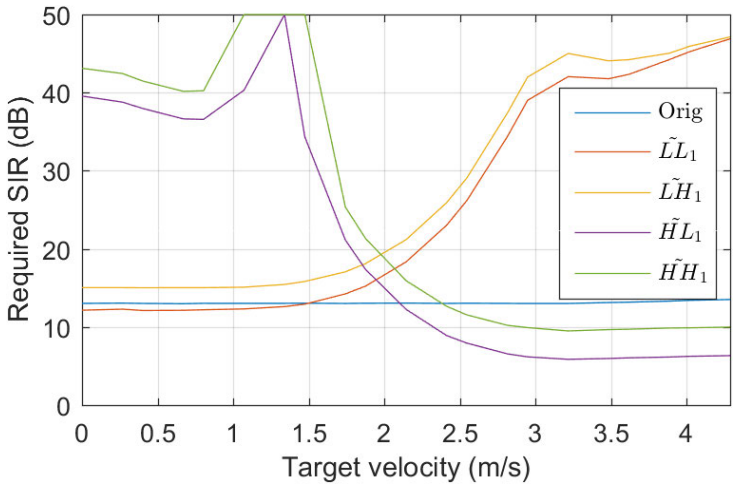

Figure 4.17. Required SIR for the HH polarisation measured at $P_{\text{d}} = 0.5$ using the 2D SWT detection scheme with the variation of the target velocity from 0 to 4.3 m/s.

Summary of 1D and 2D SWT Detection Results

The results from both the 1D and 2D SWT detection schemes demonstrate significant improvements over the original data. The $\tilde{D}_1$ and $\tilde{HL}_1$ reconstructed sub-bands are desirable for fast moving targets situated outside the endo-clutter region, while the $\tilde{A}_1$ and $\tilde{LL}_1$ reconstructed sub-bands are suitable for stationary and slow moving targets. Since the 1D

Table 4.6. Required SIR for a $P_d = 0.5$ - stationary and moving target. Improvements are shown in bold.

Polarisation	HH	HV	VH	VV
Original data	13.6	12.5	12.3	12.2
$\tilde{LL}_1$ (stationary target)	**12.8**	**12.1**	**11.4**	12.6
$\tilde{LH}_1$ (stationary target)	15.4	13.7	13.9	13.7
$\tilde{HL}_1$ (stationary target)	38.3	37.9	36.7	37.7
$\tilde{HH}_1$ (stationary target)	41.3	39.6	40.0	39.7
$\tilde{LL}_1$ (moving target)	26.8	26.0	25.3	26.5
$\tilde{LH}_1$ (moving target)	29.5	27.6	27.9	27.6
$\tilde{HL}_1$ (moving target)	**6.0**	**8.3**	**7.9**	**3.4**
$\tilde{HH}$ (moving target)	**8.9**	**9.8**	**11.0**	**5.2**

SWT offers slightly better detection performance over the 2D SWT for both stationary and moving target, the 1D SWT will be used for subsequent analysis.

4.6 Multi-Level SWT Decomposition

The multi-level decomposition of the SWT is achieved by further decomposing the approximate sub-band. The implementation of a multi-level (or higher level) decomposition using the 1D SWT is described in Sections 3.4.4 and 4.3. In computing the SWT, the total number of levels is a user-chosen parameter. In our case, the finite number of pulses places a practical ceiling on the highest level K in Equations (4.2) and (4.3). In the SWT decomposition, the wavelet filter impulse responses are up-sampled by 2 at every level of the decomposition. This causes rapid growth in the length of these filters as the level increases, eventually reaching the length of the data series. Further decomposition beyond this ceases to produce meaningful sub-bands. More precisely, if there are M samples in slow-time, and the length of the analysis filters (h_a, g_a) is N, then the maximum level K must satisfy

$$K \leq \log_2 \left(\frac{M}{N} \right). \tag{4.5}$$

For example, using length 8 Daubechies-4 filters with a CPI of 128 pulses implies the SWT is limited to 4 levels or lower. However, for our analysis in this chapter, we only use 3 levels to demonstrate the SWT performance. This simplifies the analysis and reduces the computational burden.

When performing the 3-level decomposition of the SWT, 3 detail and 1 approximate sub-bands are produced in the WT domain. The process of sub-band combination and reconstruction can then be applied to the data. For instance, we can combine the D_1 and D_2 sub-bands to produce a sub-band denoted by D_{12} which contains the information content of D_1 and D_2 sub-bands combined. For the initial analysis, the reconstructed sub-bands used are $\tilde{D}_1, \tilde{D}_2, \tilde{D}_3, \tilde{D}_{12}, \tilde{D}_{123}$, $\tilde{D}_{13}, \tilde{D}_{23}, \tilde{A}_1, \tilde{A}_2$ and $\tilde{A}_3$.

To investigate the performance of these reconstructed sub-bands, the mean separation of the data with and without an injected constant RCS target is computed. Figure 4.18 shows the mean separation for a number of reconstructed sub-band combinations using 3 different target radial velocities: 0, 1.1 and 2.6 m/s. These correspond to the centre, edge of the endo-clutter region and the exo-clutter (noise only) regions respectively. The mean separation of the original data is shown in blue and represents a reference level for the analysis. The results for the reconstructed sub-bands are then ranked and shown by a red line with triangles markers.

For the stationary target, the reconstructed sub-band $\tilde{A}_3$ has the biggest mean separation of 5 dB followed by $\tilde{A}_2$ and $\tilde{A}_1$. When the target has a radial velocity of 1.1 m/s, the reconstructed combination $\tilde{D}_{23}$ gives the best mean separation of 3 dB, implying that the target Doppler frequency is located between $\tilde{D}_2$ and $\tilde{D}_3$. For a target moving with a radial velocity of 2.6 m/s, the biggest mean separation is shown for the $\tilde{D}_1$ reconstructed sub-band and is 11 dB greater than the original mean separation. In this case, higher levels of the SWT do not improve the mean separation as there is little target information in the A_1 sub-band. Note also that the $\tilde{D}_2$ result is quite small, while the combination $\tilde{D}_{12}$ is greater than the original mean separation. This is due to the majority of information about the target being maintained in D_1.

After extensive experimentation, a group of reconstructed sub-bands have been selected for further analysis and to test the detection performance. A moving target outside the endo-clutter region will always be present in the $\tilde{D}_1$ reconstructed sub-band while a stationary target will always be located in the $\tilde{A}_1$ reconstructed sub-band. Detecting a slowly moving target is more difficult as it may be present in either the $\tilde{A}_2$ or $\tilde{D}_2$ reconstructed sub-bands or even have a Doppler frequency that lies partway between the frequency extent of these sub-bands. If this happens, it can potentially reduce the detection performance. Therefore to ensure good detection performance in all cases, we have included combinations of D_1, D_2 and D_3 sub-bands in our selected group. The frequency bandwidth of the final group of reconstructed sub-bands are shown in Figure 4.19 and include $\tilde{D}_1, \tilde{D}_2, \tilde{D}_{12}, \tilde{D}_{23}$ and $\tilde{A}_3$. Unfortunately, the target velocity is not known ahead of time and a method is required to select which sub-band to use to ensure good detection performance.

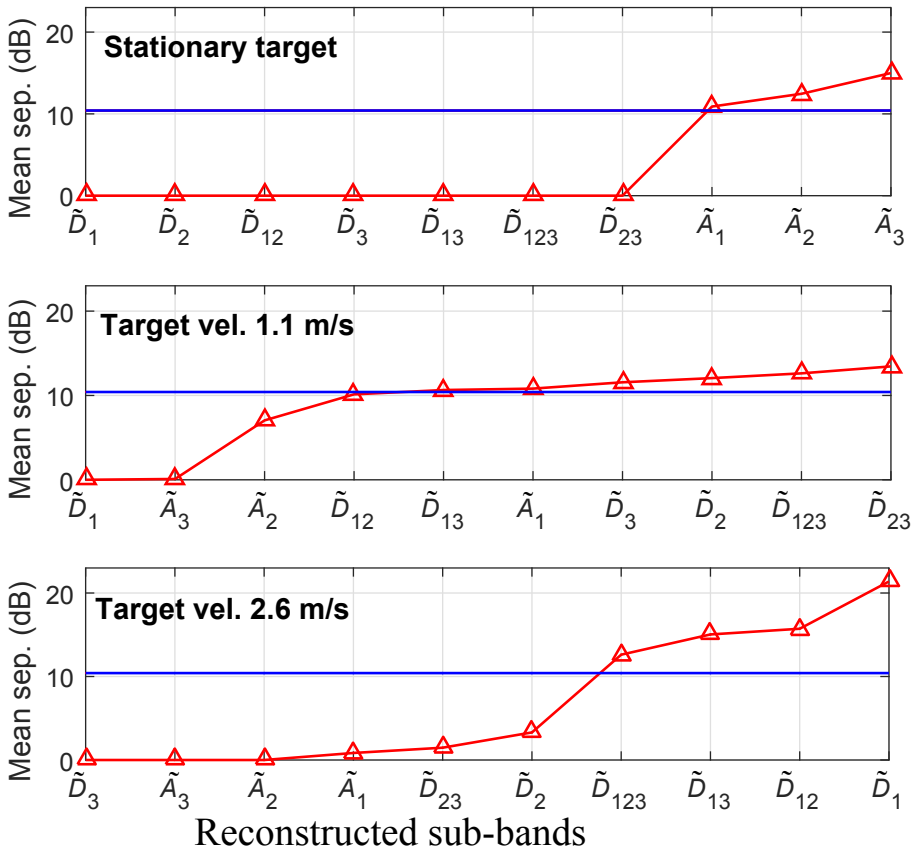

Figure 4.18. The mean separation for targets having an SIR of 10 dB after the SWT processing with sub-band reconstruction. The blue line is the original data mean separation and the red is for the reconstructed sub-bands.

4.7 Entropy Sub-band Indicator

4.7.1 Entropy Theory

Entropy is a measure of information and has been widely used to measure system disorder in statistical analysis [102]. It is also used to measure the global or average uncertainty of random samples [24, 50, 120] and has been applied to the problem of detecting targets in clutter. Jia and Kong [55] applied an entropy statistic to measure the range spread of a target in clutter. Using simulated data, the entropy detection statistic provided better performance at high SNR when compared to adaptive range cell integration and M/N detection [51]. Noting that large entropy values result in targets not being present, Wang et al. has applied entropy for target feature extraction [122]. The detection performance using entropy was observed to complement the

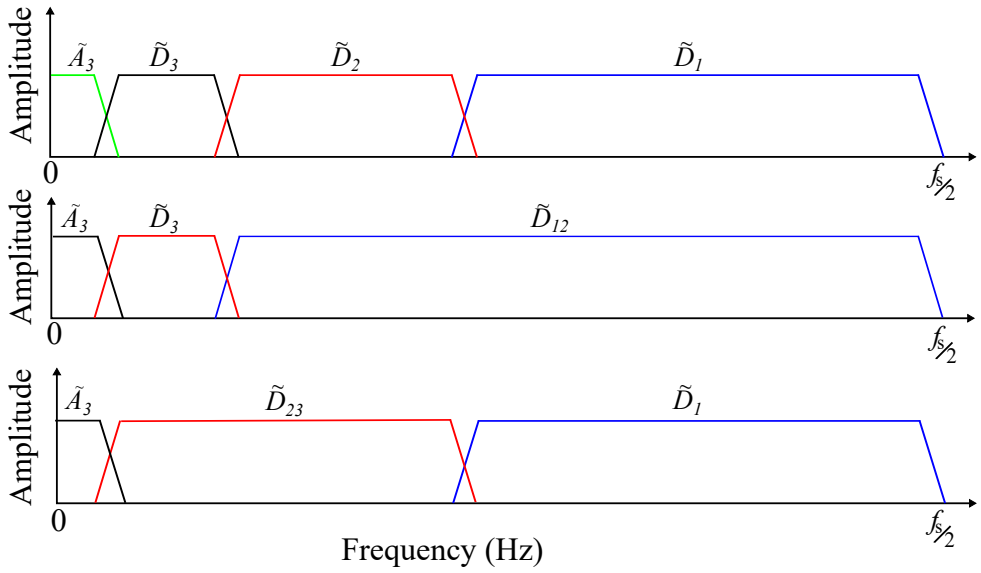

Figure 4.19. One sided frequency spectrum of the 3-level SWT reconstructed sub-bands. $f_s/2$ is the signal sampling rate. Top: the plot shows all the 3-level reconstructed sub-bands, middle: $\tilde{D}_{12}$ reconstructed sub-band is the combination of D_1 and D_2 sub-bands and bottom: $\tilde{D}_{23}$ is the combination of D_2 and D_3 sub-bands.

result using Bayesian detection (i.e. good performance with Bayesian detection resulted in poor performance with entropy detection and vice versa). Therefore a detection scheme was proposed using both methods in parallel which produced good overall detection performance. Guo et al. [49] also employed entropy to measure the randomness after non-coherent integration. Applied to a simulated dataset, the method demonstrated high probability of detection, but also produced a high level of false alarms.

For our study, entropy is proposed as a means of determining which reconstructed sub-bands contain the most information about a target and hence would provide the best detection performance. The motivation for using entropy is that the target is persistent over time while the interference returns are more random. The entropy will therefore be different when a target is present.

The entropy of a discrete random variable, X, is given by

$$H(X) = -\sum_{q=1}^{Q_E} \int_{l_q}^{u_q} g(x_q) \log g(x_q)\, dx_q \tag{4.6}$$

where $g(x_q)$ is the PDF of the data over Q_E intervals and the lower and upper limits are l_q and u_q respectively [120]. Let $w_q = u_q - l_q$ be the width of the histogram bin for the q^{th} term in

the summation. The bin probabilities can then be written as $p_q = w_q g(x_q)$, giving the final expression for the entropy,

$$H(X) = -\sum_{q=1}^{Q_E} p_q \log(p_q/w_q), \quad w_q > 0. \tag{4.7}$$

4.7.2 Entropy Application

To apply the entropy given in Equation (4.7), the PDF of the data is firstly determined for each range bin using all the slow-time samples in a given CPI. A smaller entropy value is observed when the distribution has a smaller variance and vice versa. This means that the entropy value of targets, depending on their distributions, can be smaller or larger than the entropy value of the interference. To avoid the variation, we define our entropy indicator as the absolute value of the entropy with zero mean,

$$E_b(r) = |H(r) - \langle H \rangle|, \tag{4.8}$$

where $\langle H \rangle$ is the mean entropy over all range bins. Taking the absolute value of the difference in equation (4.8) ensures that the entropy values of the reconstructed sub-band b are always positive.

To demonstrate the entropy variation when a target is present, a constant RCS target is injected into the data with an SIR of 10 dB. A CPI of 128 pulses and 200 range bins are used for the experiment. Figure 4.20 shows the entropy variation for each range bin using a single level SWT. When the target is stationary (top plot), the reconstructed sub-band $\tilde{A}_1$ produces a peak at the target location while the entropy variations in $\tilde{D}_1$ sub-band are small across all range bins. However, when the target moves at a radial velocity of 2.6 m/s (bottom plot), $\tilde{D}_1$ shows a high peak at the target bin and $\tilde{A}_1$ shows little variation. These results are consistent with the mean separation observed in Section 4.6.

Let γ_b be the *maximum entropy* variation (peak value) for the reconstructed sub-band, b, defined by

$$\gamma_b = \max_r \{E_b(r)\}. \tag{4.9}$$

The γ_b values are used as an entropy metric to determine the presence of a target. Figure 4.21 shows the entropy metric for a number of reconstructed sub-bands as the SIR increases. Three different target velocities (0, 1.1 and 2.6 m/s) are shown with each result baselined by first determining the entropy indicator from Equation (4.8) over an interference only region and

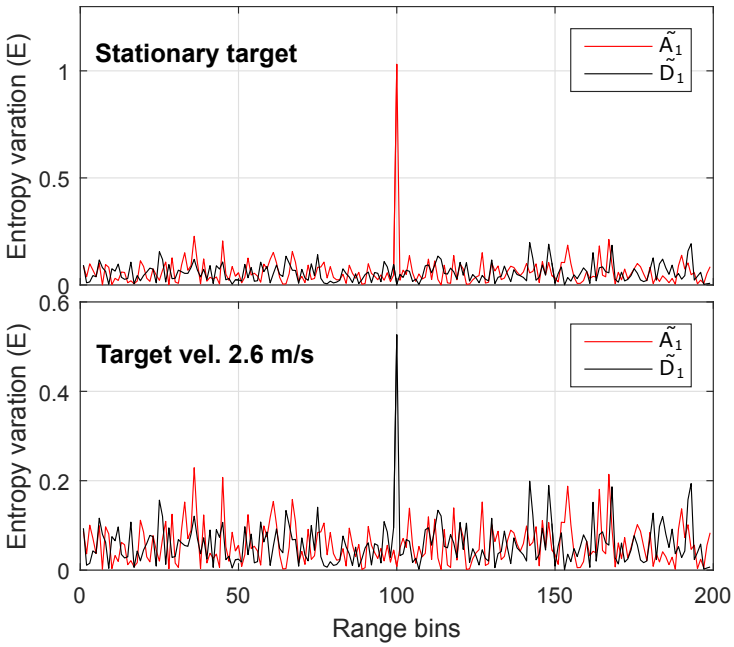

Figure 4.20. Entropy variation of the data with an injected target having an SIR of 10 dB at range bin 100: stationary target (top) and moving target with radial velocity 2.6 m/s (bottom).

then offsetting the measured entropy value. This ensures that the entropy value for each reconstructed sub-band has a similar level when no target is present. Note that when there is no target present, the entropy difference is 0.

When the target is stationary, the maximum entropy $\gamma_{\tilde{A}_3}$ of the $\tilde{A}_3$ reconstructed sub-band has the highest value followed by $\gamma_{\tilde{A}_2}$ and $\gamma_{\tilde{A}_1}$. For the faster moving target at 2.6 m/s, the entropy metric is maximum for the $\tilde{D}_1$ reconstructed sub-band. Lastly, when the target moves at 1.1 m/s, the combination $\tilde{D}_{23}$ reconstructed sub-band is best. Again, these results consistently match the mean separation found in Section 4.6. A similar result is achieved when the Swerling-1 fluctuating target is used as shown in Figure 4.22.

4.7.3 Sub-band Indication Scheme

One possible method to perform our sub-band indication is to decompose, isolate and reconstruct all the sub-bands and then determine the maximum entropy, γ, for each reconstructed sub-band. Then the reconstructed sub-band with the biggest γ value is selected for the detection as illustrated in the previous section. However, this method requires unnecessary computation as some sub-bands may not be required for the final detection.

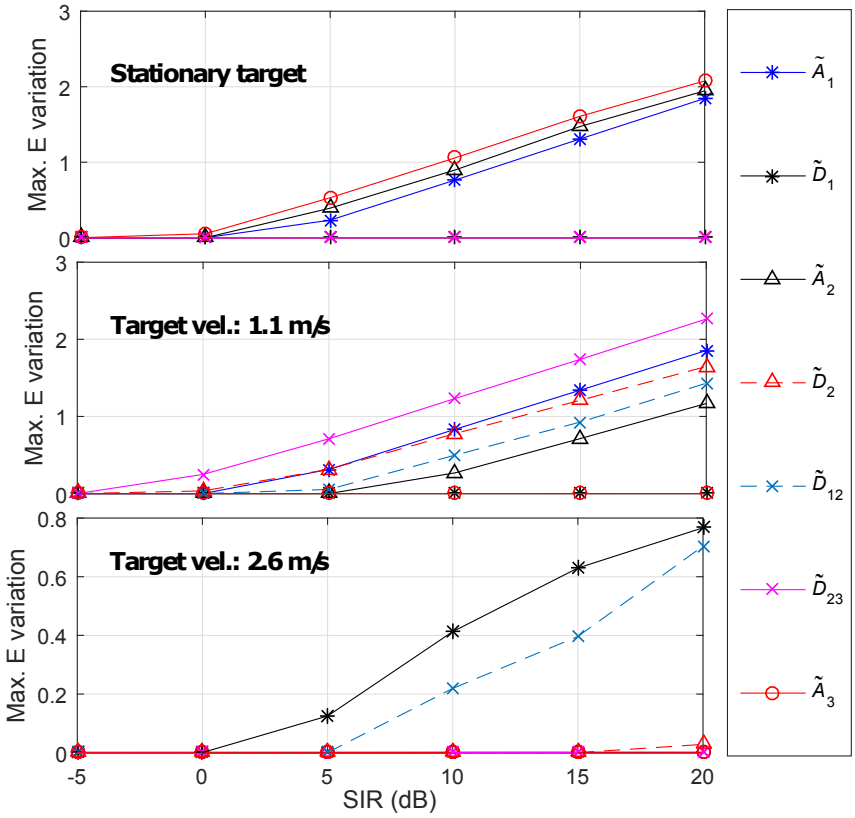

Figure 4.21. Maximum entropy variation with a Swerling-0 target as a function of SIR. For a stationary target, the $\tilde{A}_3$ sub-band has the biggest maximum entropy. For a moving target, the biggest entropy variation is seen in one of the detail sub-bands. For very weak and no target case, the maximum entropy or entropy difference is zero.

A more efficient method is to compare the entropy variation of the sub-bands after each decomposition level. This idea is based on an image processing application for selecting the minimum decomposition level of a natural image [129]. Figure 4.23 shows the sub-band selection scheme for our detector where the maximum entropy of the reconstructed sub-band for each level of decomposition is compared. The first step is to compute the $\tilde{A}_1$ and $\tilde{D}_1$ reconstructed sub-bands after a single level of decomposition and then determine $\gamma_{\tilde{A}_1}$ and $\gamma_{\tilde{D}_1}$. If $\gamma_{\tilde{D}_1}$ is greater than $\gamma_{\tilde{A}_1}$, we select $\tilde{D}_1$ to perform the detection because the target is no longer maintained in $\tilde{A}_1$. However, if the maximum entropy of $\tilde{D}_1$ is less than $\tilde{A}_1$, we compute the next level SWT and compare the maximum entropy of $\tilde{D}_2$ and $\tilde{A}_2$. This time, if $\tilde{D}_2$ is larger than $\tilde{A}_2$, we select the maximum of the three reconstructed sub-bands: $\tilde{D}_2, \tilde{D}_{12}$ and $\tilde{D}_{23}$. If $\tilde{A}_2$ has the larger entropy, then a further decomposition to $\tilde{A}_3$ is performed. For most cases, this method reduces the computation cost by avoiding the decomposition and reconstruction of sub-bands which are not necessary.

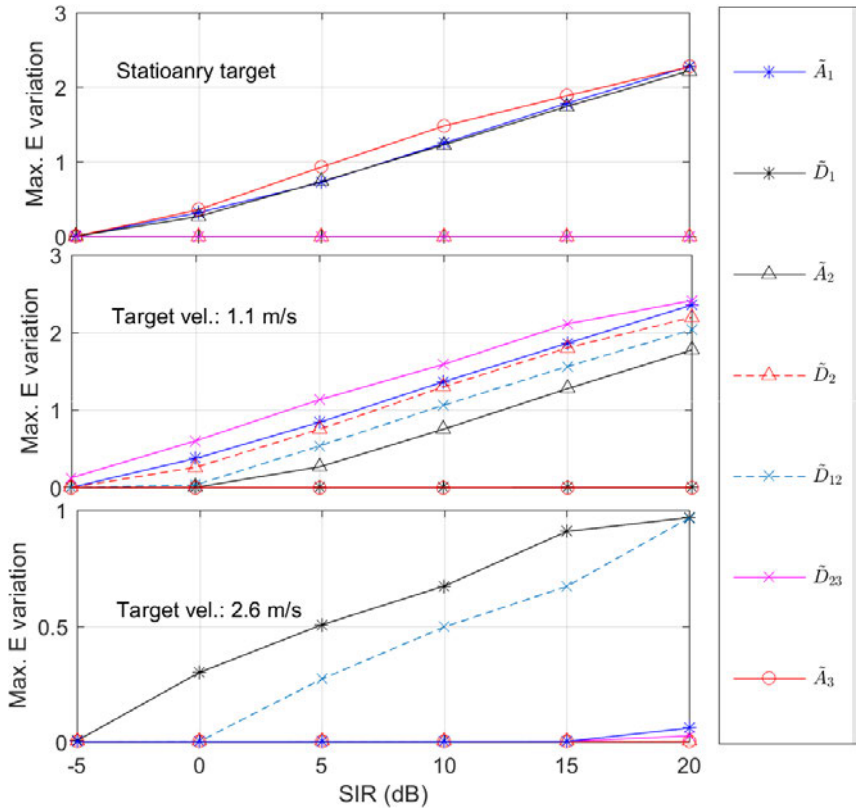

Figure 4.22. Maximum entropy variation with a Swerling-1 target as a function of SIR. For a stationary target, the $\tilde{A}_3$ sub-band has the biggest maximum entropy. For a moving target, the biggest entropy variation is seen in one of the detail sub-bands. For very weak and no target case, the maximum entropy or entropy difference is zero.

4.8 Detection Performance Using 1D SWTs

To investigate the detection performance of the new detection scheme, the Monte-Carlo simulation from Section 4.5.2 is repeated here. Variations of both the target fluctuation (Swerling-0 and 1) and the target radial velocity (0, 1.1 and 2.6 m/s) are given with each result also showing the proportion of selected reconstructed sub-bands. The data used for comparison comprises a CPI of 128 pulses, 200 range bins and both HH and VV polarisations. Note that we are not comparing any coherent detection techniques due to the time and range varying Doppler spectrum which makes such analysis complicated.

The parameters for the CA-CFAR algorithm are given in Section 4.5.2 with each reconstructed sub-band requiring a different threshold multiplier. This is also computed by fitting a model to the data and extrapolating to the desired P_{fa}. Figure 4.24 illustrates that the K+Rayleigh model fits both the data and each reconstructed sub-band well. For this experiment, the

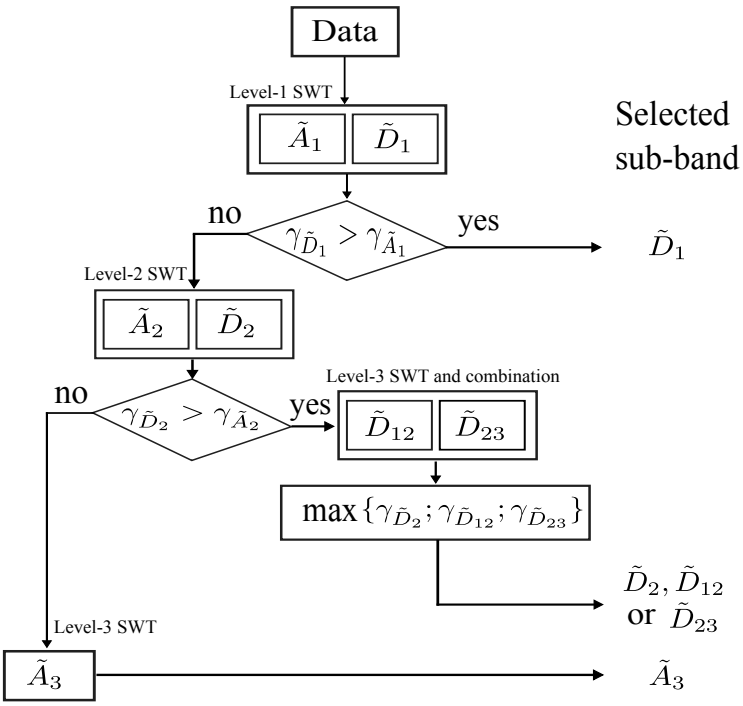

Figure 4.23. Entropy sub-band indication scheme: the entropy of each level sub-band reconstruction are compared. γ is the maximum entropy of each sub-band used to indicate the sub-band with the most information about the target.

complimentary cumulative distribution function (CCDF) of the K+Rayleigh distribution is also shown in Figure 4.25. Interestingly, the longer distribution tails due to the sea-spikes are mostly confined to the first level detail sub-bands. For this implementation, the desired P_{fa} is arbitrarily set to 10^{-3} for both filtered and unfiltered data. This choice allows for the actual P_{fa} to be measured without resorting to extrapolation of the CCDF model. The CNR and shape parameter for this example are 17.8 dB and 0.7 respectively. The CNR$_r$ and shape parameters for the reconstructed sub-bands are given in Table 4.7.

Three alternative detection cases are now compared. The first uses the unfiltered 'original' data as an input into the CA-CFAR algorithm. The second result uses the 'best' SWT reconstructed sub-band as determined by the mean separation analysis in Section 4.6. These comprise $\tilde{A}_3$, $\tilde{D}_{23}$ and $\tilde{D}_1$ for targets with radial velocities of 0, 1.1 and 2.6 m/s, respectively. The third case uses the entropy sub-band indicator to determine the 'best' reconstructed sub-band. Ideally, the performance of this scheme should match the best SWT results from the known sub-band in the second case.

Table 4.7. Shape parameter estimate for the reconstructed sub-bands used to determined the threshold in the detection analysis.

Polarisation	HH				
Reconstructed Sub-band	$\tilde{D}_1$	$\tilde{D}_2$	$\tilde{D}_{12}$	$\tilde{D}_{23}$	$\tilde{A}_3$
CNR_r (dB)	18.6	14.5	16.4	17.4	1.4
Shape	0.04	0.03	0.04	0.05	0.1

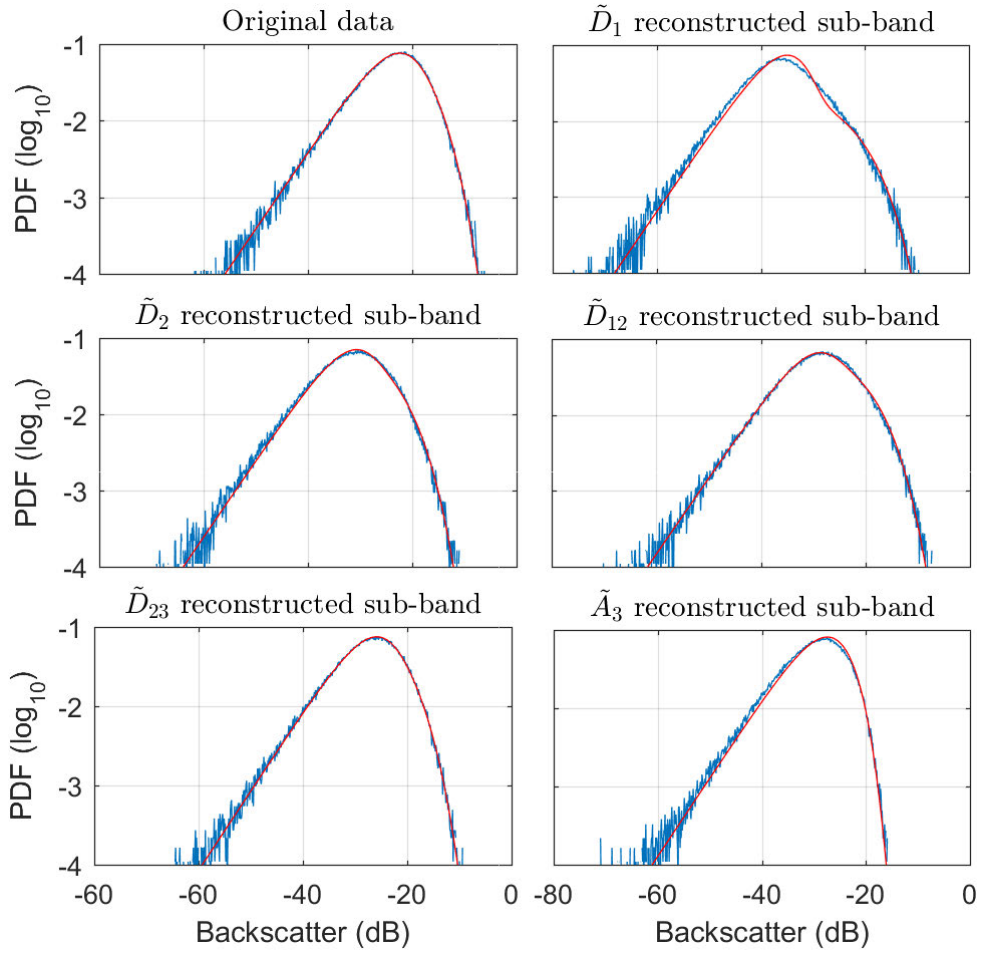

Figure 4.24. Sea clutter PDFs of the selected reconstructed sub-bands: data (blue) and K+Rayleigh distribution (red).

4.8.1 HH Polarisation

The first data set used for the detection investigation is the HH polarisation. Figure 4.26 shows the detection performance (first column) and reconstructed sub-band selections (second column) for a Swerling-0 target using the three different target velocities. The unfiltered data

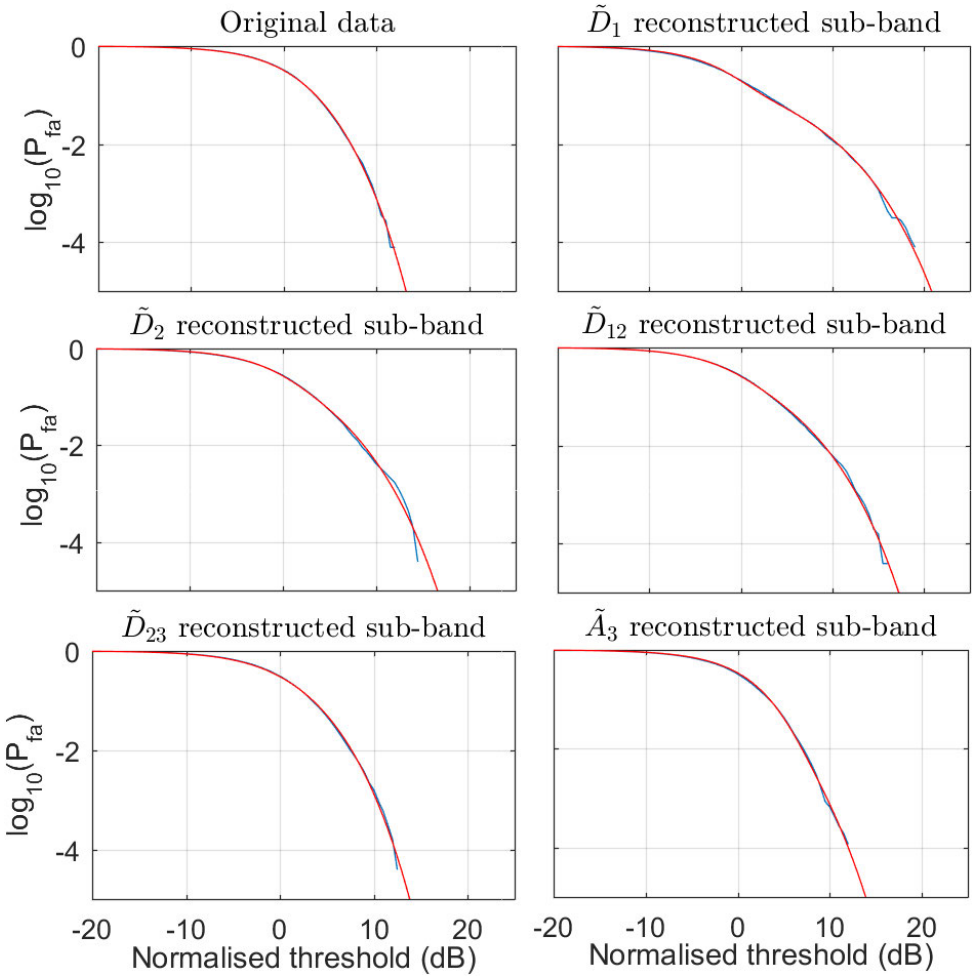

Figure 4.25. CCDF of the selected reconstructed sub-bands: data (blue) and K+Rayleigh distribution (red).

detection result is shown in blue while the best reconstructed sub-band detection results are shown in red, magenta and black for the three target velocities. The detection result using the entropy indicator is plotted in dark green and denoted as 'eSWT'. For all the comparisons in this section, the SIR has been compared at $P_{\mathrm{d}} = 0.5$.

For the stationary target, the detection in the $\tilde{A}_3$ reconstructed sub-band has the highest detection performance and is approximately 6 dB higher than the original result. The eSWT performance is not as good because the majority of the indicator results are incorrect when the SIR is below 5 dB. However it still has a 5 dB improvement over the original result. For the slow moving target, the $\tilde{D}_{23}$ performance is 3 dB above the original, while the eSWT has an improvement of only 2.5 dB. This is because the indicator is often confused between the $\tilde{D}_2$ and $\tilde{D}_{23}$ reconstructed sub-bands as shown in Figure 4.26 (right column, middle). However, since both of these contain information about the target, there is only a minor impact on the

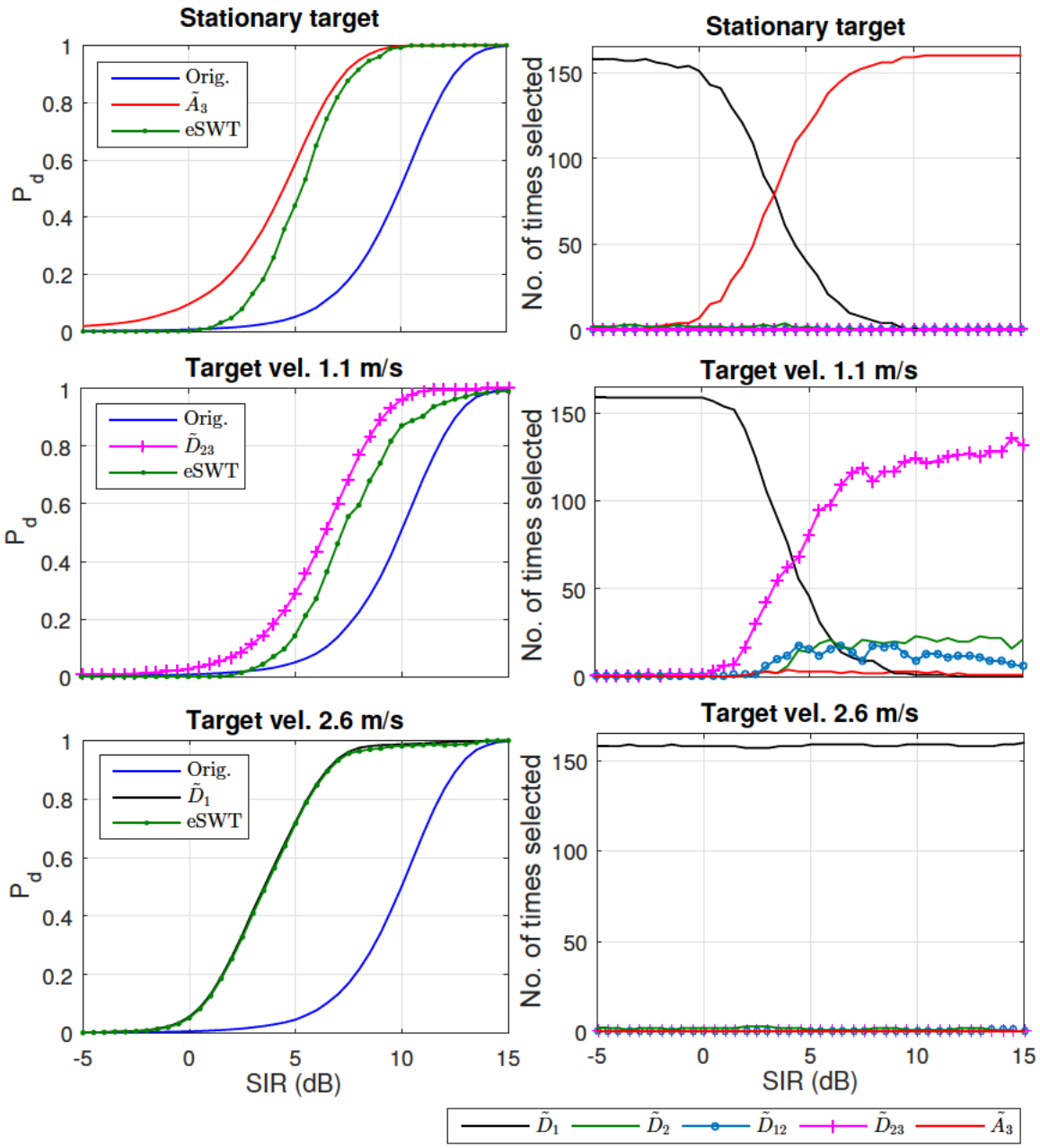

Figure 4.26. The probability of detection using a Swerling-0 target (first column) for the HH polarisation. The second column shows the number of times the reconstructed sub-bands are selected for detection when the entropy sub-band indicator is used.

final detection result. For the faster moving target, the eSWT algorithm correctly selects $\tilde{D}_1$ almost 100% of the cases and the detection improvement is about 7 dB over the unfiltered data.

Figure 4.27 illustrates the detection performance with a Swerling-1 target. Due to the larger fluctuation in the target RCS, the detection algorithm now requires a slightly higher SIR to

achieve the same P_d value as a Swerling-0 target. However, the detection improvements are almost identical to the Swerling-0 target.

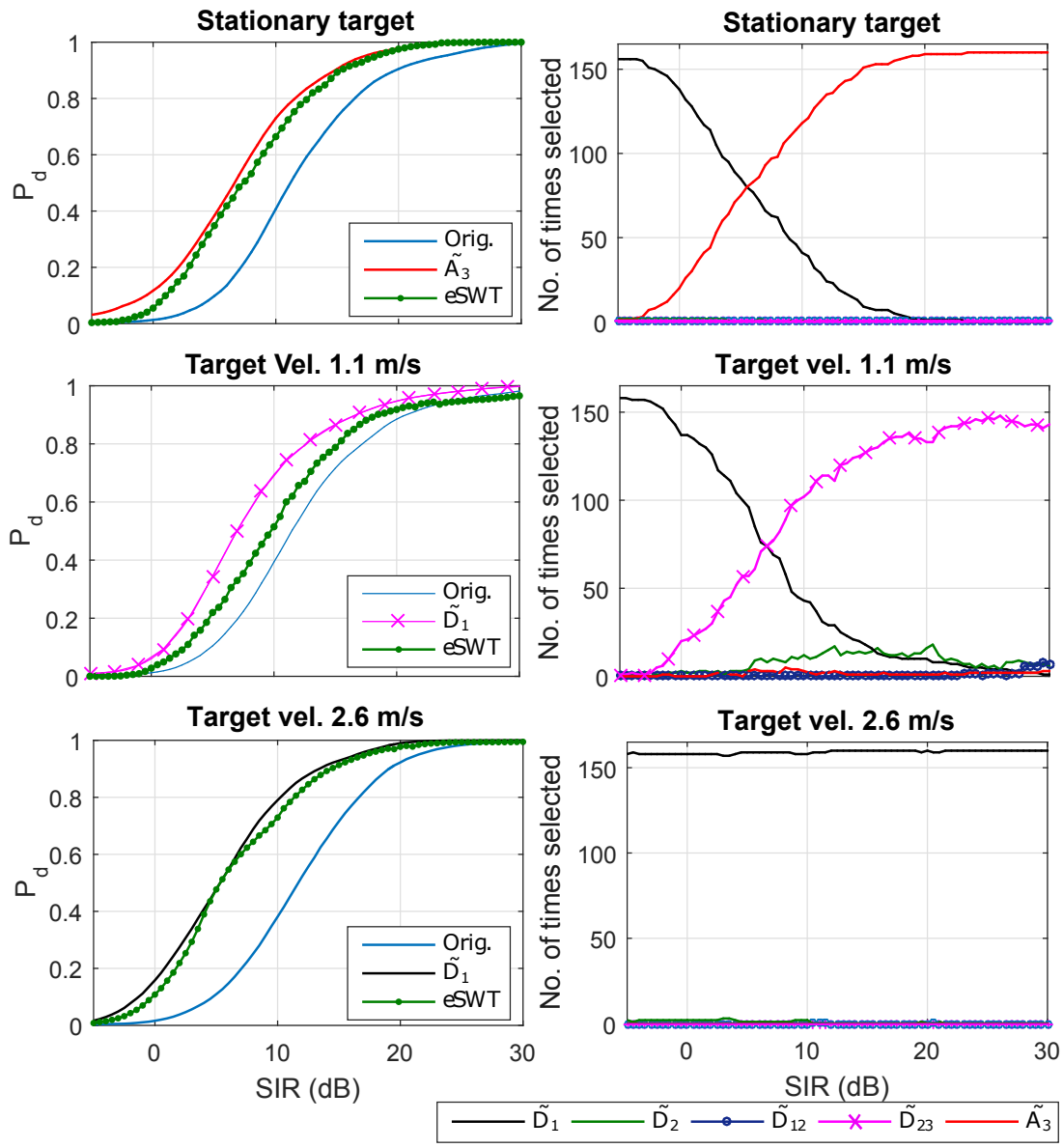

Figure 4.27. The probability of detection using a Swerling-1 target (first column) for the HH polarisation.The second column shows the number of times the reconstructed sub-bands are selected for detection when the entropy sub-band indicator is used.

4.8.2 VV Polarisation

To further investigate the detection performance, the scheme is applied to data from the VV polarisation. Figure 4.28 shows the detection performance (left column) and the number of

selected sub-bands (right column) for a Swerling-0 target. For the stationary target, there is an improvement of about 4 dB over the unprocessed data when a known reconstructed sub-band, $\tilde{A}_3$ is used. For an unknown target velocity (marked eSWT), the entropy sub-band indicator only selects the correct sub-band when the target SIR is greater than 2.5 dB with an improvement of approximately 3.5 dB. For the target moving at 1.1 m/s, the best detection result is the $\tilde{D}_{23}$ reconstructed sub-band with an improvement of about 3 dB. The eSWT improvement in this case is about 2.5 dB. When the target moves at a relative velocity of 2.6 m/s, a significant improvement of approximately 8 dB is achieved. The detection performance of a Swerling-1 target is then shown in Figure 4.29 and is very similar to the Swerling-0 results.

Overall, the proposed SWT detection works well for both HH and VV polarisations and for both Swerling-0 and Swerling-1 targets. The detection in VV offers a slightly better performance compared to the HH polarisation for moving targets but slightly less for stationary targets. The detection results reflect the differences in the sea-clutter for both polarisations. Moreover, the sub-band indicator selects the optimal reconstructed sub-band in the majority of cases.

To demonstrate the variation of the detection performance with different target velocities, the required SIR to achieve a $P_{\mathrm{d}} = 0.5$ is measured using Monte-Carlo simulation. Figure 4.30 shows the result for the HH polarisation where the blue line is the required SIR for the original unprocessed data and the red line with circles shows the result using the SWT with the entropy sub-band indicator. Overall, the eSWT required less SIR to produce the same P_{d} as the original detection with a few velocities having higher SIR. These peaks correspond to the transitions of sub-bands corresponding to PRF/4 (2.1 m/s) and PRF/16 (0.53 m/s) and highlight where the target indicator has selected the wrong sub-bands.

4.9 Conclusion

This chapter reported on the application of SWTs to target detection in sea-clutter. The process of *sub-band isolation and reconstruction* has been proposed to highlight different features of the sea-clutter and improve target detection. The first part of this chapter described how to use both 1D and 2D SWTs to analyse sea-clutter. This revealed that by isolating some sub-bands, the reconstructed sub-bands of the SWT contain less spiky sea-clutter than others. We also investigated and compared the detection performance of both 1D and 2D SWTs against unprocessed data using two methods and found that depending on the target velocity, some sub-bands of the 1D and 2D SWT offered a larger mean separation and better detection compared

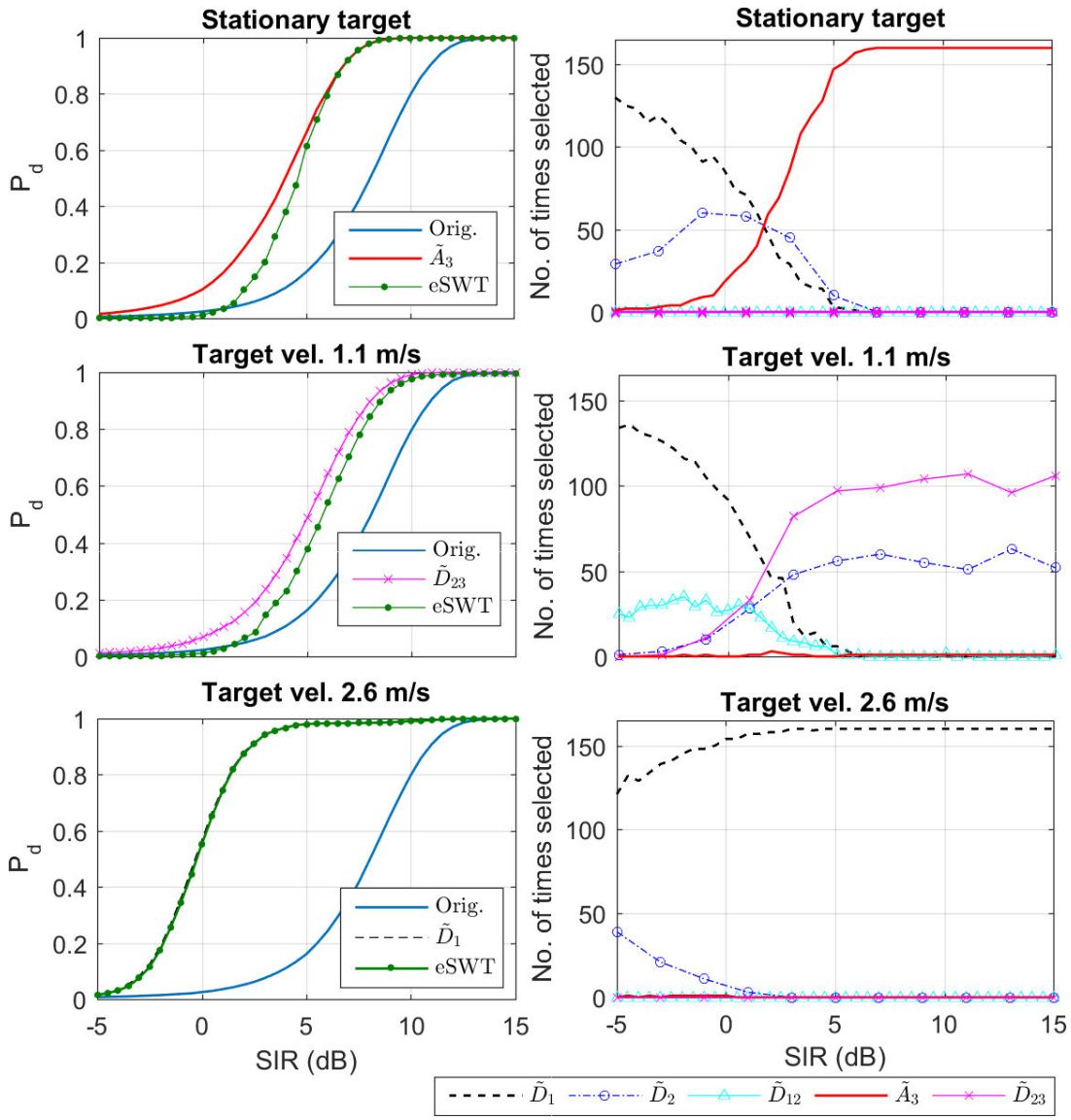

Figure 4.28. The probability of detection for Swerling-0 target (first column) for the VV polarisation and the number of times the reconstructed sub-bands are selected for detection (second column).

to the unprocessed data. It is also found that the detection using the 1D SWT outperforms the 2D SWT in all target cases.

The second part of the chapter investigated multi-level decomposition and sub-band reconstruction using the 1D SWT to further improve the detection performance. To demonstrate the performance of different sub-bands, the mean separation between the interference and target plus interference was studied for different reconstructed sub-band

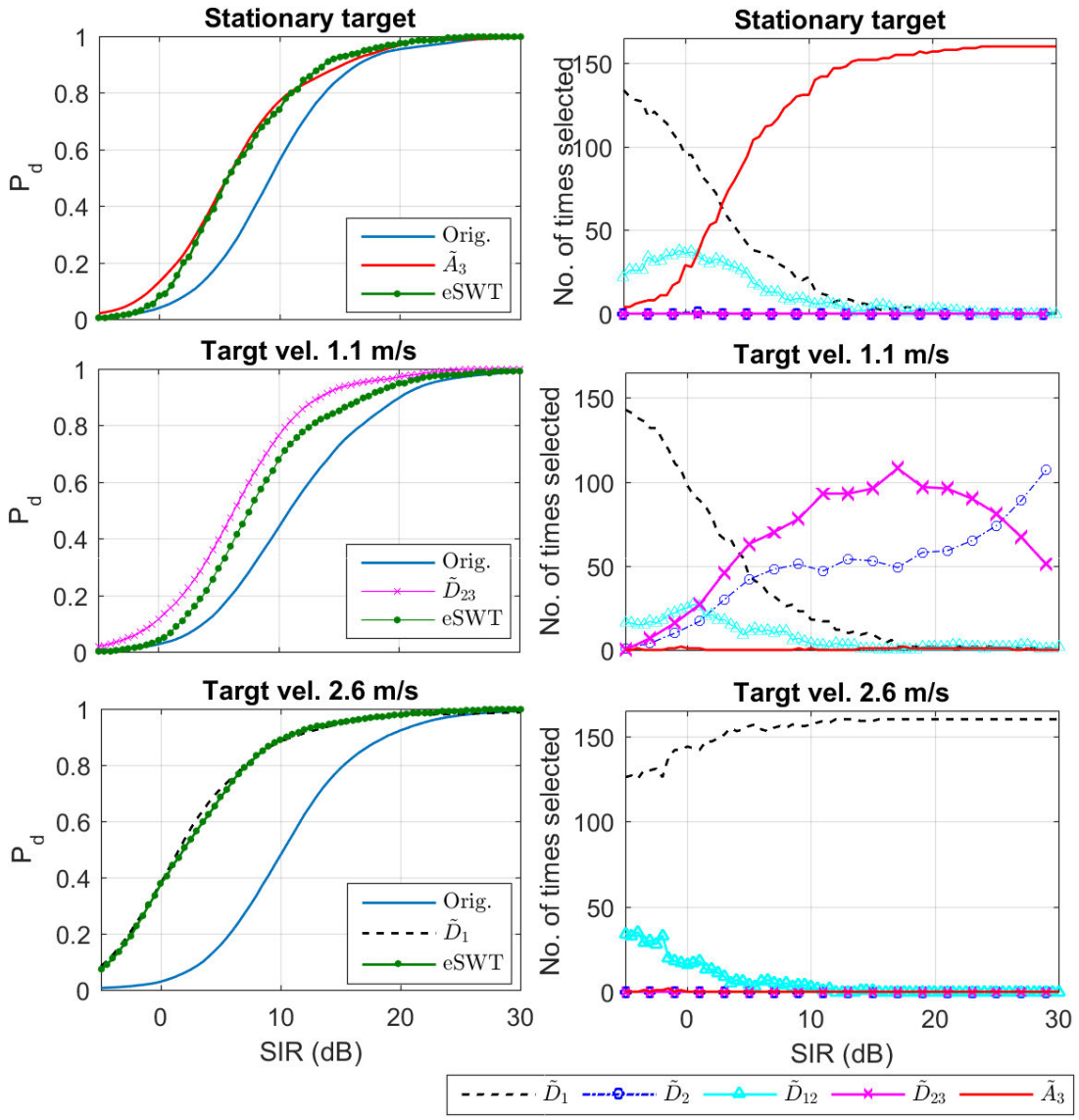

Figure 4.29. The probability of detection for Swerling-1 target (first column) for the VV polarisation and the number of times which the reconstructed sub-bands are selected for detection (second column).

combinations. This revealed that the stationary target was better detected in the approximate sub-band at a higher level decomposition, while a moving target was better detected in one of the detail reconstructed sub-bands.

Selecting the correct sub-band is key for implementing a practical detection scheme when the target's radial velocity is unknown. Entropy was proposed as a means of indicating which reconstructed sub-band contains the most information about the target. A computationally

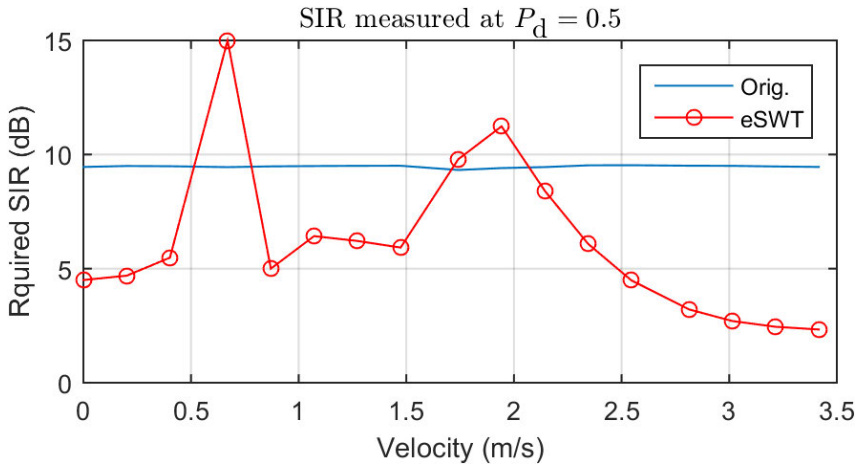

Figure 4.30. Required SIR for the HH polarisation measured at P_d = 0.5 using the 1D SWT detection scheme with variation of the target velocity from 0 to 3.4 m/s.

efficient scheme was presented based on the maximum entropy at different levels of the SWT decomposition.

The last part of the chapter used a Monte-Carlo simulation to quantify and compare the detection improvement against unprocessed data. This analysis revealed that with prior knowledge of the target's velocity, the improvement in the required SIR when measured at $P_d = 0.5$ was between 3 and 7 dB for the HH polarisation and between 2.5 and 8 dB for VV when compared to unfiltered data. The improvement also varies with the target radial velocity. For the unknown target velocity case, the entropy indication scheme was able to successfully determine the 'best' reconstructed sub-band in the majority of cases and had a similar improvement to the known target velocity case.

Chapter 5

Target Detection in Bistatic Radar Sea Clutter Using Stationary Wavelet Transforms

IN this chapter, the stationary wavelet transform (SWT) detection scheme is tested with both monostatic and bistatic data from the netted radar (NetRAD) multistatic radar system. The detection performance is determined with a Monte-Carlo simulation and a cell averaging constant false alarm rate detector. The results then confirm the robustness of the SWT detection scheme across different data sets.

5.1 Introduction

Multistatic radar systems provide additional degrees of freedom which can potentially improve our understanding of the environment and improve target detection in spiky sea clutter. Other benefits include a possible counter to stealthy targets and the potential for utilising passive receive nodes. The netted radar (NetRAD) multistatic radar system was jointly developed by the University College London in the UK and the University of Cape Town in South Africa [4]. Since the NetRAD system trials in 2010, researchers have extensively analysed the NetRAD data to gain a better understanding of the clutter behaviour [6, 45, 86] and develop multistatic coherent detection techniques [78]. This analysis showed that the bistatic mean reflectivity and amplitude statistics vary with the bistatic angle, typically having a lower mean backscatter and being less spiky than the monostatic data [6, 45].

Another potentially useful approach to improve target detection performance is to apply signal processing methods prior to detection. Existing examples include coherent processing [16, 30, 88, 124], time-frequency processing, [9, 37, 39, 53, 133] and space-time adaptive processing [83]. In Chapter 4, a novel detection technique using stationary wavelet transforms (SWT) was presented and applied to sea-clutter collected from an airborne platform [37]. In this chapter, the technique is applied to both monostatic and bistatic sea-clutter, collected from a cliff top by the NetRAD radar system. The robustness of this technique using both monostatic and bistatic data is demonstrated.

This chapter is organised as follows. Section 5.2 gives a description of the NetRAD system, trial and data sets. The background on SWTs and the detection scheme is briefly described in Section 5.3. Section 5.4 then illustrates and quantifies the detection performance. The conclusions are given in Section 5.5.

5.2 NetRAD Data

5.2.1 NetRAD System and Trial

NetRAD is a ground-based pulsed-Doppler coherent multistatic radar system consisting of three identical nodes [4]. For the sea-clutter collections, the radar operated in a bistatic configuration with two nodes triggered using GPS disciplined oscillators and synchronised through a 5 GHz wireless link [96]. The radar independently recorded both horizontal and vertical polarisations with a centre frequency of 2.4 GHz, a 45 MHz bandwidth, 1 kHz pulse repetition frequency (PRF) and a peak power of 400 W.

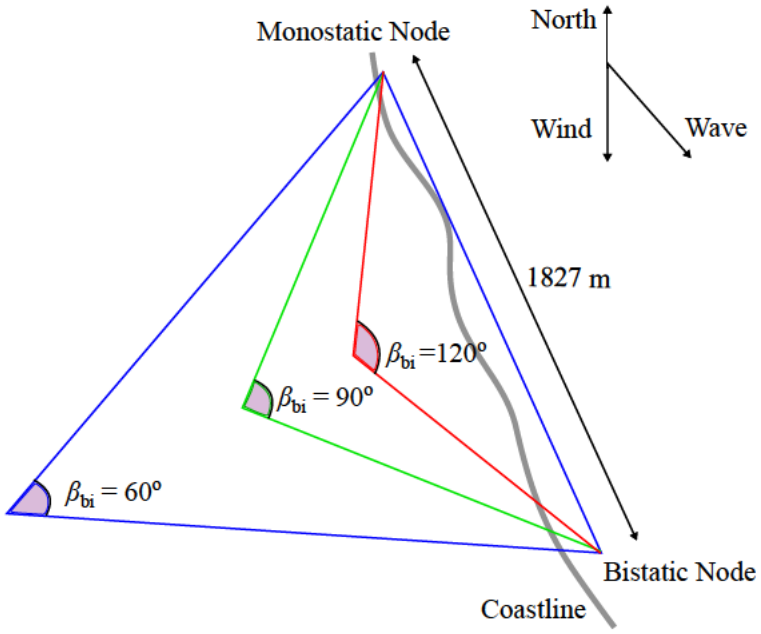

Figure 5.1. Illustration of NetRAD trial for three bistatic angles: 60°, 90° and 120° [5].

The data was recorded during a series of trials in October 2010 on the coast of South Africa near the Cape Point area [4]. The setup of the trial is shown in Figure 5.1 with one node transmitting and two receiving. Data was collected for three bistatic angles, β_{bi} of 60°, 90° and 120° with a baseline that ran Northwest to Southeast and a separation between the two nodes of 1827 m. The wind direction was from the North with a speed that increased during the trials from 10.2 m/s to 12.3 m/s, while the wave height varied between 3.28 m to 4.2 m. This corresponds to a Douglas sea state 5. Both nodes were looking cross-wind with the waves travelling towards the receiver of the bistatic node. For more detail, see Section 2.5.2.

5.2.2 NetRAD Data Analysis

Understanding the characteristics of the NetRAD sea-clutter is important to ensure the SWT scheme uses the correct wavelet decomposition level for the data. Figures 5.2 and 5.3 show examples of the horizontally polarised monostatic and bistatic data recorded at the 'bistatic' look angle of 60° with the time domain on top, the normalised Doppler spectrum or power spectral density (PSD) in the middle and the average PSD on the bottom. The data consists of strong returns that vary greatly from range bin to range bin. Some of these last for short periods of time while others persist over the whole observation time. These 'sea-spikes' are the result of breaking waves and can easily be confused with targets.

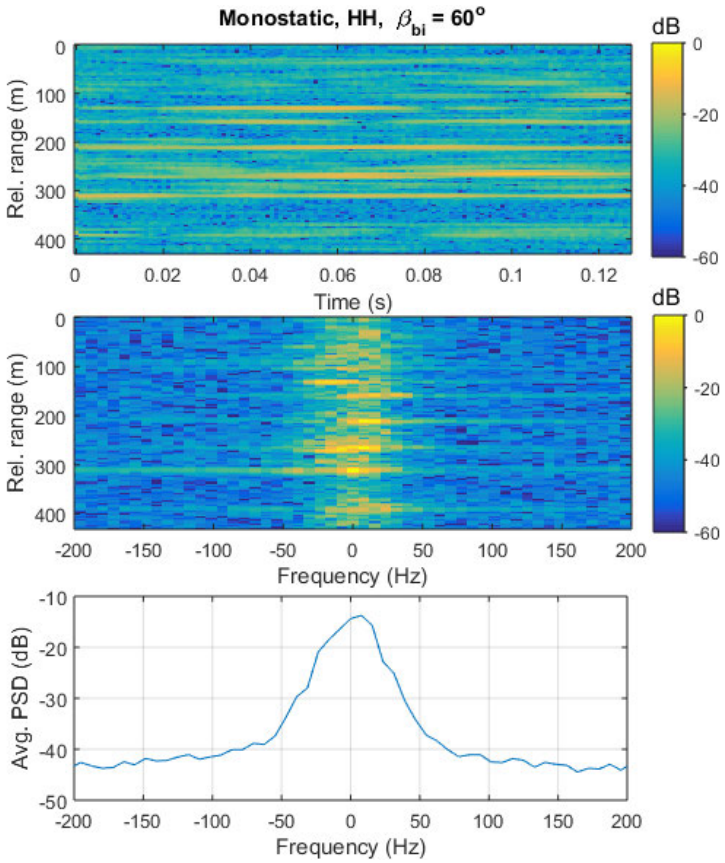

Figure 5.2. NetRAD horizontally polarised monostatic data at $\beta_{\text{bi}} = 60°$: (top) time domain, (middle) PSD, (bottom) averaged PSD.

A detailed study of the mean Doppler spectrum over all monostatic and bistatic collections has revealed 3 dB widths between 10-20 Hz and centre frequencies up to $\pm$ 50 Hz. Figure 5.4 shows the average monostatic (top) and bistatic (bottom) PSDs over range with blue, red dash and black dash-dot lines representing the bistatic angles, β_{bi} = 60°, 90° and 120° respectively. These spectra appear quite Gaussian-shaped with the monostatic results slightly wider than the bistatic results. In general there is little difference between them and also between the different bistatic angles. Note that the monostatic data collected at $\beta_{\text{bi}} = 90°$ contains a small peak at approximately 80 Hz. This appears in only a few range bins and resembles a point target-like component. This could possibly be an extremely fast wave or a recreational boat in the area at the time of the trials. To investigate the component further, we looked at later time blocks and found that the component also exists in the corresponding $\beta_{bi} = 90°$ bistatic data. During the detection process, the component will mask targets which have less power. It will also influence the statistics of the sea clutter and cause the threshold to be higher. This will result in missed detections for weak targets in nearby range bins.

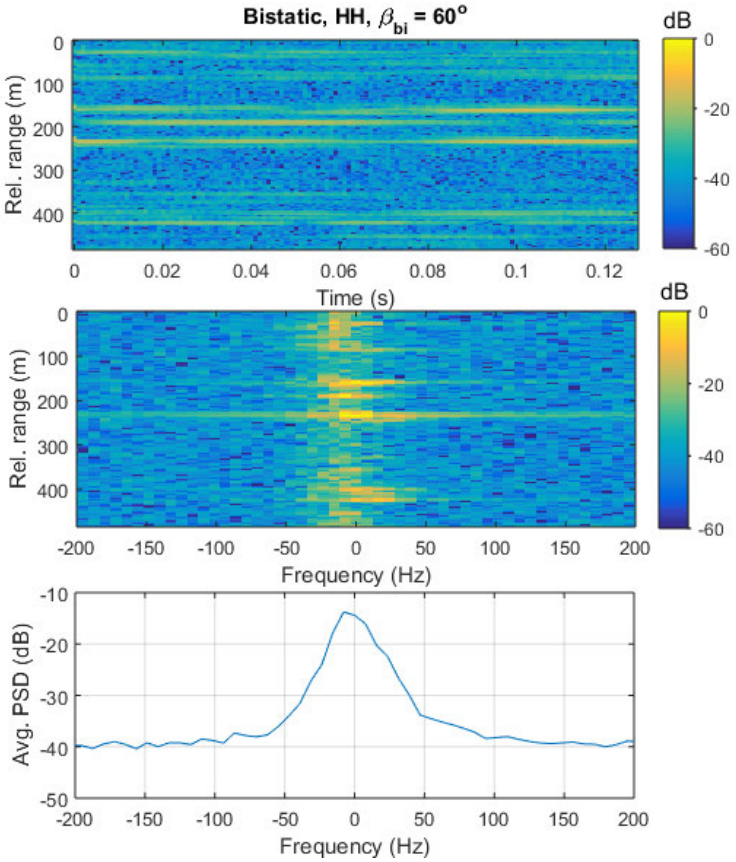

Figure 5.3. NetRAD horizontally polarised bistatic data at $\beta_{\text{bi}} = 60°$: (top) time domain, (middle) PSD, (bottom) averaged PSD.

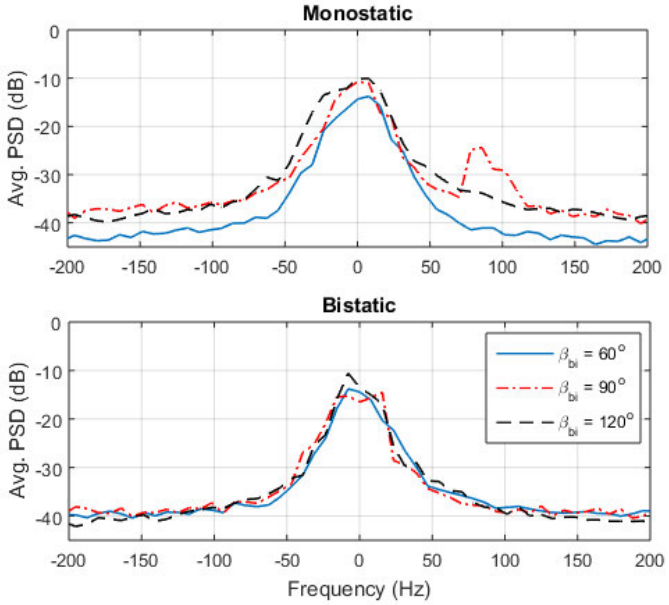

Figure 5.4. Average PSD for both monostatic and bistatic configurations with horizontal polarisation.

The sea-clutter analysed in the previous chapter were recorded in a side looking configuration from a moving airborne platform and has a broad Doppler spectrum. In comparison, the sea-clutter spectrum width of the NetRAD system is much smaller and will require slight modifications to the SWT detection scheme.

5.3 Wavelet Based Detection Scheme

Full details of the SWT detection scheme and its use on the Ingara medium grazing angle data are provided in Chapter 4 and the published work [37]. In this section, a brief summary of the scheme is provided, along with some modifications for the NetRAD data.

5.3.1 Sub-band Isolation

The different time-frequency characteristics of the interference and target implies that some reconstructed sub-bands have a stronger signal to interference ratio (SIR) than the original data. Therefore, with careful selection of these sub-bands, we can utilise the reconstructed data to improve the target detection. In the frequency domain, this can be interpreted as band-pass filtering.

The exact combination of sub-bands needs to be carefully determined for different radar systems. Factors that influence the sub-band choice include the PRF and the Doppler bandwidth of the received signal. For the Ingara data, the sea-clutter Doppler spectrum spans a larger fraction of the unambiguous frequency band, due to the low PRF and the aircraft motion causing the antenna beam to broaden. The sub-band isolation and reconstruction was implemented with the first level detail sub-band, D_1 or approximate sub-band A_1. However, for the NetRAD data, the PRF is 1 kHz and the clutter spectrum has 3 dB widths in the range of 10-20 Hz with a maximum frequency shift of up to ± 50 Hz. For SWT processing, half of the Doppler spectrum is maintained in the approximate sub-band while the other half is maintained in the detail sub-band. For the higher level SWT analysis, the approximate sub-band A is further decomposed. Figure 5.5 (top) shows the 4-level decompositions of the SWT. To reach the edge of the NetRAD clutter spectrum, the SWT must decompose the signal at least 3 times to reduce the spectral width to 62.5 Hz (i.e. $500/2^3$). In this case, the first reconstruction will produce the approximate, $\tilde{A}_3$ and detail, $\tilde{D}_{123}$ reconstructed sub-bands where $\tilde{D}_{123}$ is a combination of detail sub-bands D_1, D_2 and D_3 as illustrated in Figure 5.5 (middle). If the target is embedded in the centre of the Doppler endo-clutter region, a further

decomposition of the A_3 sub-band can be performed. Once reconstructed, this gives two new reconstructed sub-bands: $\tilde{A}_4$ and $\tilde{D}_4$, which are the approximate and detail reconstructed sub-bands at level 4. During the decomposition, a target might be split into two different sub-bands if its frequency is situated in between two frequency regions. If this happens, it can potentially reduce the detection performance and we may consider the combination of D_3 and D_4 to produce a new reconstructed sub-band $\tilde{D}_{34}$ as shown in Figure 5.5.

Based on analysis of the Doppler spectra, it is proposed that $\tilde{D}_{123}$, $\tilde{A}_4$, $\tilde{D}_4$ and $\tilde{D}_{34}$ be used for the detection experiments; $\tilde{A}_3$ is omitted because it contains identical information to $\tilde{A}_4$ and $\tilde{D}_4$ combined. The reconstructed sub-band combination $\tilde{D}_{123}$ is chosen to cover the upper parts of the data which primarily contains thermal noise. The reconstructed sub-band combination $\tilde{D}_{34}$ is chosen to avoid the situation that a target is part way between D_3 and D_4. The PSD of these reconstructed sub-bands are shown in Figure 5.6.

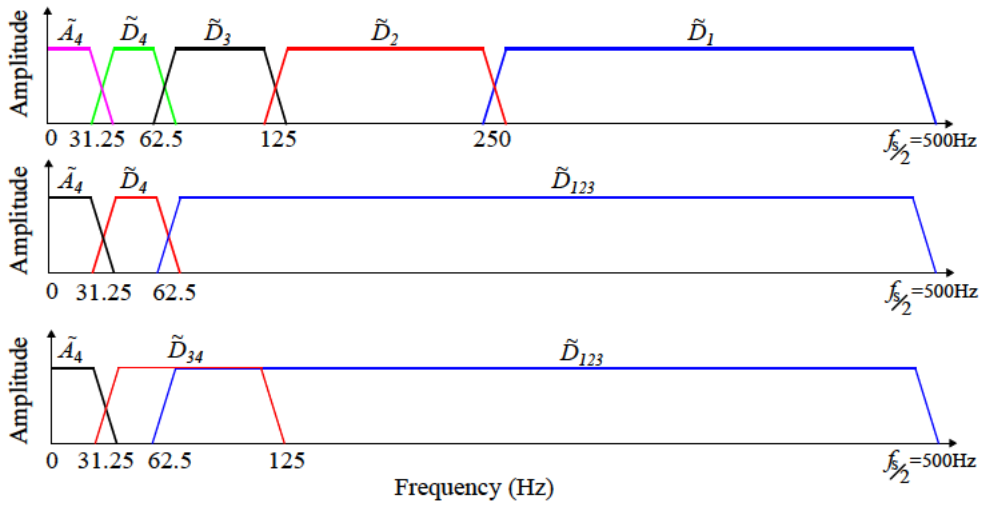

Figure 5.5. One sided frequency spectrum of the multi-level reconstructed sub-bands. f_s is the sampling frequency.

5.3.2 Sub-band Indicator

The sub-band indication scheme, presented in Section 4.7, is used to select the optimal reconstructed sub-band. The selection scheme is employed using the flowchart shown in Figure 5.7 where γ is the maximum entropy value of the range bins in a reconstructed sub-band. The algorithm first compares the value of $\gamma_{\tilde{D}_{123}}$ and $\gamma_{\tilde{A}_3}$. If $\gamma_{\tilde{D}_{123}}$ is greater than $\gamma_{\tilde{A}_3}$, then $\tilde{D}_{123}$ is selected. Otherwise, the data is further decomposed and reconstructed to achieve $\tilde{A}_4$ and $\tilde{D}_4$. A final entropy check then decides on either $\tilde{A}_4$ or the maximum of $\tilde{D}_4$ and $\tilde{D}_{34}$.

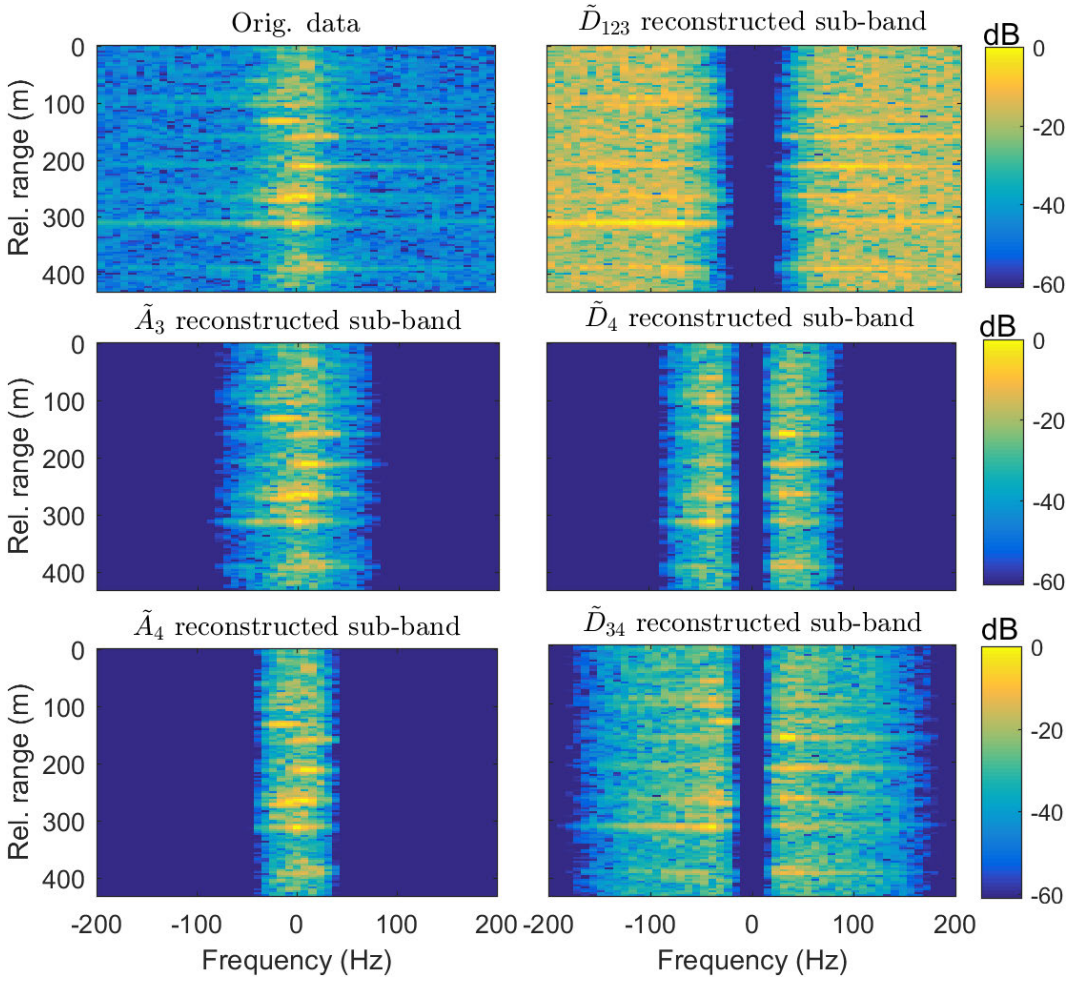

Figure 5.6. NetRAD data PSD after sub-band isolation and reconstruction using an SWT: $\tilde{A}_3$ and $\tilde{A}_4$ are the approximate reconstructed sub-bands of the original data at levels 3 and 4 respectively. $\tilde{D}_{123}$ is the combination of detail sub-bands D_1, D_2 and D_3 while the sub-band $\tilde{D}_{34}$ is the combination of D_3 and D_4.

To demonstrate the entropy variation, a constant RCS (Swerling-0) target is injected into the data. Figure 5.8 shows the entropy metric for a number of reconstructed sub-bands as the SIR increases. Three targets are shown with radial velocities of 0, 1.9 and 6.3 m/s (corresponding to 0, 31.25 and 101.56 Hz respectively). The target velocities are chosen to be at the centre and edge of the endo-clutter region and out in the exo-clutter region. When the target is stationary, the $\tilde{A}_3$ sub-band has the highest maximum entropy followed by $\tilde{A}_4$. Using the logic shown in Figure 5.7, the $\tilde{A}_4$ reconstructed sub-band is selected. For the higher frequency target, the $\tilde{D}_{123}$ reconstructed sub-band has the highest entropy and is selected (bottom of Figure 5.8). Lastly, when the target frequency is 31.25 Hz, the $\tilde{D}_{34}$ reconstructed sub-band has the greatest entropy value followed by $\tilde{D}_4$, $\tilde{A}_3$ and $\tilde{A}_4$. The scheme will select $\tilde{D}_{34}$ over $\tilde{D}_4$ because they both contain the same information.

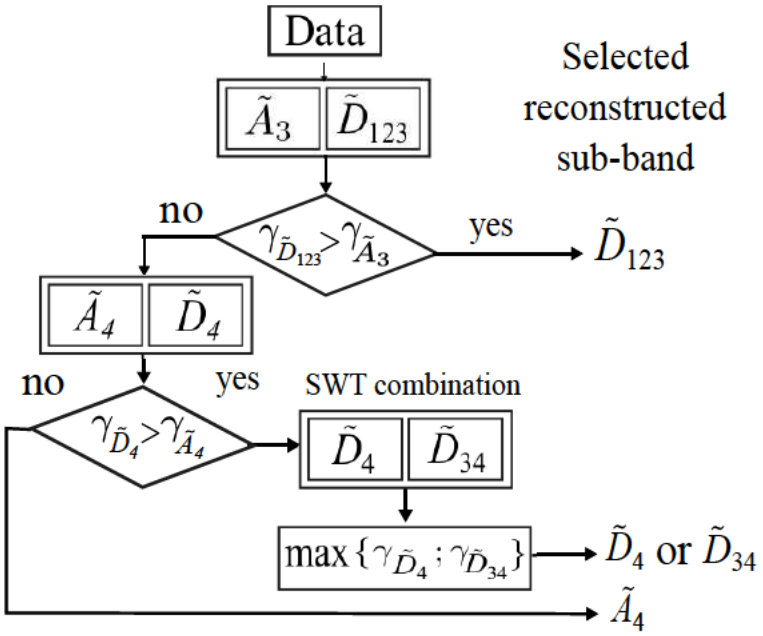

Figure 5.7. Entropy sub-band indication scheme for the NetRAD data: the maximum entropy (γ) is used to indicate the sub-band with the most information about the target.

5.4 Detection Analysis

For the analysis here, a non-fluctuating RCS (Swerling-0) target is used with variations of the target radial velocity. The data blocks used for the comparison are firstly HH and then VV polarisations with bistatic angles 60°, 90° and 120°. Each data block comprises a coherent processing interval (CPI) of 128 pulses with the number of range bins dependent on the bistatic angle. Along with the probability of detection, P_{d}, the number of reconstructed sub-bands is also shown for each result.

To investigate the detection performance using the SWT, a CA-CFAR algorithm is implemented along range to determine an adaptive threshold which adapts to the local clutter and maintains a constant false alarm rate. It is implemented with $M_r = 32$ range bins adjacent to the cell under test. The guard bins on either side of the target are not required because the targets used in the thesis are the simulated point-targets. To determine the threshold multiplier, a common technique is to run the CA-CFAR detection algorithm on the data with no target present. The multiplier is then varied to match the desired probability of false alarm, P_{fa}, which is set to 10^{-3}.

To determine the P_{d}, a Monte Carlo simulation is implemented by repeatedly injecting targets at each range bin. The target SIR is varied and the detection scheme is run. The P_{d} is then

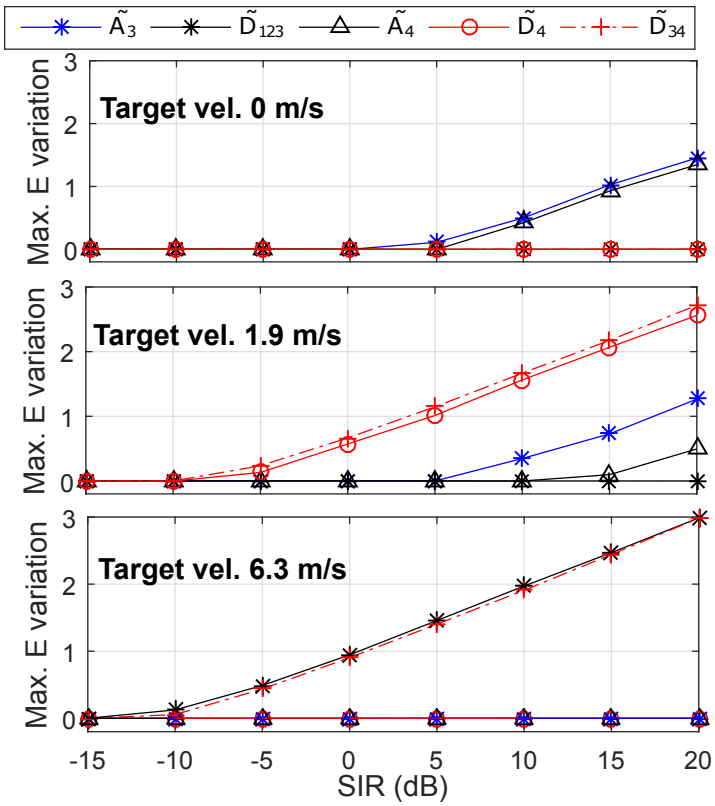

Figure 5.8. Maximum entropy variation with a Swerling-0 target as a function of SIR.

determined by counting the number of detections which cross the threshold. For the SWT scheme, the Daubechies-4 wavelet is used.

5.4.1 HH Polarisation

The first detection results use the HH polarised data. Figures 5.9 and 5.10 show the detection performance at a bistatic angle of 60°. The probability of detection for the three target velocities are shown in the first column as a function of the SIR with the number of times each sub-band is selected shown in the second column. The original (orig) non-filtered detection result is shown in blue, while the best reconstructed sub-band detection results are shown in red, green and black for the three target velocities. The detection result using the entropy indicator is plotted in magenta and denoted as 'eSWT'. For all detection comparisons, the required SIR is compared at $P_{\mathrm{d}} = 0.5$.

For a stationary target, the best reconstructed sub-band is $\tilde{A}_4$, for a target moving with 1.9 m/s, it is $\tilde{D}_4$ and with a velocity of 6.3 m/s, the best result is found in $\tilde{D}_{123}$. When compared to the unfiltered data, the monostatic results show slightly worse performance for the eSWT due to

the ineffectiveness of the indicator, while an increase of 0.6 dB is observed for the bistatic case. However when the target is moving, the eSWT algorithm shows greater improvement. For a slow target moving of 1.9 m/s, the improvement is 9.4 dB and 11.6 dB for the monostatic and bistatic cases respectively. When the target moves faster, the eSWT and the best reconstructed sub-band have the same detection performance. An improvement of 20.9 dB is achieved for the monostatic case and 19.6 dB for the bistatic case at $\beta_{\text{bi}} = 60°$.

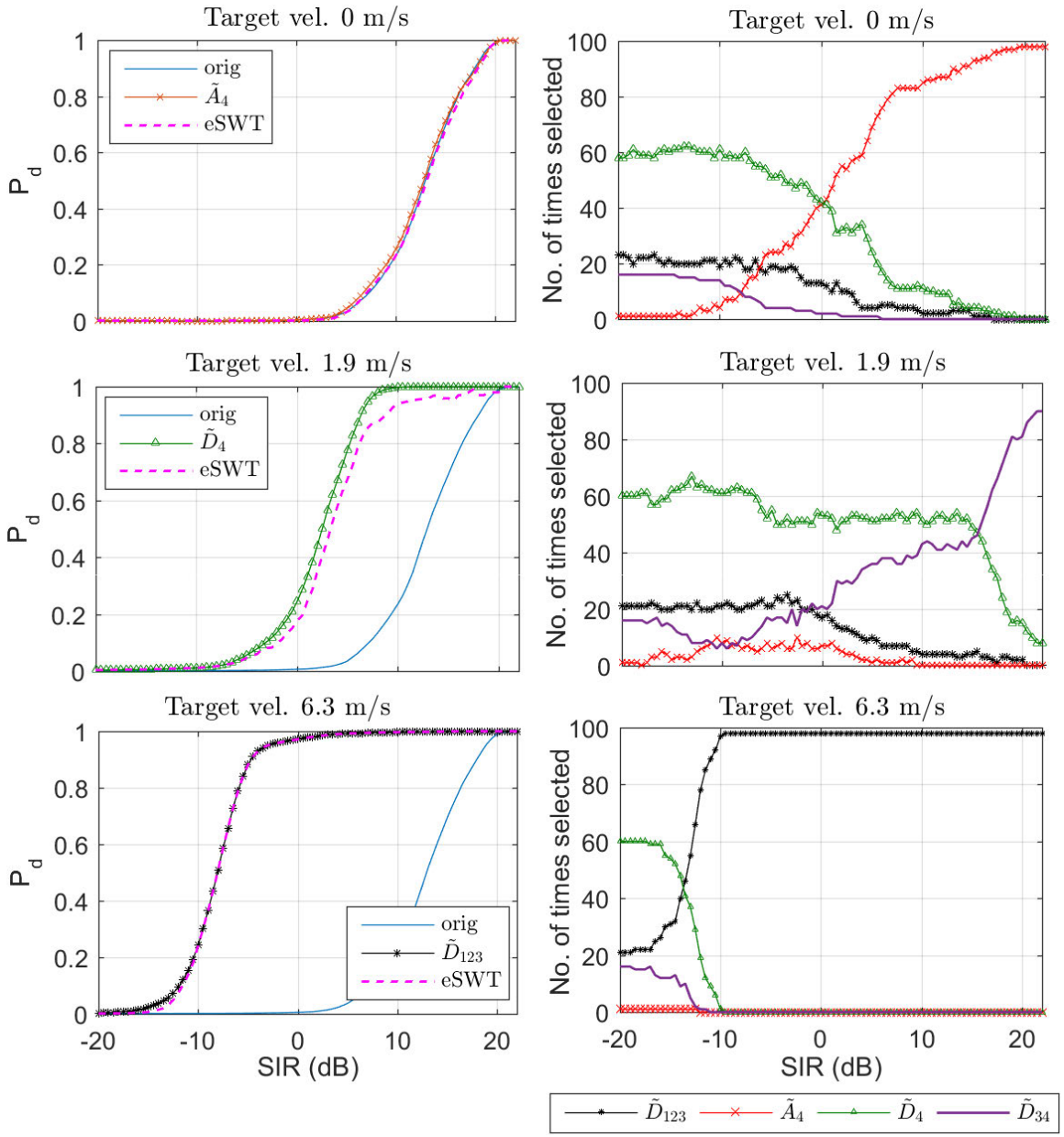

Figure 5.9. The probability of detection (first column) and number of selected sub-bands (second column) for the NetRAD monostatic HH polarisation $\beta_{\text{bi}} = 60°$ and a Swerling-0 target.

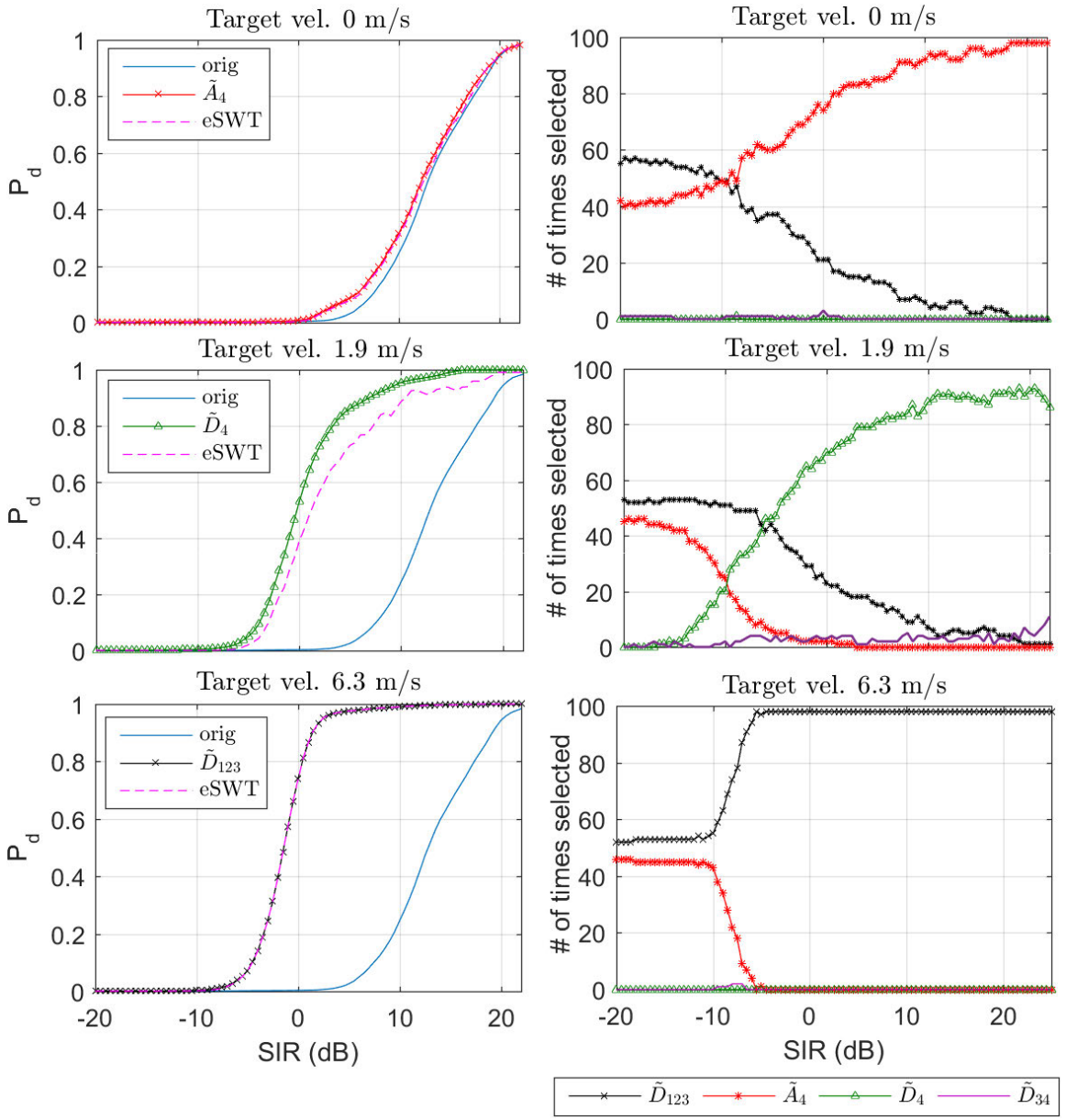

Figure 5.10. The probability of detection (first column) and the number of selected sub-bands (second column) for NetRAD bistatic HH polarisation $\beta_{\text{bi}} = 60^\circ$ and a Swerling-0 target.

Table 5.1 summarises the performance improvement for all bistatic angles (60°, 90° and 120°) when compared to the unfiltered data. It is now clear that there is only a minor improvement between 0.1 to 0.6 dB for the stationary target, with the best results achieved using the 60° bistatic data. For the slow moving target, the bistatic results typically have a larger improvement, with a maximum of 15.6 dB at a bistatic angle of 120°. However, for the slow moving target using the monostatic 90° data, there is a much smaller improvement in the eSWT when compared to the $\tilde{D}_4$ reconstructed sub-band. This is due to the entropy indicator

selecting an incorrect reconstructed sub-band for the detection (i.e. the reconstructed sub-band $\tilde{D}_{123}$ is selected for the detection instead of $\tilde{D}_4$). This confusion is caused by the interfering target as discussed in Section 5.2.2.

Table 5.1. Detection improvement for monostatic and bistatic HH polarised data with a Swerling-0 target. Results are measured at $P_d = 0.5$ and a probability of false alarm of 10^{-3}.

NetRAD		Monostatic			Bistatic		
		60°	90°	120°	60°	90°	120°
Target velocity 0 m/s	$\tilde{A}_4$	0.1	0.5	1	0.6	0.2	0.5
	eSWT	-0.1	0	**0.6**	**0.4**	-1.3	**0.2**
Target velocity 1.9 m/s	$\tilde{D}_4$	10.4	11.6	13.2	13.0	6.7	17.2
	eSWT	**9.4**	**4.2**	**11.5**	**11.6**	**6.0**	**15.6**
Target velocity 6.3 m/s	$\tilde{D}_{123}$	20.9	18.1	19.0	14.3	12.5	19.6
	eSWT	**20.9**	**18.1**	**19.0**	**14.3**	**12.1**	**19.6**

5.4.2 VV Polarisation

The SWT detection scheme is also applied to the VV polarisation. Figures 5.11 and 5.12 show the detection performance (left column) and the number of sub-bands (right column) of the monostatic and bistatic configurations at $\beta_{bi} = 60°$. It can be observed that for the stationary target, the detection improvement of the known reconstructed sub-band is minor and the detection results from the entropy sub-band indicator become slightly worse for some configurations due to the sub-band indicator selecting incorrect sub-bands. For the slow moving target, the best detection results show an improvement of about 11 dB for the monostatic data and 7.4 dB for the bistatic data, respectively. It is also observed that for the slow moving target in the monostatic 60° data, our indicator seems to fail to select the correct sub-band as shown in Figure 5.11 (middle right). This maybe due to a strong breaking wave or another unknown target in the data. When the target moves at higher velocity, the detection improvement is significant for both the known reconstructed sub-band and the entropy selected sub-band. The improvements are 17.7 and 18.3 dB for the monostatic and bistatic data, respectively.

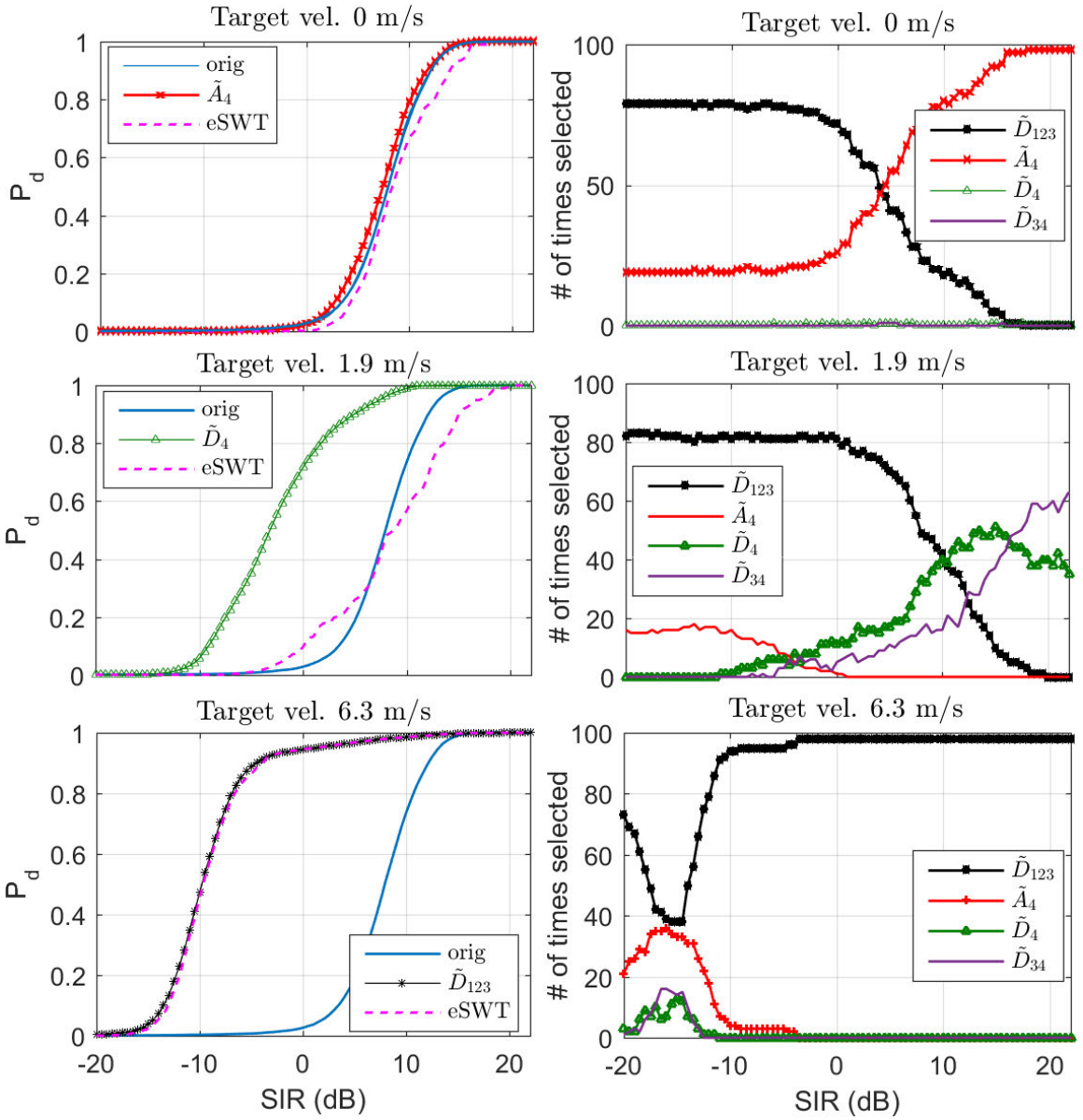

Figure 5.11. The probability of detection (first column) and the number of selected sub-bands (second column) for NetRAD monostatic data and VV polarisation: $\beta_{\text{bi}} = 60°$ and a Swerling-0 target.

The SWT scheme has also been applied to other bistatic angles for the VV polarisation. Table 5.2 gives a summary of the detection improvement for the reconstructed sub-band with known target and unknown target velocity. The table shows that the detection performance using the SWT is larger when the target is non-stationary. The highest detection improvement is 35.8 dB for the monostatic configuration at 120°.

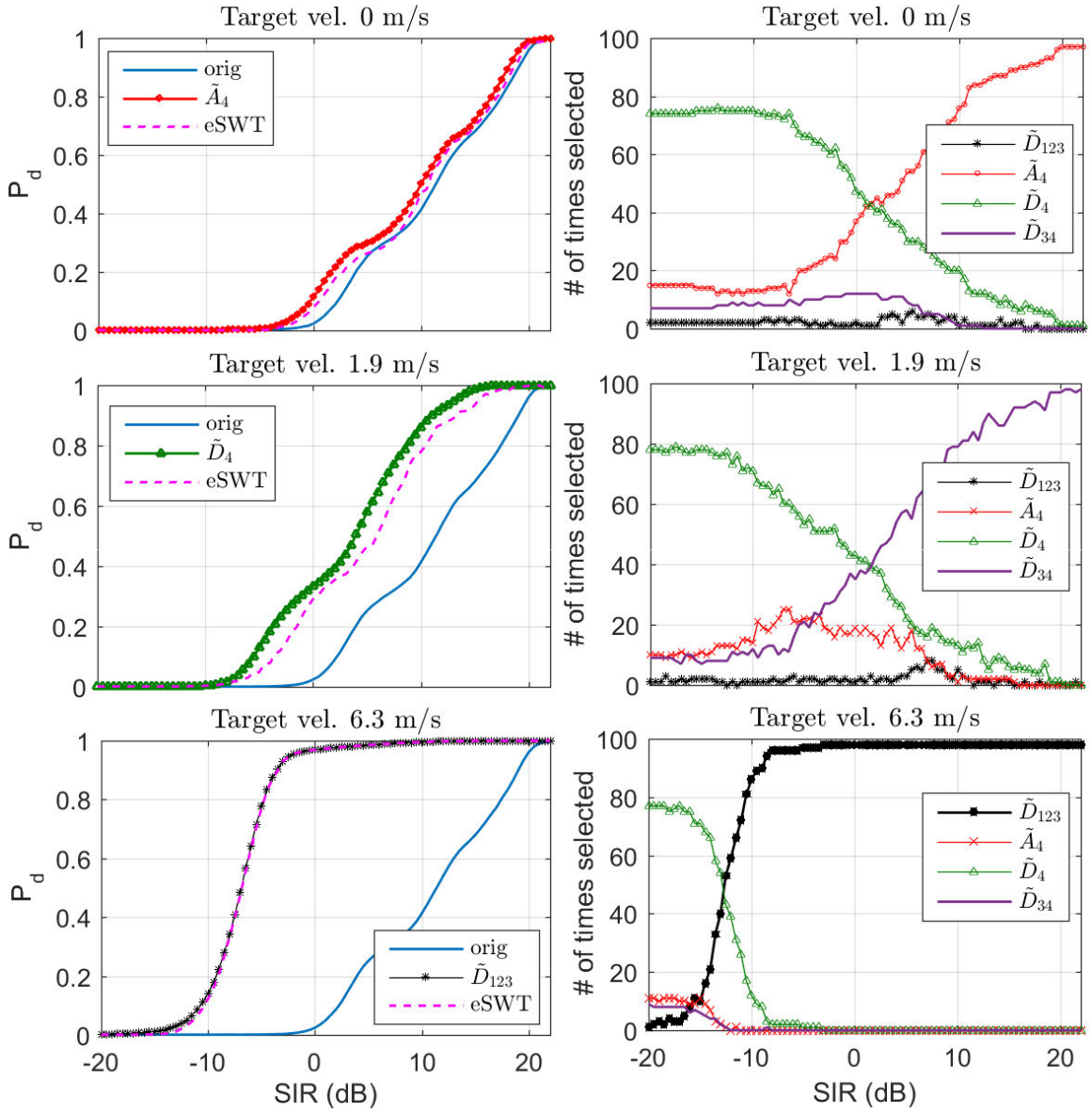

Figure 5.12. The probability of detection (first column) and the number of selected sub-bands (second column) for NetRAD bistatic data and VV polarisation: $\beta_{\text{bi}} = 60°$ and a Swerling-0 target.

5.4.3 Detection Summary and Recommendation

Based on the detection performance and analysis, we found that the proposed SWT detection scheme is robust and performs well for nearly all data sets from both monostatic and bistatic configurations. The detection improvements vary depending on the target velocities. The best detection is found in the monostatic VV polarisation, at the bistatic angle of 120°. In terms of bistatic angles of operation, a conclusive trend cannot be drawn from the SWT detection scheme.

Table 5.2. Detection improvement for monostatic and bistatic VV polarised data with a Swerling-0 target. Results are measured at $P_d = 0.5$ and a probability of false alarm of 10^{-3}.

NetRAD		Monostatic			Bistatic		
		60°	90°	120°	60°	90°	120°
Target velocity 0 m/s	$\tilde{A}_4$	0.45	0.23	0.4	1.4	0.85	0.38
	eSWT	-0.5	-0.25	**0.4**	**0.8**	**0.75**	-0.02
Target velocity 1.9 m/s	$\tilde{D}_4$	11	18.55	16.8	7.4	7.9	19.4
	eSWT	-0.4	**16.35**	**16.5**	**5.4**	**7.75**	**12.1**
Target velocity 6.3 m/s	$\tilde{D}_{123}$	17.7	24	35.8	18.3	10.4	19.75
	eSWT	**17.65**	**23.75**	**35.8**	**18.25**	**9.4**	**19.72**

However, the detection analyses provided here are admittedly only based on limited results from a very short observation time (128 pulses or 0.12 s). Moreover, the data at $\beta_{bi} = 90°$ and $\beta_{bi} = 60°$ of the monostatic HH and VV polarisations appear to contain unexpected targets, making the comparison unclear. Another point to note is that the radar looks at different patches of the sea-surface for every bistatic angle and polarisation and the sea surface structure may be varying between trials. Moreover, the range to the illuminated patch of sea surface is shorter as the bistatic angle β_{bi} increases.

5.5 Conclusion

This chapter demonstrated a SWT-based detection scheme for small target detection in monostatic and bistatic sea-clutter from a ground based radar system at low grazing angles. The first part of this chapter analysed different aspects of sea-clutter which could impact on the detection. It was found that the Doppler spectrum of the sea component was approximately 1/10 of the spectral width of the Ingara data.

With a good understanding of the data, the signal processing method using SWTs was adapted to the NetRAD sea-clutter data. The process of *sub-band isolation and reconstruction* was illustrated with each reconstructed sub-band of the SWT highlighting different features of the sea-clutter to better detect targets. Entropy was then used to select the appropriate reconstructed sub-band when the target velocity is not known prior to its detection.

To demonstrate the SWT scheme, a Monte-Carlo simulation using a CA-CFAR detection algorithm was implemented. The best reconstructed sub-bands with known target velocity were then compared with that determined by an entropy indicator. This analysis revealed that depending on the target velocity and bistatic angle, the improvement over unfiltered data varied between -1.3 dB and 20.9 dB for the HH polarised data and between -0.5 dB and 35.8 dB for the VV polarisation. The entropy indicator was able to successfully determine the 'best' reconstructed sub-band in the majority of cases.

These results demonstrated that the SWT scheme can improve the detection performance in many cases. However, there is no clear indication whether a monostatic or bistatic configuration is more favourable. More trials and analysis are therefore required to clarify which geometry is preferable. When compared with the Ingara medium grazing angle in Chapter 4, the NetRAD results were better for a fast moving target but worse for a stationary target.

Chapter 6

Target Detection in Sea Clutter Using Resonance Based Sparse Signal Separation

SEA clutter and targets often have different characteristics due to their motion. In this chapter, this difference is exploited with a resonance-based sparse signal separation method using the tuned Q-factor wavelet transform (TQWT). The separation is achieved using a basis pursuit denoising (BPD) formulation. This chapter firstly investigates the impact of the regularisation (or penalty) parameter in the BPD algorithm and then proposes an adaptive penalty parameter which dynamically adapts to the sea-clutter intensity across range. A new detection scheme is developed and demonstrated with the Ingara sea-clutter data. Using a Monte-Carlo simulation, a significant detection improvement is achieved.

6.1 Introduction

In previous chapters, a novel detection technique using an application of stationary wavelet transform (SWT) was presented. The technique explored the various levels of SWT decomposition by partitioning the sea-clutter Doppler spectrum into sub-bands. When tested with real radar sea-clutter, significant detection improvements were achieved. Another potentially useful approach to improve the detection performance is to exploit the resonance properties of the clutter and target backscatter. Over a short time period, targets travel at an approximately constant radial velocity resulting in a sustained oscillation. Sea-clutter on the other hand varies with the environmental conditions and has non-sustained oscillations and a wider Doppler spectrum. In this chapter, a resonance-based sparse signal separation technique is investigated for extracting targets from background sea-clutter and improving the detection performance.

Sparse signal separation has been successfully used in various applications such as image denoising, speech recovery and the detection of targets in sea-clutter [41, 43, 75, 77, 100]. Farshchian and Selesnick [43] first applied a resonance-based decomposition using dual tuned Q-factor wavelet transforms (TQWT) to show how to separate targets from any unwanted interference. Nguyen and Al-Ashwal [77] similarly applied the dual TQWT to separate both a rubber inflatable boat and a flock of birds from sea-clutter.

To further understand the choice of the TQWT parameters, Ng et al. [75] investigated the effect of different Q-factors on the target separation. A single Q-factor TQWT decomposed the data into a signal component with a sparse representation and a residue. This used a basis pursuit denoising (BPD) approach. When applied to real data, it was found that a low Q-factor TQWT led to better detection for stationary targets while a high Q transform led to better detection of moving targets. In practice, an important factor in determining the performance of sparse signal separation is the choice of the penalty parameter, λ. When λ is small, the signal component is not very sparse but the reconstruction has high fidelity (small residue); conversely, when λ is large, the signal component is very sparse, but the residue can be large [65]. Anitori et al. [8] proposed a complex approximate message passing (CAMP) iterative algorithm to solve the BPD problem, and applied it to target detection from radar measurements in Gaussian noise. The CAMP threshold parameter (proportional to λ) and the noise variance were adaptively estimated to achieve a sparse solution. It was further shown that the scheme can adaptively control the probability of false alarm against unknown noise and clutter, albeit in a classical detection context.

This chapter uses the TQWT parameters investigated in [75] and focuses on an analysis of the penalty parameter's impact on sea-clutter using a TQWT and the BPD formulation. To be consistent with earlier work [75], the BPD problem is solved using an iterative algorithm known as the 'Split Augmented Lagrangian Shrinkage Algorithm' (SALSA) [2,99], which also runs significantly faster than CAMP. Based on this analysis, an adaptive method is proposed to determine the penalty parameter using statistics of the backscatter to achieve a good sparse representation of the output signal, thus improving the detection of weak targets.

This chapter is organised as follow. Section 6.2 outlines the principle of sparse signal separation and related applications. Section 6.3 give a brief description of TQWTs and the motivation that TQWT is a suitable dictionary for sea-clutter analysis. The results using different TQWT parameters and penalty parameters are presented in Section 6.4, as well as the proposed adaptive penalty parameters. Section 6.5 illustrates the impact of the penalty parameter on sea-clutter and demonstrates the detection performance achieved with the adaptive penalty parameter for both low and high Q-factors.

6.2 Sparse Signal Representation

A signal representation is said to be sparse when it is well approximated by few coefficients. Donoho [32] first proposed the sparse representation technique in the context of compressive sensing, which suggested that a signal can be reconstructed by fewer values without significant degradation. The method has proved to be effective in many fields including astrophysics, machine learning, signal processing and image processing [21, 34, 99]. This section provides an introduction to the theory of sparse signal representation in the context of finding the least square and sparsity-based solution to a problem. A suitable sparse-based method is then proposed for the sea-clutter analysis.

Consider an under-determined linear system defined by equations

$$\mathbf{y} = \mathbf{A}\mathbf{x} + \mathbf{e} \tag{6.1}$$

where

$$\mathbf{y} = \begin{bmatrix} y_0 \\ y_1 \\ \vdots \\ y_{M-1} \end{bmatrix}, \quad \mathbf{x} = \begin{bmatrix} x_0 \\ x_1 \\ \vdots \\ x_{N-1} \end{bmatrix}, \quad \text{and} \quad \mathbf{e} = \begin{bmatrix} e_0 \\ e_1 \\ \vdots \\ e_{M-1} \end{bmatrix}.$$

The vectors $\mathbf{y}$ and $\mathbf{x}$ have length M and N ($M < N$), respectively. The vector $\mathbf{e}$ is an unknown noise (or error term) with the same length as $\mathbf{y}$. The matrix $\mathbf{A}$[1] is the degradation operation (or dictionary) consisting of $M \times N$ elements. The goal is to find a sparse representation $\mathbf{x}$ such that $\mathbf{y} \simeq \mathbf{A}\mathbf{x}$.

The system has more unknowns than equations with no solution when $\mathbf{y}$ is not in the span of the columns of $\mathbf{A}$. To avoid such cases, the matrix $\mathbf{A}\mathbf{A}^T$ is assumed invertible and therefore, the system characterised by Equation (6.1) has infinitely many solutions [40, 101].

The definition of vector norms is given here as it will be used in subsequent sections. Suppose a vector $\mathbf{x} = [x(1), x(2), \cdots, x(N)]^T$ is an N dimensional vector in Euclidean space. The norm of the vector is

$$\|\mathbf{x}\|_p^p = \sum_{n=0}^{N-1} |x(n)|^p \tag{6.2}$$

where $1 \leq p \leq \infty$ and the $p-$norm is also known as ℓ_p-norm of the vector. The ℓ_1-norm (or $\|\cdot\|_1$) is the sum of absolute values of the vector elements, while the ℓ_2-norm (or $\|\cdot\|_2$) is the sum of the element squares and referred to as the 'energy' of $\mathbf{x}$.

6.2.1 Least Squares Approximation

The least squares (LS) formulation is a classic signal estimation technique. From the linear model of Equation (6.1), we can write the error term as:

$$\mathbf{e} = \mathbf{y} - \mathbf{A}\mathbf{x}. \tag{6.3}$$

The ℓ_2-norm of the error term, or the square error, is then given by

$$\begin{aligned} \|\mathbf{e}\|_2 &= \sqrt{e_0^2 + e_1^2 + \cdots + e_{M-1}^2} \\ &= \|\mathbf{y} - \mathbf{A}\mathbf{x}\|_2. \end{aligned} \tag{6.4}$$

This problem is a continuous differentiable unconstrained convex optimisation, which is solved by performing differentiating with respect to $\mathbf{x}$. The solution of Equation (6.4) is explicitly given by [98, 101]:

$$\mathbf{x} = \mathbf{A}^T(\mathbf{A}\mathbf{A}^\mathbf{T})^{-1}\mathbf{y}. \tag{6.5}$$

When the signal, $\mathbf{y}$, is noisy and strongly correlated, the error term can be large (i.e. $\mathbf{A}$ is ill-conditioned) and the estimation becomes meaningless [11, 98]. To overcome that

[1] $\mathbf{A}$ is often referred to as the measurement matrix in compressive sensing literature.

possibility, a regularisation term is required to achieve a stable solution. The fundamental idea of the regularisation is to substitute the original ill-conditioned problem with a well-conditioned problem whose solution approximates the required solution [11]. This problem can be solved using an iterative optimisation method by minimising the cost function to get an approximate solution of Equation (6.1) [11, 101]:

$$\min_{\mathbf{x}} \|\mathbf{y} - \mathbf{A}\mathbf{x}\|_2^2 + \lambda \|\mathbf{x}\|_2^2 \tag{6.6}$$

where $\lambda\|\mathbf{x}\|_2^2$ is the *regularisation* term which is introduced to narrow down the choice of solutions to one well-defined solution. The regularisation parameter λ is added to avoid the system over-estimation or overfitting. The solution to Equation (6.6) is given by

$$\mathbf{x} = (\mathbf{A}^{\mathbf{T}}\mathbf{A} + \lambda \mathbf{I})^{-1}\mathbf{A}^{\mathbf{T}}\mathbf{y}. \tag{6.7}$$

The equations can grow very large if $\mathbf{y}$ and/or $\mathbf{x}$ are long especially in signal processing. Therefore, a fast algorithm is required to solve the system of equations.

6.2.2 Sparse Solutions

In signal processing, another common approach to invert an under-determined system is a technique known as basis pursuit (BP) [22]. This aims to minimise the sum of absolute values of $\mathbf{x}$. The BP equation is given by:

$$\min_{\mathbf{x}} \|\mathbf{x}\|_1 \quad \text{such that} \quad \mathbf{y} = \mathbf{A}\mathbf{x} \tag{6.8}$$

where $\|\mathbf{x}\|_1$ is the ℓ_1-norm. When the signal is noisy, the solution is found by minimising the following cost function:

$$\min_{\mathbf{x}} \{\|\mathbf{y} - A\mathbf{x}\|_2^2 + \lambda \|\mathbf{x}\|_1\} \tag{6.9}$$

where $\lambda\|\mathbf{x}\|_1$ is the ℓ_1-norm regularisation and $\|\cdot\|_2^2$ is the fidelity term. This is also known as basis pursuit denoising (BPD) and in statistical analysis, known as least absolute shrinkage and selection operator (LASSO) [110]. The problem is usually solved using an iterative numerical algorithm rather than computing an analytic solution [101].

As illustrated in Figure 6.1, the sum of squared values in the ℓ_2-norm is most sensitive to large values. Therefore, when performing the minimisation using an ℓ_2-norm, it is vital that the values of $\mathbf{x}$ are small to avoid system overfitting. As a result, sparse solutions are usually not achieved by minimising the ℓ_2-norm [101].

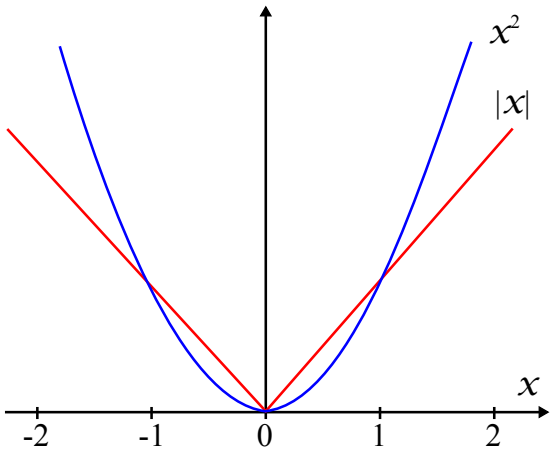

Figure 6.1. The approximate behaviour of functions $|x|$ and x^2 [101].

The problem in Equation (6.6) is convex, smooth and globally differentiable. Similarly the BPD problem in Equation (6.9) is also convex, but is now non-smooth and non-differentiable due to ℓ_1-norm [40]. The BPD problems in Equation (6.9) does not have an explicit solution due to $\|x\|_1$ being non-differentiable at zero [101]. Instead a valid solution can be found using iterative algorithms from optimisation theory [17, 19]. Some of these include Approximate Message Passing (AMP) [33], Complex AMP (CAMP) [66], Iterative Shrinkage-Thresholding Algorithm (ISTA) [11] and Split variable Augmented Lagrangian Shrinkage Algorithm (SALSA) [2]. From these choices, SALSA is found to be the most effective iterative algorithm for obtaining a sparse solution within a reasonable computation time [101].

6.3 Sparse Signal Separation with TQWTs

In this work, sparse signal separation using the BPD method and TQWTs as a dictionary is investigated to isolated targets from the background sea-clutter. When both the BPD algorithm and the TQWT are used, a number of parameters must be known prior to the implementation.

The tuned Q-factor wavelet transform (TQWT) is a flexible time-frequency transform, compared to the conventional dyadic WT. The Q-factor of the dyadic WT is low which can lead to poor frequency resolution and hence only being suitable for piecewise smooth signals [10, 19]. For signals with a higher frequency resolution, the TQWT can be used, with a Q-factor that is adjustable and can be tuned to suit different signals. The details of these transforms are presented in Chapter 3.

A TQWT decomposes a given signal $\mathbf{x}$ into a set of wavelet coefficients $\mathbf{w}$:

$$\mathbf{w} = \mathbf{\Phi}\mathbf{x}, \tag{6.10}$$

where $\mathbf{\Phi}$ is the matrix (or dictionary) corresponding to the TQWT. Each TQWT is characterised by the parameters:

- Q-factor (Q $= \frac{f_c}{B}$): the ratio of centre frequency, f_c, and bandwidth, B.
- Redundancy factor (r): controls the overlapping of the bandpass filter response of multiple sub-bands.
- Decomposition level (K): If one performs K-levels of decomposition, there are K+1 sub-bands (i.e K detail (or high-pass) and 1 approximate (or low-pass) sub-band).

When using the TQWT, the Q-factor is typically chosen so that the wavelet function matches the signal being analysed. It should be set low for impulsive signals without sustained oscillations and high for sustained oscillatory signals. In a multi-level decomposition, the two filter banks of the TQWT are iteratively applied to the low-pass signal with r defining the spectral overlap between two adjacent band-pass filters. The maximum decomposition level, K, that an analysed signal can be decomposed, depends on the parameters: Q, r and the length of the signal.

6.4 Analysis of Sea-Clutter with BPD

For our analysis, the BPD problem using the TQWT is characterised by

$$\min_{\mathbf{w}} \|\mathbf{y} - \Phi^{-1}\mathbf{w}\|_2^2 + \lambda\|\theta \odot \mathbf{w}\|_1 \tag{6.11}$$

where the ℓ_2-norm ($\|.\|_2$) and ℓ_1-norm ($\|.\|_1$) are the *fidelity* and *penalty* terms, respectively, $\odot$ denotes element-wise multiplication, and θ is a vector of the ℓ_2-norms of wavelets needed to satisfy the energy preserving condition of the TQWT.

To apply BPD to the problem of separating targets from sea-clutter, we let $\mathbf{Y}$ denote the radar backscatter in the slow time domain. The separation is then given by

$$\mathbf{Y} = \mathbf{X} + \mathbf{R}, \tag{6.12}$$

where $\mathbf{X}$ is the approximated signal and $\mathbf{R}$ is the residue. Ideally, we would like the $\mathbf{X}$ component to be the target signal, while the interference (clutter and noise) is the $\mathbf{R}$

component. In the analysis, the variation of TQWT parameters is firstly investigated, followed by the choice of penalty parameter.

The Ingara sea-clutter data set is used for this work with Figure 6.2 showing the HH backscatter, collected in the upwind direction at 30° grazing angle. The data are subdivided into 4 blocks of 128 pulses (0.22 s) having 200 range bins per block. The fourth block is selected for analysis as it contains the most sea-clutter variability across range bins. Note that the range bins will be labelled 1 to 200 for the subsequent analysis. Further detail on the data set and the Ingara radar can be found in Section 2.5.1.

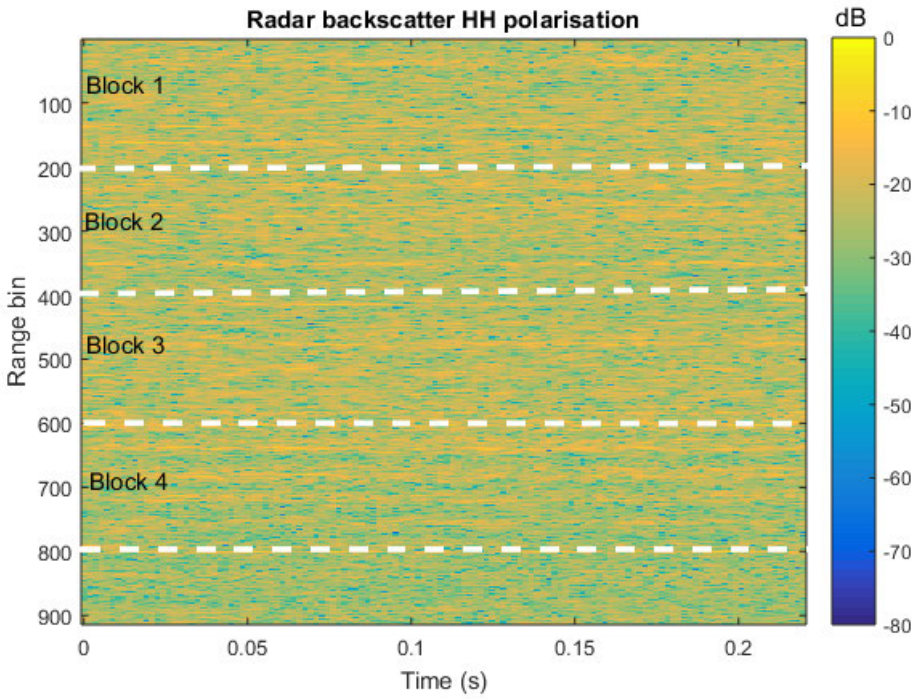

Figure 6.2. Ingara radar backscatter with HH polarisation. Each block consists of 200 range bins by 128 pulses (or 0.22 seconds).

6.4.1 Choice of TQWT Parameters

When using the TQWT, there are three parameters (Q, r and K) which must be set prior to implementation. With extensive simulation, Ng et al. [75] investigated the effect of these parameters for the BPD problem. It was shown that stationary targets are largely captured in the **X** component with a low Q-factor TQWT. Moving targets, on the other hand, are better matched with a high Q-factor TQWT.

To demonstrate the effect of different Q-factors, a stationary and a moving target with a radial velocity of 2.6 m/s and an SIR of 5 dB were injected into range bins 60 and 140 in the selected data block. The BPD problem is then solved for the data using both low Q-factor parameters (Q = 1, r = 2 and J = 3) and high Q-factor parameters (Q = 8, r = 8 and J = 30) based on analysis in [75]. Figures 6.3 and 6.4 show the BPD optimisation output for these cases. In both figures, it is found that the majority of the clutter is contained in the residue component. When the low Q-factor is used, the stationary target is maintained in the **X** component while the moving target is completely rejected. For the high Q-factor, the moving target is now captured in the **X** component and the stationary target is primarily in the residue.

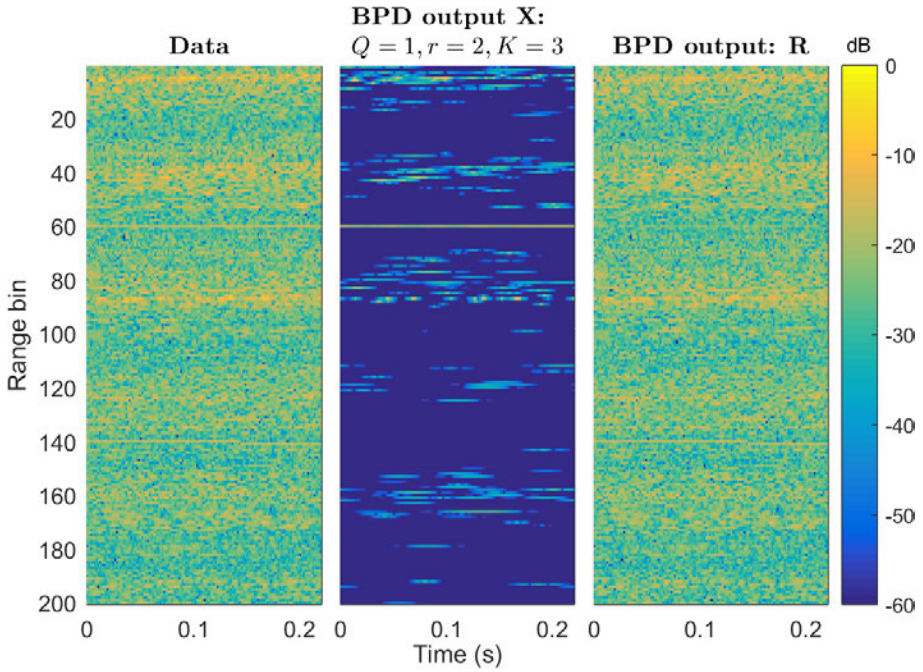

Figure 6.3. BPD output using a low Q-factor TQWT (Q = 1, r = 2 and K = 3). Two simulated point targets with SIRs of 5 dB are injected into the data. The stationary target is at range bin 60 and the moving target is at range bin 140 from the 4^{th} data block.

To illustrate the potential detection improvement of these results, the mean separation between the interference only and interference plus target is now compared along with the difference of the energy ratios of the **X** and **R** components. The energy ratio is defined for each range bin and is determined by summing the power in **X** component and the **R** component over M pulses in the CPI,

$$E_{\text{rat}}(r) = \sum_{m=1}^{M} \frac{|\mathbf{X}_r(m)|^2}{|\mathbf{R}_r(m)|^2} \tag{6.13}$$

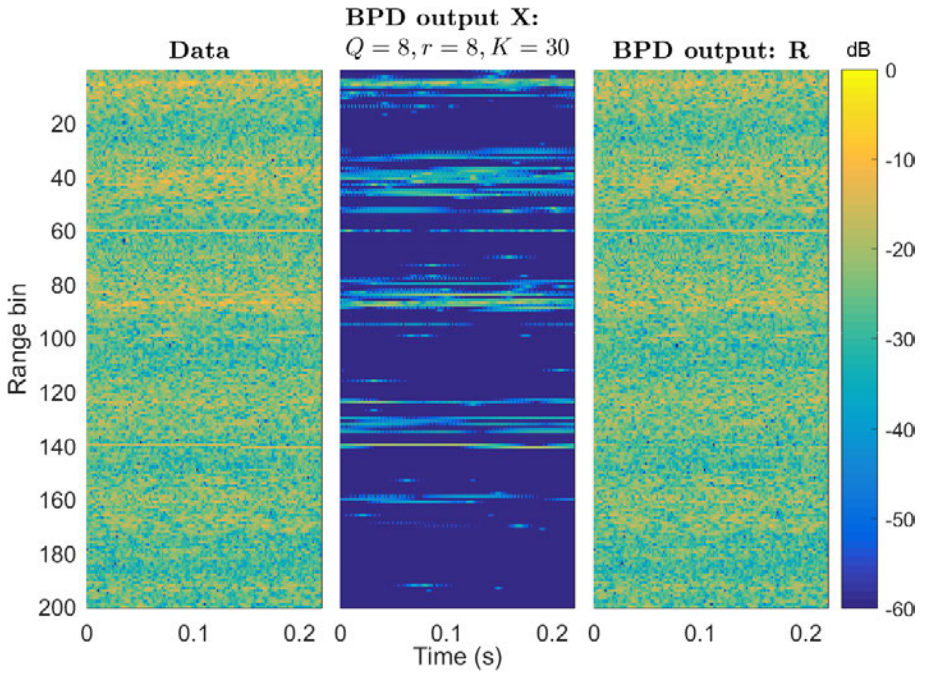

Figure 6.4. BPD output using a high Q-factor TQWT (Q = 8, r = 8 and K = 30). Two simulated point targets with SIRs of 5 dB are injected into the data. The stationary target is at range bin 60 and the moving target is at range bin 140.

where r is the range bin index. If there exists a target in a given range bin, the energy after BPD optimisation ($\mathbf{X}_r$ component) will remain strong while the energy of the same range bin in the residue ($\mathbf{R}_r$ component) will be small. Note that depending on the target velocity, target echoes can span multiple range bins. This must be taken into account when measuring the detection performance. Table 6.1 gives a summary of the mean separation and energy ratio difference of the data after the BPD processing for a range of TQWT parameters. The energy ratio difference and mean separation consistently indicate that the low Q-factor TQWT has the best performance for a stationary target, while the high Q-factor TQWT performs best for the moving target. For more detailed analysis relating to the choice of TQWT parameters, refer to [75].

6.4.2 Penalty Parameter Selection

A crucial factor which impacts the performance of the signal separation is the penalty parameter λ. When the value λ is zero, the obtained $\mathbf{X}$ component is closely matched with the data, while a higher value of λ means that the $\mathbf{X}$ component is sparser in the TQWT domain. The most suitable value for λ depends on the nature of the analysed signal. The main focus of this section is to propose and evaluate a selection technique for λ.

Table 6.1. BPD results of mean separation and energy ratios in dB using different TQWT parameters. A simulated Swerling-0 target with an SIR of 5 dB is used with the best performance highlighted in bold.

TQWT parameters			Stationary target		Moving target	
Q	r	K	Mean separation	Energy ratio difference	Mean separation	Energy ratio difference
1	2	3	**12.51**	**22.43**	-0.78	6.99
3	2	5	3.47	17.78	1.86	14.77
5	4	15	1.74	14.77	5.2	14.77
8	8	30	-1.44	14.77	**5.91**	**17.78**

Detection Statistic

The presence of a target in a range bin usually results in a larger energy ratio, compared to interference only. Ng et al. [75] used this model for detection using a cell averaging constant false alarm rate (CA-CFAR) algorithm. However, in this work, the energy ratio is used directly as a detection statistic:

$$E_{\text{rat}} \underset{H_0}{\overset{H_1}{\gtrless}} \gamma \tag{6.14}$$

where H_0 and H_1 indicate the hypothesis for the returned signal containing interference only and interference plus target, respectively. The choice of the threshold, γ, is somewhat arbitrary and a natural question is how to select a value that leads to sensible results. This choice also influences the spread of points during the pre-processing stage where we estimate λ_0 and η with no targets present. When there is a large γ, the penalty parameters are small with the result having less energy in the **R** component. Conversely, a small γ typically results in a large penalty parameter. From extensive experiments, two discoveries were found. Firstly, good detection performance is achieved when the energy in **R** is greater than the energy in the **X** component. This implies that a suitable upper bound for choosing the threshold is $\gamma < 0$ dB. Secondly, the detection performance is largely insensitive to the choice of γ, over several decades of energy ratio values. A number of experiments were repeated for choices of γ ranging from -10 dB to -80 dB, with differences in the detection performance being negligibly small. If we choose too low a value, numerical problems can occur in the implementation and we therefore set a lower bound on the choice of $\gamma > -100$ dB.

Impact of Penalty Parameter

In previous research on sparse signal separation applied to sea-clutter [43, 75, 77], a global λ was used to analyse the data for all range bins. For example, three stationary Swerling-0 targets are injected into different range bins of the Ingara data set (40, 90 and 140) with SIRs of 5, 2.5 and 0 dB, respectively. As the target is stationary, the TQWT parameters are chosen to be Q = 1, r = 2 and J = 3. In this work, the number of iterations and the selection of μ which affects convergence speed are empirically chosen to be 50 and 2, respectively and are consistent with previous work [75, 77, 99].

Figure 6.5 shows the original data (left) and the $\mathbf{X}$ component with fixed penalty parameters of 0.5 (middle) and 1 (right), after performing the BPD optimisation. When λ is 0.5, the targets are visible, but there is also a large amount of sea-clutter present. However, when λ is set to 1, the $\mathbf{X}$ component maintains the strongest target and parts of the target having SIR = 2.5 dB, with the weakest target eliminated. The BPD optimisation has instead placed it in the residue component (not shown). This analysis has demonstrated that using a uniform or global penalty parameter for all range bins is a trade-off between retaining targets and suppressing sea-spikes.

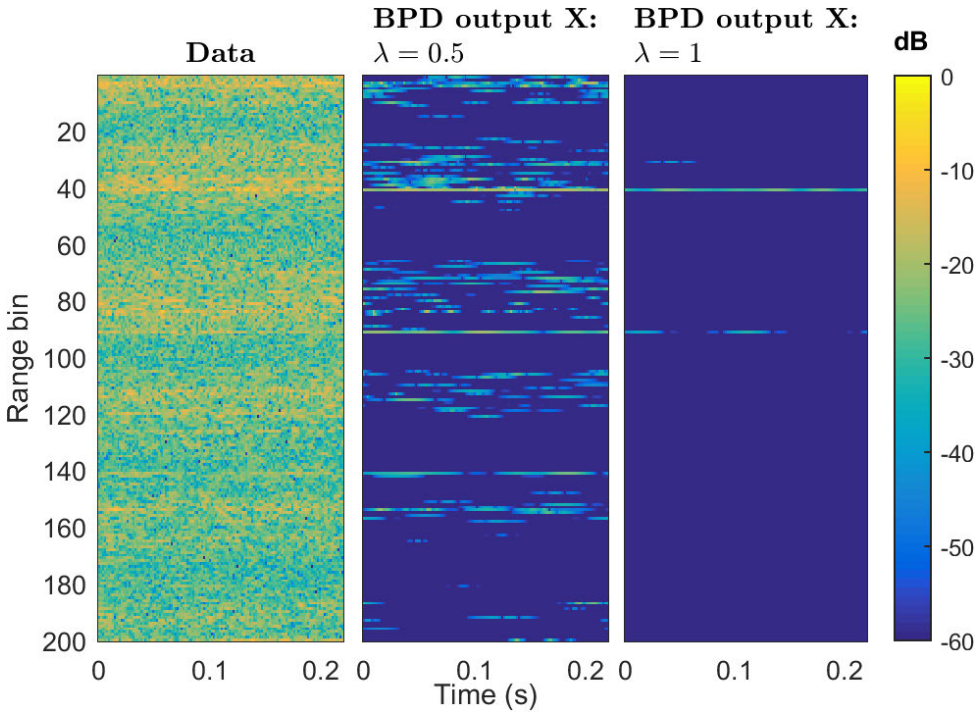

Figure 6.5. Signal separation, $\mathbf{X}$, when the penalty term λ is 0.5 (middle) and 1 (right). The original data is shown on the left.

Adaptive Penalty Parameter

As shown on the left side of Figure 6.5, the Ingara data has strong waves which move through the scene. The radar backscatter corresponding to a crest is indicated by strong returns at approximately every 40 range bins. Since the BPD optimisation is performed independently for each range bin, it is possible to choose penalty parameters that depend on the strength of the signal backscatter. For example, range bins corresponding to the wave crests can have larger penalty parameters than those in the trough.

One measure which clearly shows this fluctuation is the backscatter standard deviation (STD), defined for the r^{th} range bin as σ_r. However, we cannot directly use the STD to scale the penalty parameter, as any strong target will cause the optimisation to weight the penalty term too strongly. To avoid penalising the target, the STD is instead averaged by $M/2$ range cells either side of the range cell of interest. The averaged STD, $\tilde{\sigma}_r(M)$, is shown in Figure 6.6 for different choices of M. From these results, $M = 8$ provides a reasonable amount of smoothing while preserving the shape and is used for the remaining examples.

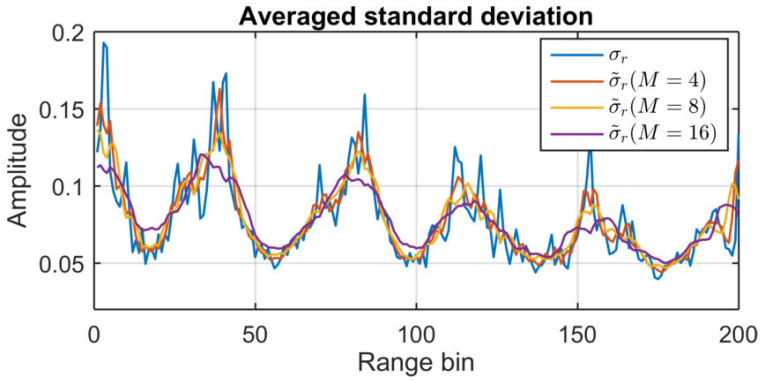

Figure 6.6. Range bin STD, σ_r, and the averaged STD, $\tilde{\sigma}_r$, with: (—) $M = 4$, (—) $M = 8$, (—) $M = 16$.

The proposed adaptive penalty parameter for each range bin is given by

$$\lambda_r = \lambda_0 + \eta \left(\tilde{\sigma}_r(M) - \min\{\tilde{\sigma}_r(M)\} \right), \tag{6.15}$$

where λ_0 is a constant offset for the penalty parameter, η is a multiplier which can be chosen to suit the clutter background and the averaged STD is offset by its minimum value across all range bins. The offset adds a degree of flexibility to allow bigger increases of λ_r at the crests of the waves than in the troughs.

To demonstrate the effect of the adaptive penalty parameter, three examples are shown with $\eta = 0, 2$ and 4 and $\lambda_0 = 0.5$. Figure 6.7 shows the images of the $\mathbf{X}$ components. When the adaptive penalty parameter is used, there is clearly less clutter present in the $\mathbf{X}$ components as the value of η increases.

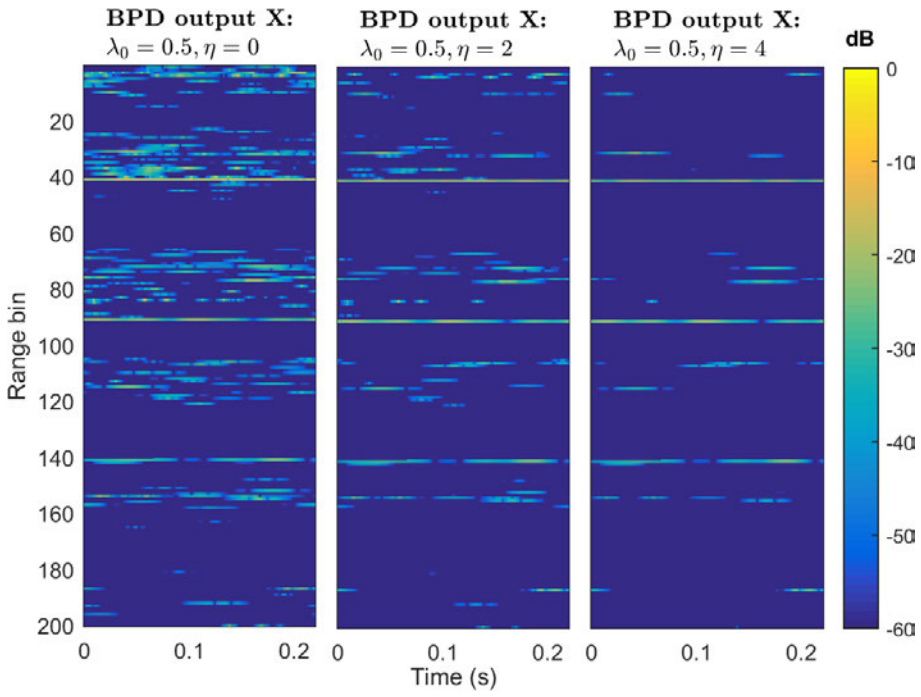

Figure 6.7. BPD output using different sets of adaptive penalty parameters for $\lambda_0 = 0.5$ and $\eta = 0$ (non-adaptive), 2 and 4. The value of M is 8.

To further demonstrate the effect of the adaptive penalty parameter, the energy ratio is measured after the BPD. Figure 6.8 shows the energy ratio of the example dataset with the three targets present. When the penalty term is fixed (left figure), large fluctuations in the energy ratio are observed for different λ_0. However, when adaptive penalty parameters are used, the energy ratios of the data become more uniform, with minimal effect to the targets. If η is further increased above 4, we find that the penalty parameter is too high and the BPD starts to remove too much of the target from $\mathbf{X}$.

Penalty Parameter Model

The penalty parameters for both adaptive and non-adaptive cases must be determined prior to performing BPD signal separation from background data which is known to be free of any targets. For the adaptive penalty parameter technique, two parameters λ_0 and η must be determined, while the non-adaptive formulation requires only an estimation of the intercept λ_0

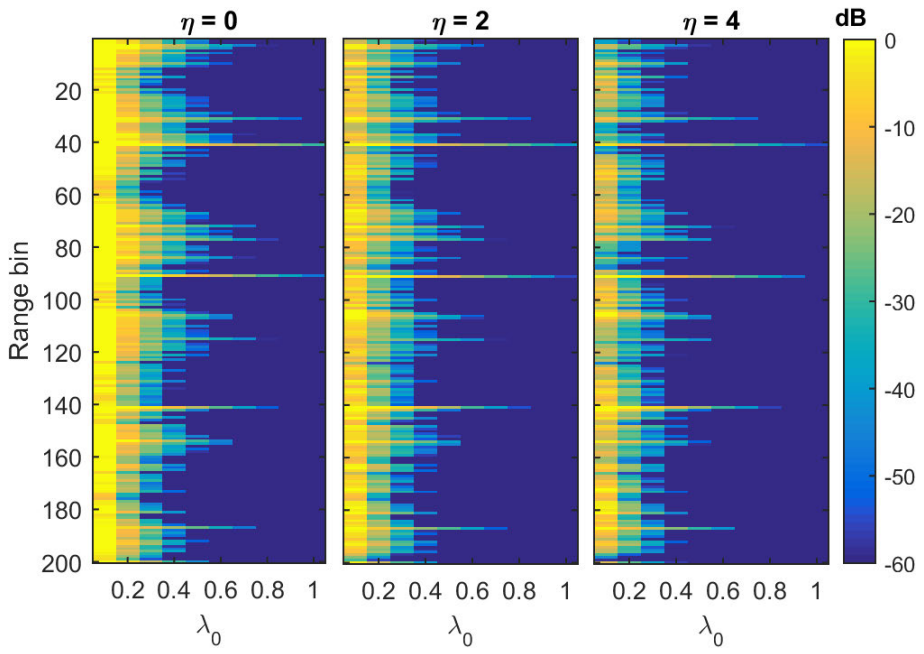

Figure 6.8. Energy ratio after BPD for $\eta = 0, 2$ and 4. Three targets having SIRs of 5, 2.5 and 0 dB are present at range bins 40, 90 and 140, respectively.

because η is set to zero. For the adaptive case, one possible approach to estimate the parameters is to determine a linear fit to the energy ratio. Then we shift the model to achieve a desired level of residual clutter or P_{fa} in the $\mathbf{X}$ component. For the analysis, 9 additional blocks of target free data are used to achieve a $P_{\text{fa}} = 10^{-3}$. Since the energy ratio after BPD can get very small for large values of the penalty parameter, a minimum value for the energy ratio is set to $\gamma = -60$ dB, well within the recommended range of -100 dB $< \gamma < 0$ dB found earlier.

Figure 6.9 shows a scatter plot of the HH polarised energy ratios as a function of penalty parameters λ_r and the averaged standard deviation $(\tilde{\sigma}_r - \min\{\tilde{\sigma}_r\})$. The blue circles indicate the required λ_r to achieve an energy ratio of -60 dB at each range bin. The red line is the linear fit representing the variation in energy ratio for different range bins. It is observed that the penalty parameter increases with the standard deviation. The line is then shifted upward by increasing the intercept of the red line to achieve the desired P_{fa} of 10^{-3}. For the 2000 data points in Figure 6.9, this corresponds to 2 points above the black line. The intercept and slope of the black line are $\lambda_0 = 0.8$ and $\eta = 3.76$, respectively. For the non-adaptive penalty case, the line is horizontal and the slope η is zero. This is represented by the magenta line in Figure 6.9 with $\lambda_0 = 1.06$. This approach for selecting λ_0 and η is quite heuristic, but provides a straightforward method for achieving the desired P_{fa} without requiring an analytical study of the detection statistics.

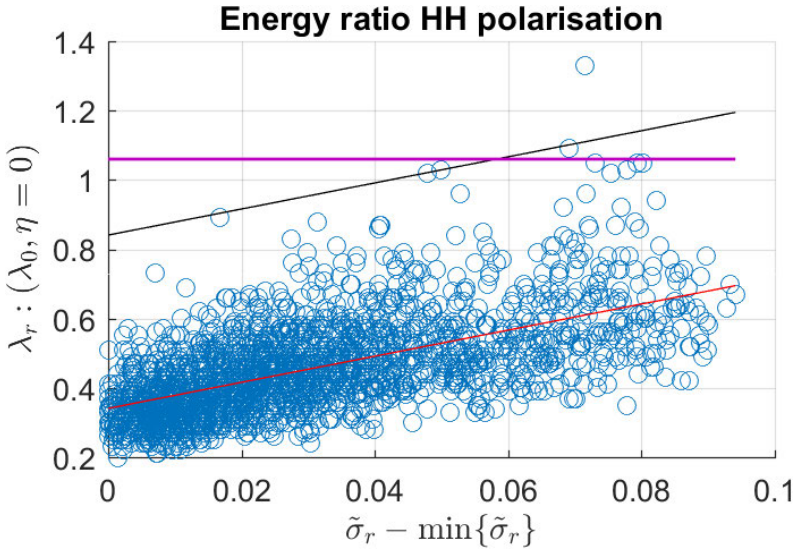

Figure 6.9. Scatter plot of the energy ratio at $\gamma = -60$ dB for each range bin with HH polarisation. The vertical axis is the penalty parameter required for BPD and the horizontal axis is the standard deviation: $(\tilde{\sigma}_r - \min\{\tilde{\sigma}_r\})$. The red line (—) is the best fit to the energy ratio, while the black line (—) and the magenta line (—) represent the adaptive and non-adaptive penalty parameters respectively.

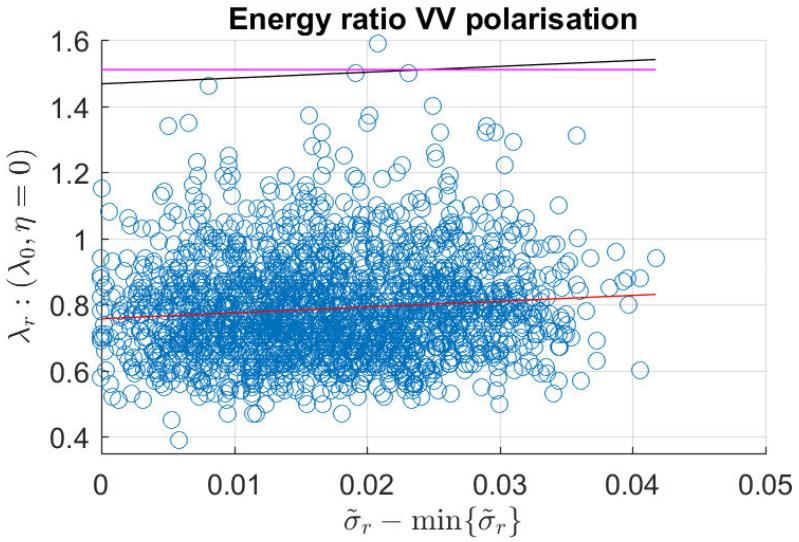

Figure 6.10. Scatter plot of the energy ratio at $\gamma = -60$ dB for each range bin with VV polarisation. The vertical axis is the penalty parameter required for BPD and the horizontal axis is the standard deviation: $(\tilde{\sigma}_r - \min\{\tilde{\sigma}_r\})$. The red line (—) is the best fit to the energy ratio, while the black line (—) and the magenta line (—) represent the adaptive and non-adaptive penalty parameters respectively.

Figure 6.10 shows the same scatter plot for the VV polarisation. The energy ratios do not vary as greatly with $(\tilde{\sigma}_r - \min\{\tilde{\sigma}_r\})$ compared to the HH polarisation. As a result, the fitting line (red) is relatively flat. The intercept λ_0 and slope η of the shifted version of the fitting line are 1.46 and 1.67, respectively. The non-adaptive penalty parameter is represented by the horizontal magenta line with an intercept, $\lambda_0 = 1.51$. A small value of slope for the adaptive case means that the algorithm requires less adaptation and the data has less variation across range. In comparison, the penalty parameters in VV are bigger than those in the HH polarisation when setting the same P_{fa}. Another point to note is the smoothed standard deviation in the VV polarised data is about half of the HH polarisation, meaning that the HH backscatter varies more than the VV backscatter.

6.5 Detection Performance

The new detection scheme is now investigated with and without the adaptive penalty parameter. The results of the BPD detection scheme will then be compared against the detection of unprocessed data using a cell averaging constant false alarm rate (CA-CFAR) scheme. Note that due to the time and range varying nature of the spectrum, we do not consider any coherent processing techniques. Two types of fluctuating targets (Swerling-0 and Swerling-1) are investigated in both HH and VV polarised data. We also use low Q-factor TQWT parameters (Q = 1, r = 2 and K = 3) for the injected stationary target and high Q-factor TQWT parameters (Q = 8, r = 8, and K = 30) for the moving target with a radial velocity of 2.6 m/s.

6.5.1 Detection Implementation

The adaptive and non-adaptive penalty parameters used for BPD are described in Section 6.4.2 such that the probability of false alarm P_{fa} is 10^{-3}, for a chosen threshold $\gamma = -60$ dB. The detection results are compared to the detection of unprocessed (original) data using a CA-CFAR detection scheme, applied to the data intensity. The CA-CFAR algorithm is implemented along range and adapts to the local clutter to approximately maintain a constant false alarm rate. It is implemented with $M_r = 32$ range bins adjacent to the cell under test. Since the targets used in the thesis are the simulated point-targets, the guard bins on either side of the target are not required. To determine the threshold multiplier, the CA-CFAR detection algorithm is run on the data with no target present. The multiplier is then varied to match the desired probability of false alarm, P_{fa}.

To determine the probability of detection, P_d, a Monte Carlo simulation is implemented by repeatedly injecting simulated targets into each range bin. The target SIR is then varied and the various detection schemes are run. The P_d is then determined by tallying the number of correct detections. Refer to Section 2.4 for more detail on the Monte-Carlo simulation and the CA-CFAR algorithm.

6.5.2 Low Q-factor TQWT Detection

Figure 6.11 shows the probability of detection versus SIR for the processed and unprocessed data for HH (top) and VV (bottom) polarisations with a constant Swerling-0 target. As the target is stationary, the data was processed using the low Q-factor TQWT parameters (Q = 1, r = 2 and K = 3). The CA-CFAR conventional detection scheme for the unprocessed data is shown in Figure 6.11 by the blue solid line, while the detection using the non-adaptive (or fixed) and adaptive penalty parameters are shown in red dashed and black dash-dot lines, respectively. The minimum required SIRs to achieve a probability of detection, $P_d = 0.5$ are measured to show the improvement in performance. Firstly, we can observe that the required SIR for the HH polarisation using both non-adaptive and adaptive penalty parameter schemes have significant improvements of 11.25 dB and 12.75 dB over the unprocessed data. That is, the adaptive penalty parameter provides an improvement of 1.5 dB over the non-adaptive scheme. For the VV data, the detection improvements over the unprocessed data using the non-adaptive and adaptive schemes are 8.6 dB and 8.7 dB, respectively. The similar detection performance of non-adaptive and adaptive penalty parameters highlight that backscatter from the VV polarisation fluctuates less than the HH polarisation. It can be observed that the red curve jumps above the black curve for the P_d near 1. This is due to the penalty parameter setting for the adaptive case being greater than in the non-adaptive case (see Figures 6.9 and 6.10). It is also interesting to note that the target is better detected in the VV polarisation when the CA-CFAR scheme is used but after BPD, the detection improvement is less than the improvement with the HH polarisation.

Figure 6.12 shows the detection performance when a fluctuating Swerling-1 target is injected into the HH (top) and VV (bottom) polarisations. In general, the detection of Swerling-1 targets requires a higher SIR to achieve the same P_d than a Swerling-0 target. For the HH polarisation, the detection improvement over unprocessed data is approximately 11.5 dB and 12.5 dB for the schemes using non-adaptive and adaptive penalty parameters, respectively. For the VV polarisation, the improvement is approximately 9 dB for both non-adaptive and adaptive BPD schemes.

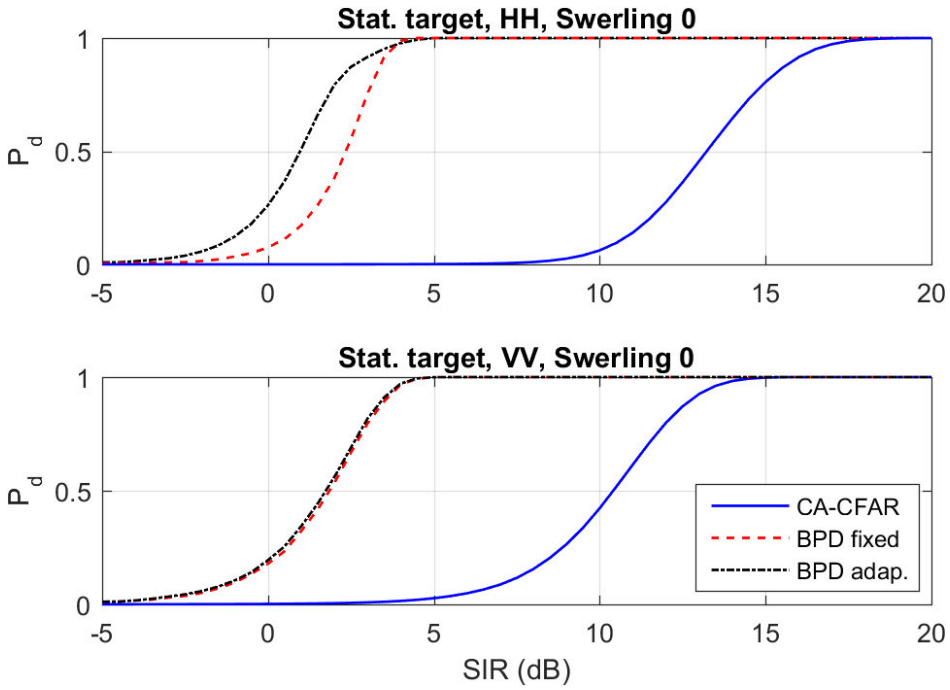

Figure 6.11. Detection performance of Swerling-0 targets with HH (top) and VV (bottom) polarisations: (—) CA-CFAR, (- - -) fixed penalty parameter (BPD-fixed), (-·-·-) adaptive penalty parameter (BPD-adap.).

6.5.3 High Q-factor TQWT Detection

To investigate the performance of the BPD scheme with a high Q-factor TQWT, a moving target is now injected into the data. In this analysis, the TQWT parameters are Q = 8, r = 8 and K = 30 which are found to have the best signal separation for a target with radial velocity of 2.6 m/s [75]. One key difference for moving targets is that their backscatter drifts from one range bin to the next over the CPI and hence the detection improvement may be reduced.

Similar to the low Q-factor procedure, we have to first determine the required penalty parameters prior to performing the BPD detection scheme. Figure 6.13 shows the scatter plot of required penalty parameter versus $(\tilde{\sigma}_r - \min\{\tilde{\sigma}_r\})$ for the high Q-factor parameters. The blue circles indicate the required λ_r for a given $(\tilde{\sigma}_r - \min\{\tilde{\sigma}_r\})$ to sustain the energy ratio of $\gamma = -60$ dB at each range bin. The red line represents the energy ratio fit, while the black and magenta lines denote the required adaptive and non-adaptive penalty parameters respectively. The left figure of Figure 6.13 is for the HH polarisation, while the VV polarisation is on the right.

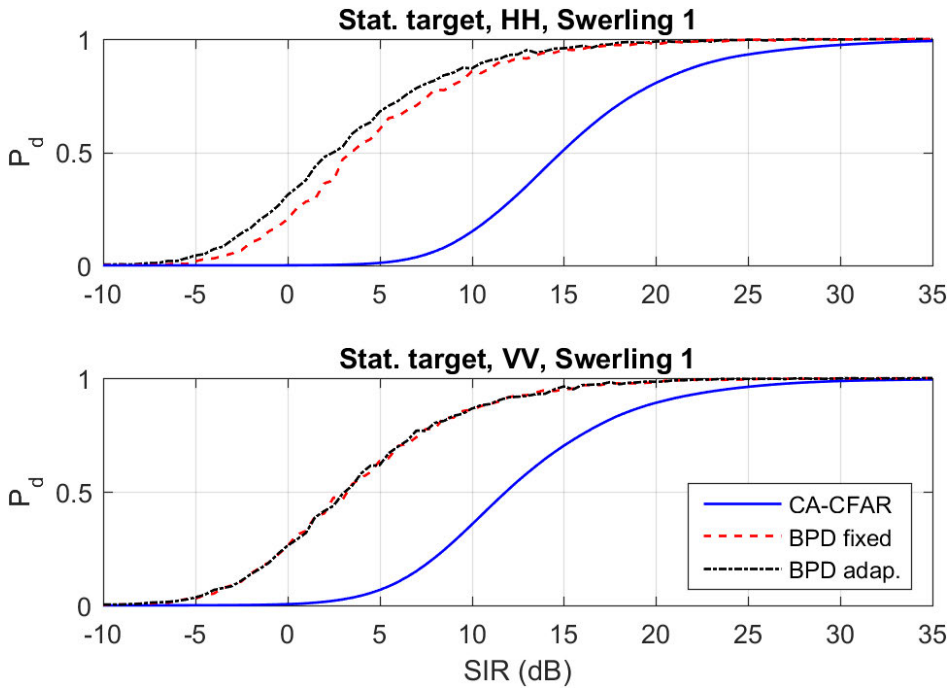

Figure 6.12. Detection performance of Swerling-1 targets with HH (top) and VV (bottom) polarisations: (—) CA-CFAR, (- - -) fixed penalty parameter (BPD-fixed), (-·-·-) adaptive penalty parameter (BPD-adap.).

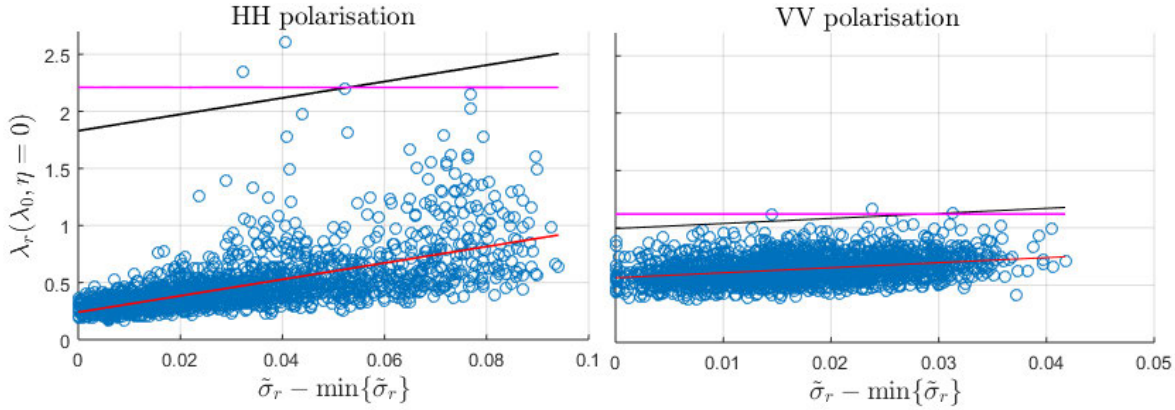

Figure 6.13. Scatter plot of the energy ratio at $\gamma = -60$ dB using a high Q-factor TQWT for each range bin with HH (left) and VV (right) polarisations. The vertical axis is the penalty parameter required for BPD and the horizontal axis is the standard deviation: $(\tilde{\sigma}_r - \min\{\tilde{\sigma}_r\})$. The red line (—) is the best fit to the energy ratio, while the black line (—) and magenta line (—) denote the adaptive and non-adaptive penalty parameters respectively.

In the HH polarisation, there are a few outliers as the penalty parameter is quite high in order to sustain the -60 dB energy ratio. These outliers were found to correspond to sea-spikes and

are well-matched to the high Q-factor wavelet. The computed values of λ_0 and η for the adaptive case are 1.8 and 7.2 respectively. The fixed penalty parameter is $\lambda_0 = 2.2$. For the VV polarisation, the required penalty parameter is relatively constant to maintain the energy ratio of -60 dB. The slope of the adaptive penalty parameter is relatively small with parameters, $\lambda_0 = 0.98$ and $\eta = 4.4$ while the non-adaptive case has $\lambda_0 = 1.1$.

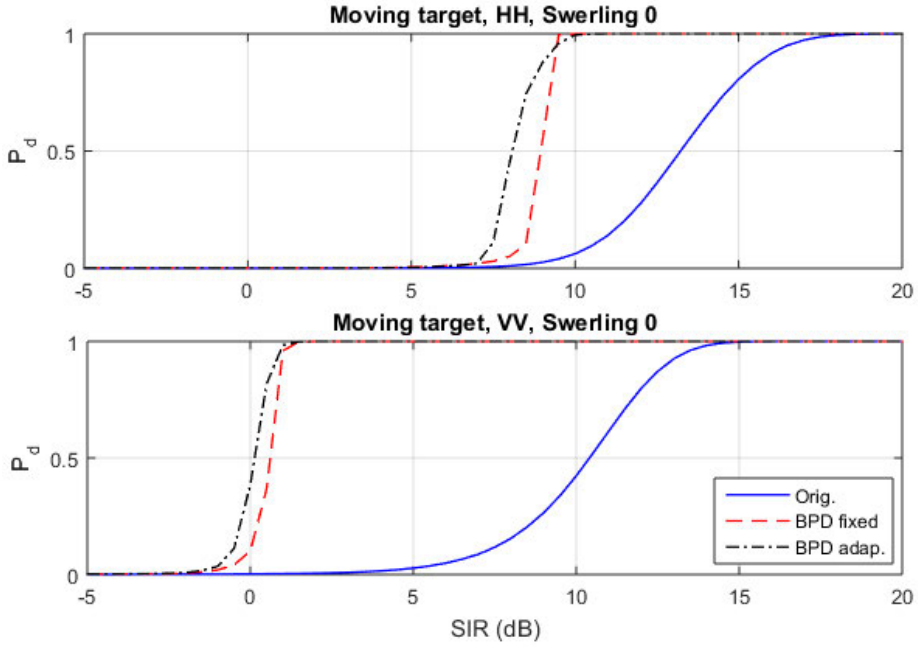

Figure 6.14. Detection performance of Swerling-0 targets using a high Q-factor TQWT with HH (top) and VV (bottom) polarisations: (—) CA-CFAR, (- - -) fixed penalty parameter (BPD-fixed) and (-·-·-) adaptive penalty parameters (BPD-adap.).

Figure 6.14 shows the detection performance of a Swerling-0 target for the HH (top) and VV (bottom) polarisations. These results show much steeper curve for the BPD due to combination of the Swerling-0 target and the high Q-factor TQWT. Moreover, the detection improvement for the HH polarisation in this case is decreased when compared to the low Q-factor TQWT due to the high setting of penalty parameters as shown in Figure 6.13. For the HH polarisation, we observe that the detection performance using non-adaptive and adaptive BPD schemes give improvements of 4.25 and 5.15 dB, respectively. These improvements are relatively small for both cases, possibly due to high penalty parameter. The detection performance in the VV polarisation does not suffer from the high penalty parameter and has an improvement of 9.8 dB and 10.37 dB for the non-adaptive and adaptive penalty schemes, respectively.

The BPD scheme with a high Q-factor is also used to investigate the detection performance for a Swerling-1 target. It is worth mentioning that the effects in the HH polarisation caused

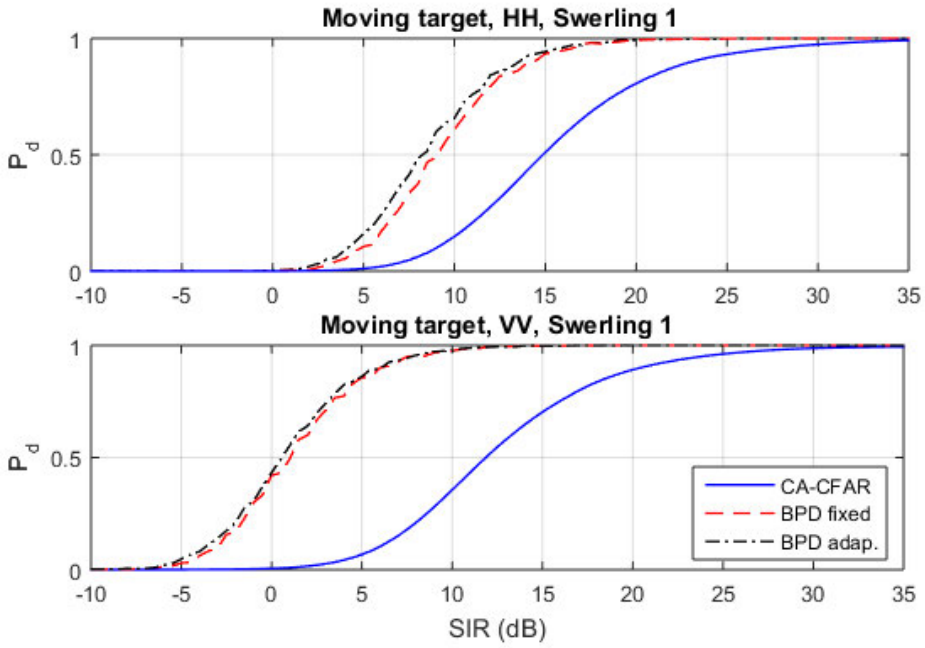

Figure 6.15. Detection performance of Swerling-1 targets using a high Q-factor TQWT with HH (top) and VV (bottom) polarisations: (—) CA-CFAR, (- - -) fixed penalty parameter (BPD-fixed) and (-·-·-) adaptive penalty parameter (BPD-adap.).

by the outliers will also impact the detection of the Swerling-1 targets. Figure 6.15 shows the detection performance using the BPD scheme with a high Q-factor TQWT for the HH (top) and VV (bottom) polarisations. The detection improvement for the HH polarisation is 5.7 dB and 6.6 dB for non-adaptive and adaptive schemes respectively. For the VV polarisation, the detection improvement is 11 dB and 11.5 dB.

6.5.4 Detection Summary

For a comparison of all the results, Table 6.2 shows a summary of the detection improvements using the BPD scheme with non-adaptive and adaptive penalty parameters. The table also includes the detection improvement for the HH and VV polarisations and both Swerling target fluctuations.

The proposed BPD detection scheme offers a significant improvement over the unprocessed data for both polarisations and target fluctuations. The biggest improvement is achieved for the HH polarisation when the low Q-factor TQWT parameters are used with a stationary target. The second main result is that the BPD scheme with an adaptive penalty parameter provides better detection performance over the non-adaptive case for both low and high Q-factors and also in

Table 6.2. Summary of non-adaptive and adaptive BPD detection improvements (minimum required SIR) when measured at $P_d = 0.5$. Two sets of TQWT parameters are used for the detection in HH and VV polarisations with two types of target fluctuations (Swerling-0 and 1). Note: when low Q-factor TQWT is used, the target is stationary and when high Q-factor is used, the target moves with a radial velocity of 2.6 m/s.

TQWT			Pol.	Fixed penalty BPD				Adaptive Penalty BPD			
Q	r	K		λ_0	η	P_d Improvement (dB)		λ_0	η	P_d Improvement (dB)	
						Swerling-0	Swerling-1			Swerling-0	Swerling-1
1	2	3	HH	1.06	0	**11.25**	**11.5**	0.84	3.77	**12.75**	**12.5**
			VV	1.51	0	8.6	8.75	1.46	1.67	8.75	9
8	8	30	HH	2.2	0	4.25	5.7	1.8	7.2	5.15	6.6
			VV	1.1	0	**9.8**	**11**	1	4.4	**10.37**	**11.5**

both polarisations. Thirdly, the BPD detection results using a low Q-factor in HH polarised data is better than the VV polarisation for both types of targets due to the required penalty parameters being greater for the VV polarisation. However, when a high Q-factor TQWT is used for detecting moving targets, the performance levels are reversed: the detection in the VV polarisation is better than HH due the higher penalty parameters. Another interesting point to note is that Swerling-1 targets have a slightly better detection improvement than the Swerling-0 target when a high Q-factor TQWT is used.

6.6 Conclusion

In this chapter, signal separation of targets and sea-clutter was demonstrated using the BPD algorithm with TQWTs. Stationary and slowing moving targets are better suited to a low Q-factor TQWT while fast moving targets are better suited to a high Q-factor TQWT.

The focus of this chapter was on choosing the penalty parameter for the BPD algorithm. It was found that a high penalty parameter can reject strong interference, but at the cost of suppressing weak targets. In order to reject as much interference as possible while still detecting weak targets, we proposed a method to determine an adaptive penalty parameter which varies according to the sea-surface fluctuations across range. A simple method of choosing these penalty parameters was presented. The selection of these parameters is based on the least square error fitting between the energy ratio and the average standard deviation of

the interference. If the energy ratio is used as a detection threshold, then the choice of penalty parameter can be directly linked to the desired probability of false alarm.

A new detection scheme was then proposed based on the energy ratio after sparse signal separation. Using Monte-Carlo simulations, the detection performance of the sparse signal separation scheme offered significant improvements up to 12.75 dB over the original data when compared to a conventional CA-CFAR algorithm.

In this chapter, we only considered detection in the range / time domain. Future work could investigate a formulation in in the range / Doppler domain where further improvement may be achieved due to the coherent processing gain.

Chapter 7

Conclusion and Future Work

IN this chapter, a summary of the thesis and the main contributions are outlined. A description of future work to further improve the performance of radar detection in sea-clutter is provided.

7.1 Conclusion

The main goal of this thesis was to develop new techniques for detection of small targets in sea-clutter. For maritime radar, the main interfering component are sea-spikes which are not only strong in intensity but also vary in velocity. The challenges of detecting targets in these conditions have been outlined in Chapters 1 and 2. A review of time frequency methods was conducted and reported in Chapters 1 and 3. The stationary wavelet transform (SWT) and tuned Q-factor wavelet transform (TQWT) were selected for the different detection schemes presented in the thesis. The SWT is the shift invariant version of the discrete wavelet transform (DWT), while the TQWT is shift invariant and provides better time-frequency resolution.

Two radar data sets, outlined in Chapter 2, were used to validate the detection schemes. The first data set is collected at medium grazing angles from a moving airborne platform using the Ingara radar. The second data set was recorded by the NetRAD system.

The first detection scheme in the thesis is based on sub-band analysis using SWTs. The SWT decomposes a signal into different components (sub-bands) with each sub-band revealing different characteristics of the data. Initial analysis looked at the mean separation between the interference and the interference with an injected target. Many of the reconstructed sub-bands were then shown to have larger separation than the unprocessed data. For a stationary target, better separation was achieved in the low resolution approximate reconstructed sub-band. However, moving targets had better separation in one or multiple reconstructed detail sub-bands. The optimal choice of sub-band requires the target velocity to be known prior the detection. To overcome this problem, a sub-band indicator using an entropy metric was introduced. A heuristic scheme was then proposed to reduce the computation time and select the reconstructed sub-band with the most information about the target.

To quantify the detection improvement and robustness, Monte-Carlo simulations were implemented for the unprocessed Ingara data, the reconstructed sub-band with known target velocity and the reconstructed sub-band using the entropy metric. The detection performance using a CA-CFAR revealed that with prior knowledge of the target velocity, the improvement was between 3 and 7 dB over the unprocessed data. For the unknown target velocity case, the entropy indicator was able to successfully determine the best reconstructed sub-bands in the majority of the cases and offered similar improvement over the unfiltered data when compared to the ‘best’ reconstructed sub-band.

With the successful implementation of the SWT scheme in Chapter 4, the scheme was then applied to the data recorded with the NetRAD bistatic radar system. Both the Ingara and

NetRAD radar systems operate at different frequency bands, PRFs and grazing angles. Moreover, the data received from low and medium grazing angles contains different sea-clutter characteristics. With the NetRAD data, the Doppler width is confined to ± 50 Hz and we needed to decompose the data to lower resolutions. For analysis, the scheme was applied to 12 different sets of data from 3 different bistatic angles (60°, 90° and 120°) and included both monostatic and bistatic data with HH and VV polarisations.

The results showed that the scheme worked well with the NetRAD radar system. The highest improvement compared to the unfiltered data was found in the monostatic configuration with 20.9 dB and 35.8 dB greater SIRs for the HH and VV polarisations respectively. When analysing the improvement in relation to the bistatic angles, the results show mixed improvements with an unclear conclusion whether one operational angle is better than the others. This may be due to possible target contamination in some of the data sets.

Overall, the new SWT detection scheme works effectively for both medium and low grazing angle data sets, operated from moving and static platforms. The largest improvements for both cases were 8 dB for the Ingara data and 35.8 dB for the NetRAD data.

The final part of the thesis, Chapter 6 considered sparse signal separation using a resonance based transform. The algorithm used to perform sparse signal separation was basis pursuit denoising (BPD). The BPD algorithm requires two main factors to achieve a good separation: a selected sparse transform (or dictionary) and a regularisation (penalty) parameter. For this work, a tuned Q-factor wavelet transform (TQWT) was used based on previous studies.

The novel contribution here is an adaptive penalty parameter for the BPD algorithm. In previous work, a global penalty parameter was used for all range bins. With the adaptive scheme, the penalty parameter is uniquely set for each range bin using an estimate of the standard deviation smoothed across range.

A detection scheme was then developed using the energy ratio between the residual and estimated signal. To demonstrate and quantify the detection improvement, a Monte-Carlo simulation was implemented using the Ingara data set as a detection statistic. The scheme using both non-adaptive and adaptive penalty parameters was compared to the detection of unprocessed data. The results for the HH polarisation showed a significant improvement of 11.5 dB and 12.8 dB over the conventional processing for the non-adaptive and adaptive schemes, respectively. For VV polarisations, the improvement was 11 dB and 11.5 dB for the non-adaptive and adaptive penalty parameters.

The two detection schemes, presented in this thesis both showed great potential when tested on real radar data. The first scheme was tested with both the Ingara and NetRAD data while the second scheme was validated with the Ingara data only. The SWT detection scheme offers a significant detection improvement over a conventional detector, while the second scheme using sparse signal separation provided even further improvement.

7.2 Future Work

Detection methods based on wavelet transforms have been investigated here but there are other time-frequency transforms that have potential and were not studied. With the wavelet transforms used in this project, two schemes have been developed and tested on real radar data. However, there is still further work which can be explored to improve the detection performance of small targets in sea-clutter. Some suggested potential further investigations are listed below.

7.2.1 Sub-band Analysis Using SWTs

1. **Detection in the range-Doppler domain**
   Radar target detection can be implemented in either the range-time or range-Doppler domains. In this thesis, only range-time detection has been explored. However, further improvement in performance could be achieved in the frequency domain.

2. **Sub-band Indicator**
   The choice of a sub-band indicator when the target velocity is not known prior to the detection could be further explored. The entropy metric was proposed in this work and selects the correct sub-bands in the majority of cases. However, the indicator does not work very well when the SIR is low and there are strong sea-spikes. Therefore research into an alternative indicator is encouraged to further improve the detection performance.

3. **Choice of Wavelets**
   The SWT detection scheme was shown to have significant detection improvement for small targets. In this thesis, the Daubechies-4 wavelet was used based on previous work but a more thorough investigation is recommended to potentially improve detection performance.

7.2.2 Sparse Signal Separation Using TQWTs

With the sparse signal separation scheme, stationary and slow moving targets are better detected using low Q-factor TQWTs while fast moving targets are better detected with high Q-factor. In order to capture both stationary and moving targets, a dual Q-factor implementation could be implemented. A method which has been used to perform the dual-Q signal separation is Morphological Component Analysis (MCA) [106]. The method was previously analysed by Farshchian and Selesnick [43] and Nguyen and Al-Ashwal [77]. However, their implementations used a fixed penalty parameter. Based on the observed effectiveness of the adaptive penalty parameter, a new implementation using the dual-Q MCA technique could be investigated. Future work using this sparse signal separation method could also be implemented in the frequency domain.

Appendix A

Detection Performance Using Single Level SWTs

THIS appendix provides the detection results for all the polarisations with the single level SWT using both 1D and 2D wavelets. The results complement those included in Chapter 4.

A.1 Detection performance

An analysis of the detection performance and comparison using 1D and 2D SWTs was studied in Chapter 4 with only the results presented for the HH polarisation. The conclusion from these results is that the 1D SWT produced better detection performance than the 2D SWTs. In this appendix, the detection performance for all polarisations are presented.

Figure A.1 shows the probability of detection for the original and 1D SWT reconstructed sub-bands. Results for the stationary and moving targets are shown in the first and second columns, respectively. Figure A.2 then illustrates the required SIR using the 1D SWT detection scheme with a variation of the velocity from 0 to 4.3 m/s when measured at $P_{\mathrm{d}} = 0.5$. These results are then repeated for the 2D SWT in Figures A.3 and A.4.

Using both the 1D and 2D SWTs, the detection performance of the sub-band reconstruction scheme offers better detection performance compared to the unprocessed data. For stationary targets, the approximate reconstructed sub-bands ($\tilde{A}_1$ and $\tilde{LL}_1$) of both the 1D and 2D SWTs show the biggest improvement. Moving targets are best detected in the detail $\tilde{D}_1$ and vertical $\tilde{HL}_1$ reconstructed sub-bands. The detection improvements also vary when different polarisations are used. For the stationary target using the 1D SWT, similar improvements were observed for HV, VH and HH polarisations while the VV polarisation offered the least improvement. When using the 2D SWT, the biggest improvement is achieved in the HH polarisation followed by the VH polarisation, while the VH and VV polarisations are worse than the unprocessed data. The detection improvements are reversed for the moving target. The biggest improvements using both the 1D and 2D SWTs are found in the VV polarisation followed by HH, HV and VH.

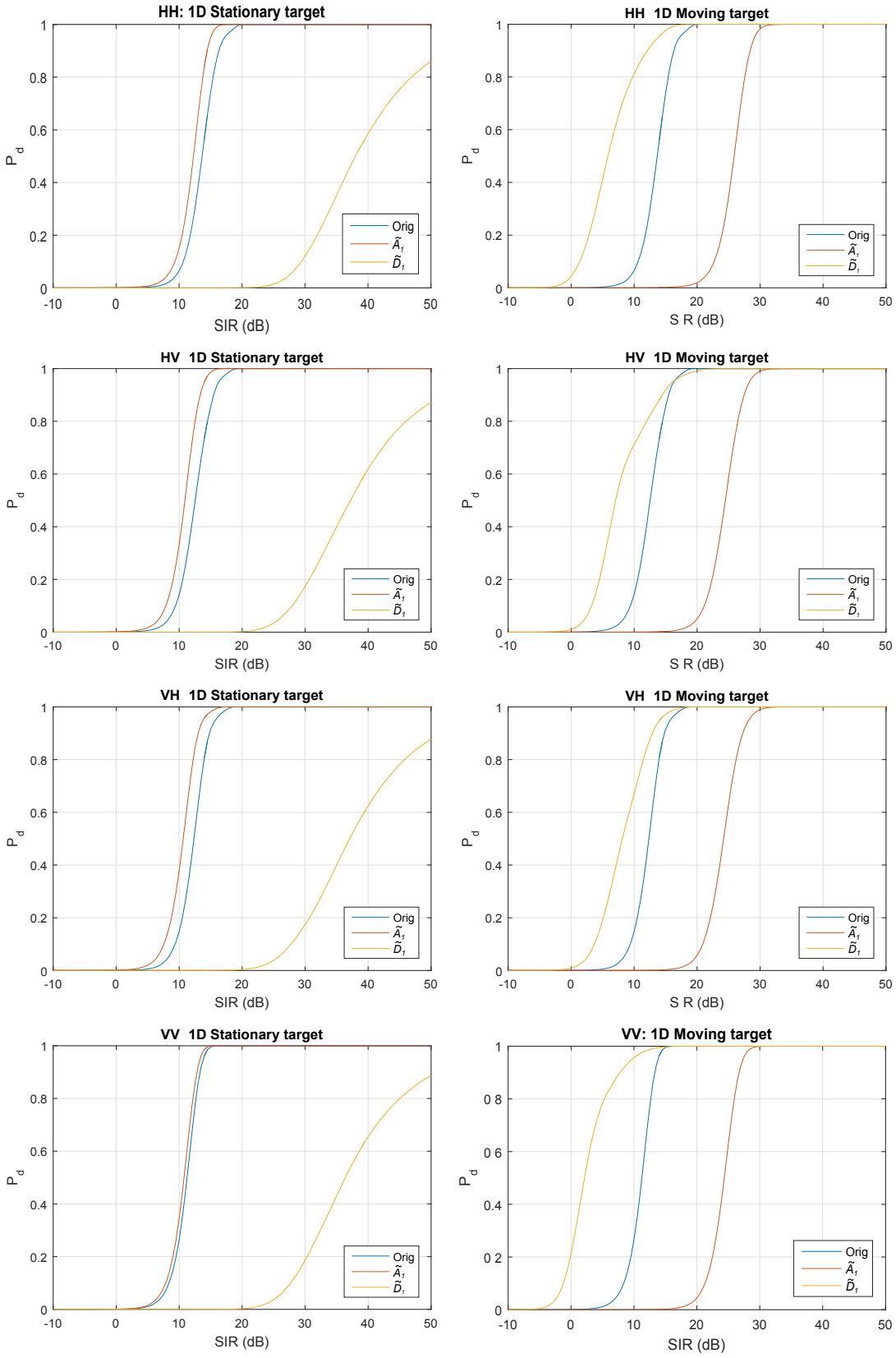

Figure A.1. The probability of detection for the original and 1D SWT reconstructed sub-bands. Results for stationary and moving targets are shown in first and second columns.

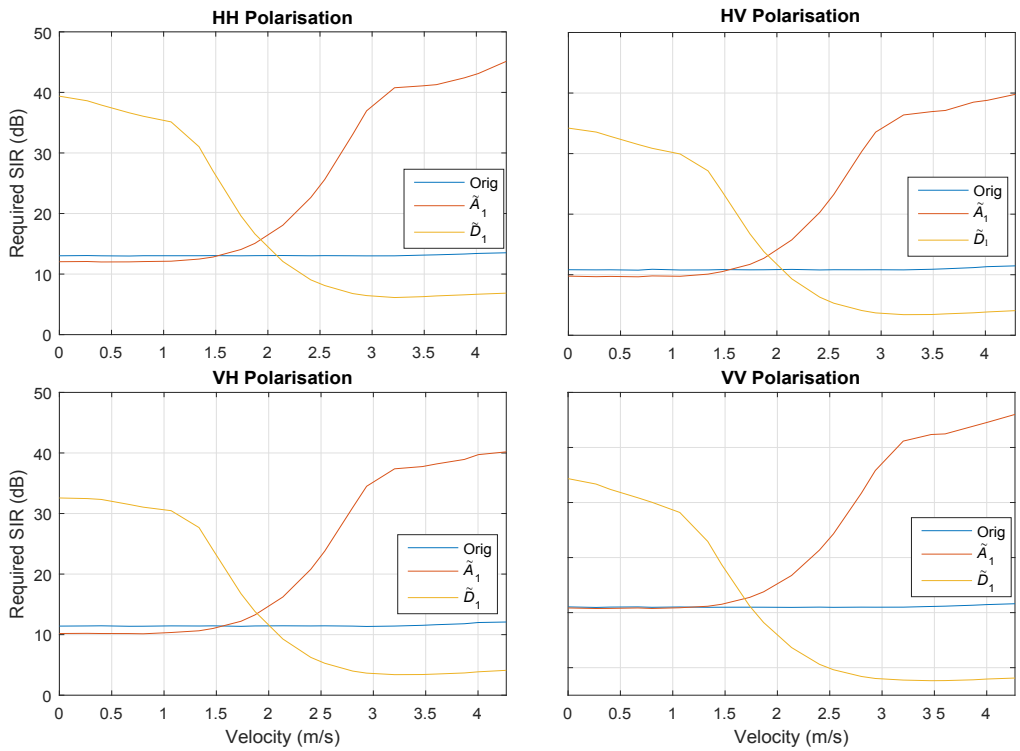

Figure A.2. Required SIR using the 1D SWT detection scheme with variation of the velocity from 0 to 4.3 m/s.

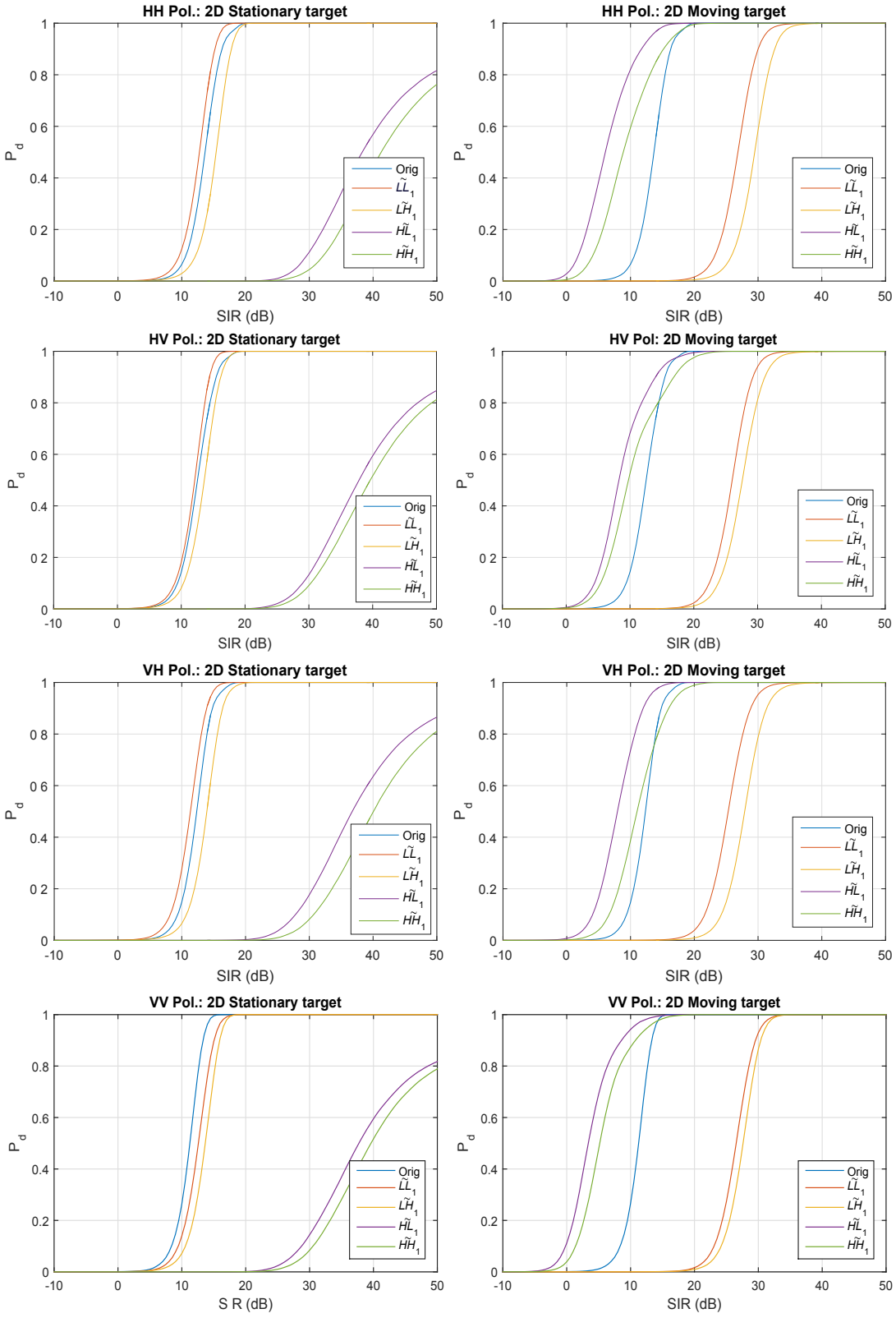

Figure A.3. The probability of detection for the original and 2D SWT reconstructed sub-bands. Results for stationary and moving targets are shown in first and second columns.

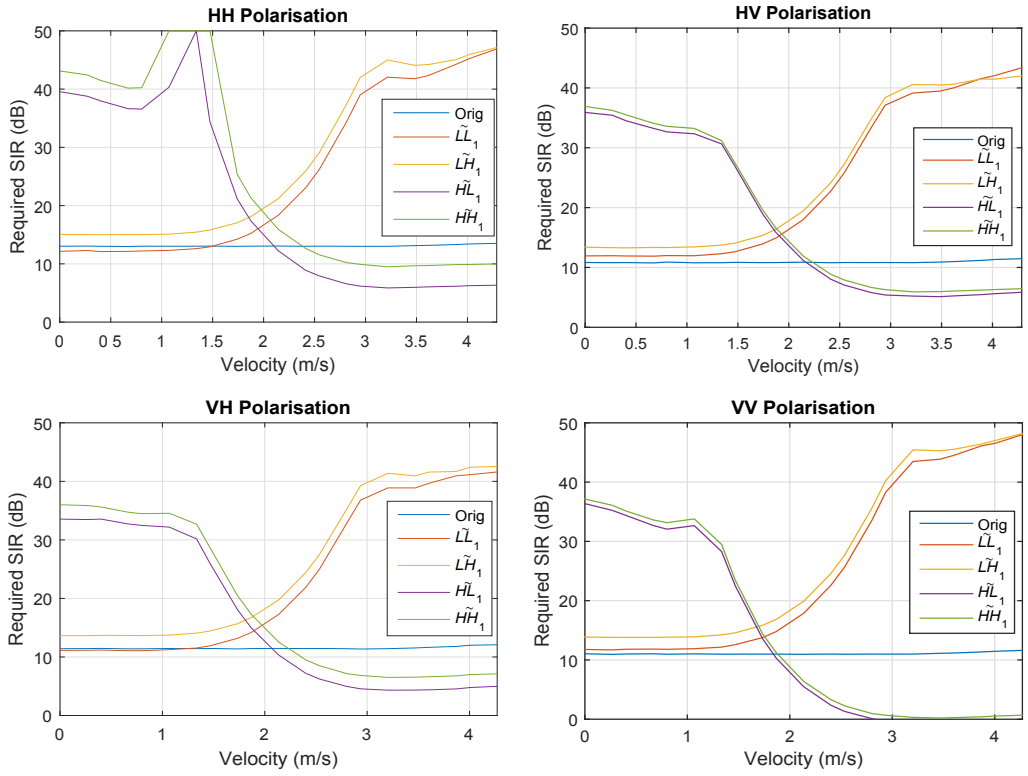

Figure A.4. Required SIR using the 2D SWT detection scheme with variation of the velocity from 0 to 4.3 m/s.

Bibliography

[1] D. A. Abraham and A. P. Lyons, "Reliable methods for estimating the K-distribution shape parameter," *IEEE Journal of Oceanic Engineering*, vol. 35, no. 2, pp. 288–302, 2010.

[2] M. V. Afonso, J. M. Bioucas-Dias, and M. A. T. Figueiredo, "Fast image recovery using variable splitting and constrained optimization," *IEEE Transactions on Image Processing*, vol. 19, no. 9, Sept 2010.

[3] N. Ahuja, S. Lertrattanapanich, and N. Bose, "Properties determining choice of mother wavelet," *IEE Proceedings on Vision, Image and Signal Processing*, vol. 152, no. 5, pp. 659–664, Oct 2005.

[4] W. Al-Ashwal, "Measurement and modelling of bistatic sea clutter," Ph.D. dissertation, University College London, 2011.

[5] W. A. Al-Ashwal, K. Woodbridge, and H. D. Griffiths, "Analysis of bistatic sea clutter-part I: Average reflectivity," *IEEE Transactions on Aerospace and Electronic Systems*, vol. 50, no. 2, pp. 1283–1292, 2014.

[6] ——, "Analysis of bistatic sea clutter-part II: Amplitude statistics," *IEEE Transactions on Aerospace and Electronic Systems*, vol. 50, no. 2, pp. 1293–1303, 2014.

[7] M. G. Amin, Y. D. Zhang, F. Ahmad, and K. D. Ho, "Radar signal processing for elderly fall detection: The future for in-home monitoring," *IEEE Signal Processing Magazine*, vol. 33, no. 2, pp. 71–80, 2016.

[8] L. Anitori, A. Maleki, M. Otten, R. G. Baraniuk, and P. Hoogeboom, "Design and analysis of compressed sensing radar detectors," *IEEE Transactions on Signal Processing*, vol. 61, no. 4, pp. 813–827, Feb 2013.

[9] J. E. Ball and A. Tolley, "Low SNR radar signal detection using the continuous wavelet transform (CWT) and a Morlet wavelet," in *Radar Conference*, May 2008, pp. 1–6.

[10] I. Bayram and I. W. Selesnick, "Overcomplete discrete wavelet transforms with rational dilation factors," *IEEE Transactions on Signal Processing*, vol. 57, no. 1, pp. 131–145, 2009.

[11] A. Beck and M. Teboulle, "A fast iterative shrinkage-thresholding algorithm for linear inverse problems," *SIAM Journal on Imaging Sciences*, vol. 2, pp. 183–202, Mar. 2009.

[12] F. Berizzi and E. Dalle-Mese, "Fractal analysis of the signal scattered from the sea surface," *IEEE Transactions on Antennas and Propagation*, vol. 47, no. 2, pp. 324–338, Feb 1999.

[13] F. Berizzi and E. Dalle Mese, "Scattering coefficient evaluation from a two-dimensional sea fractal surface," *IEEE Transactions on Antennas and Propagation*, vol. 50, no. 4, pp. 426–434, Apr 2002.

[14] F. Berizzi and E. Dalle-Mese, "Scattering from a 2D sea fractal surface: fractal analysis of the scattered signal," *IEEE Transactions on Antennas and Propagation*, vol. 50, no. 7, pp. 912–925, Jul 2002.

[15] S. Bocquet, "Parameter estimation for Pareto and K distributed clutter with noise," *IET Radar Sonar and Navigation*, vol. 9, no. 1, pp. 104–113, 2015.

[16] S. Bocquet, L. Rosenberg, and S. Watts, "Simulation of coherent sea clutter with inverse gamma texture," in *International Radar Conference*, October 2014.

[17] S. Boyd and L. Vandenberghe, *Convex Optimization*. New York, USA: Cambridge University Press, 2004.

[18] J. N. Briggs, *Target Detection by Marine Radar*. The Institution of Electrical Engineers, 2004.

[19] C. S. Burrus, R. A. Gopinath, and H. Guo, *Introduction to Wavelets and Wavelet Transforms: A Primer*. Prentice Hall, 1997.

[20] G. Calvagno, M. Ermani, R. Rinaldo, and F. Sartoretto, "A multiresolution approach to spike detection in EEG," in *IEEE International Conference on Acoustics, Speech, and Signal Processing*, vol. 6, 2000, pp. 3582–3585 vol.6.

[21] E. J. Candes and T. Tao, "Near-optimal signal recovery from random projections: Universal encoding strategies," *IEEE Transactions on Information Theory*, vol. 52, no. 12, pp. 5406–5425, 2006.

[22] S. S. Chen, D. L. Donoho, and M. A. Saunders, "Atomic decomposition by basis pursuit," *SIAM Review*, vol. 43, pp. 129–159, Jan. 2001.

[23] V. Chen and H. Ling, *Time-frequency Transforms for Radar Imaging and Signal Analysis*. Artech House, 2002.

[24] T. M. Cover and J. A. Thomas, *Elements of Information Theory*. Wiley-Interscience, 2006, Wiley Series in Telecommunications and Signal Processing.

[25] D. J. Crisp, M. Preiss, and A. S. Goh, "Ingara medium-high incidence angle polarimetric sea clutter measurements and analysis for the MAST'06 trial," Defence Science and Technology Organisation, Technical Report, 2008.

[26] I. Daubechies, "The wavelet transform, time-frequency localization and signal analysis," *IEEE Transactions on Information Theory*, vol. 36, no. 5, pp. 961–1005, 1990.

[27] ——, *Ten Lectures on Wavelets*, ser. CBMS-NSF. Siam, 1992.

[28] G. Davidson, "Doppler filtering and detection strategies for multifunction radar," Ph.D. dissertation, Univeristy College London, 2000.

[29] G. Davidson and H. D. Griffiths, "Wavelet detection of low observable targets within sea-clutter," in *International Radar Conference*, 2002.

[30] A. De Maio and M. S. Greco, Eds., *Modern Radar Detection Theory*. SciTech, 2016.

[31] Y. Dong, "Distribution of X-band high resolution and high grazing angle sea clutter," Defence Science and Technology Organisation, Research Report DSTO-RR-0316, 2006.

[32] D. L. Donoho, "Compressed sensing," *IEEE Transactions on Information Theory*, vol. 52, no. 4, pp. 1289–1306, 2006.

[33] D. L. Donoho, A. Maleki, and A. Montanari, "Message passing algorithms for compressed sensing," *Computing Research Repository*, 2009.

[34] M. Duarte, M. Davenport, M. Wakin, and R. Baraniuk, "Sparse signal detection from incoherent projections," in *IEEE International Conference on Acoustics, Speech and Signal Processing*, vol. 3, May 2006, p. III.

[35] V. Duk, B. Ng, and L. Rosenberg, "The potential of 2D wavelet transforms for target detection in sea-clutter," in *IEEE Radar Conference*, May 2015, pp. 0901–0906.

[36] V. Duk, L. Rosenberg, and B. Ng, "Adaptive regularisation for radar sea clutter signal separation using a sparse-based method," in *International Radar Conference*, Oct. 2017.

[37] V. Duk, L. Rosenberg, and B. W. H. Ng, "Target detection in sea-clutter using stationary wavelet transforms," *IEEE Transactions on Aerospace and Electronic Systems*, vol. 53, no. 3, pp. 1136–1146, June 2017.

[38] J. R. Duncan, W. C. Keller, and J. W. Wright, "Fetch and wind speed dependence of Doppler spectra," *Radio Science*, vol. 9, pp. 809–819, 1974.

[39] N. Ehara, I. Sasase, and S. Mori, "Weak radar signal detection based on wavelet transform," in *IEEE International Conference on Acoustics, Speech, and Signal Processing*, vol. 2, Apr 1994, pp. II/377–II/380.

[40] M. Elad, *Sparse and Redundant Representations: From Theory to Applications in Signal and Image Processing*, 1st ed. Springer Publishing Company, 2010.

[41] M. Farshchian, "Target extraction and imaging of maritime targets in the sea clutter spectrum using sparse separation," *IEEE Geoscience and Remote Sensing Letters*, vol. 14, no. 2, pp. 232–236, Feb 2017.

[42] M. Farshchian and F. L. Posner, "The Pareto distribution for low grazing angle and high resolution X-band sea clutter," in *IEEE Radar Conference*, 2010, pp. 789–793.

[43] M. Farshchian and I. Selesnick, "Application of a sparse time-frequency technique for target with oscillatory fluctuations," in *International Waveform and Diversity Conference*, January 2012, pp. 191–196.

[44] F. Fay, J. Clarke, and R. Peters, "Weibull distribution applied to sea clutter," *IEE Radar Conference*, pp. 101–103, 1977.

[45] F. Fioranelli, M. Ritchie, H. Griffiths, S. Sandenbergh, and M. Inggs, "Analysis of polarimetric bistatic sea clutter using the NetRAD radar system," *IET Radar, Sonar & Navigation*, vol. 10, pp. 1356–1366(10), October 2016.

[46] D. Gabor, "Theory of communication," *IEE*, vol. 93, pp. 429–441, November 1946.

[47] H. Griffiths, W. Al-Ashwal, K. Ward, R. Tough, C. Baker, and K. Woodbridge, "Measurement and modelling of bistatic radar sea clutter," *IET Radar, Sonar & Navigation*, vol. 4, no. 2, pp. 280–292, 2010.

[48] N. W. Guinard and J. C. Daley, "An experimental study of a sea clutter model," *Proceedings of the IEEE*, vol. 58, pp. 543–550, 1970.

[49] R. Guo, M. Hao, M. Li, Y. Ni, and Z. Cheng, "Small targets detection in low resolution sea clutter," in *Asia-Pacific Microwave Conference*, Dec 2008, pp. 1–4.

[50] B. Harris, "Entropy," *John Wiley and Sons, Inc*, 2006.

[51] P. K. Hughes, "A high-resolution radar detection strategy," *IEEE Transactions on Aerospace and Electronic Systems*, vol. 19, no. 5, pp. 663–667, Sept 1983.

[52] E. Jakeman and P. N. Pusey, "Significance of K distributions in scattering experiments," *Physical Review Letters*, vol. 40, pp. 546–550, Feb 1978.

[53] F. Jangal, S. Saillant, and M. Helier, "Wavelet contribution to remote sensing of the sea and target detection for a high-frequency surface wave radar," *IEEE Geoscience and Remote Sensing Letters*, vol. 5, no. 3, pp. 552–556, July 2008.

[54] A. T. Jessup, W. K. Melville, and W. C. Keller, "Breaking waves affecting microwave backscatter, 1. detection and verification," *Journal of Geophysical Research*, vol. 96, no. C11, pp. 20,547–20,559, November 1991.

[55] S. Jia and L. Kong, "A new approach to range spread target detection based on information entropy," in *2nd Asian-Pacific Conference on Synthetic Aperture Radar*, Oct 2009, pp. 560–562.

[56] I. Joughin, D. Percival, and D. Winebrenner, "Maximum likelihood estimation of K distribution parameters for SAR data," *IEEE Transactions on Geoscience and Remote Sensing*, vol. 31, no. 5, pp. 989–999, Sep 1993.

[57] P. Karsmakers, T. Croonenborghs, M. Mercuri, D. Schreurs, and P. Leroux, "Automatic in-door fall detection based on microwave radar measurements," in *European Radar Conference*. IEEE, 2012, pp. 202–205.

[58] J. D. Klein, "Calibration of complex polarimetric SAR imagery using backscatter correlation," *IEEE Transactions on Aeronautical and Electronics Systems*, vol. 28, January 1992.

[59] E. Knott, J. Shaeffer, and M. Tuley, *Radar Cross Section*, ser. SciTech radar and defense series. Institution of Engineering and Technology, 2004.

[60] P. H. Y. Lee, J. D. Barter, K. L. Beach, C. L. Hindman, B. M. Lake, H. Rungaldier, J. C. Shelton, A. B. Williams, R. Yee, and H. C. Yuen, "X-band microwave backscattering from ocean waves," *Journal of Geophysical Research*, vol. 100, no. C2, pp. 2591–2611, 1995.

[61] P. H. Y. Lee, J. D. Barter, E. Caponi, C. L. Hidman, B. M. Lake, H. Rungaldier, and J. C. Shelton, "Power spectral lineshapes of microwave radiation backscattered from sea surfaces at small grazing angles," *IEE Proceedings of Radar, Sonar and Navigation*, vol. 142, no. 5, pp. 252–258, 1995.

[62] R. W. Lindsay, D. B. Percival, and D. A. Rothrock, "The discrete wavelet transform and the scale analysis of the surface properties of sea ice," *IEEE Transactions on Geoscience and Remote Sensing*, vol. 34, no. 3, pp. 771–787, May 1996.

[63] T. Lo, H. Leung, J. Litva, and S. Haykin, "Fractal characterisation of sea-scattered signals and detection of sea-surface targets," *IEE Proceedings on Radar and Signal Processing*, vol. 140, no. 4, pp. 243–250, Aug 1993.

[64] M. W. Long, *Radar Reflectivity of Land and Sea - Third Edition*. Artech House, 2001.

[65] J. Mairal, F. Bach, and J. Ponce, *Sparse Modeling for Image and Vision Processing*. Foundations and trends in computer graphics and vision, 2014.

[66] A. Maleki, L. Anitori, Z. Yang, and R. G. Baraniuk, "Asymptotic analysis of complex LASSO via complex approximate message passing (CAMP)," *Computing Research Repository*, 2011. [Online]. Available: http://arxiv.org/abs/1108.0477

[67] S. G. Mallat, "A theory for multiresolution signal decomposition: the wavelet representation," *IEEE Transactions on Pattern Analysis and Machine Intelligence*, vol. 11, no. 7, pp. 674–693, 1989.

[68] S. Mallat, *A Wavelet Tour of Signal Processing*, 2nd ed., ser. Electronics & Electrical. Academic Press, 1999.

[69] M. Martorella, F. Berizzi, and E. Dalle Mese, "On the fractal dimension of sea surface backscattered signal at low grazing angle," *IEEE Transactions on Antennas and Propagation*, vol. 52, no. 5, pp. 1193–1204, May 2004.

[70] A. Mertins, *Wavelet Transform*. John Wiley & Sons, Ltd, 2001. [Online]. Available: http://dx.doi.org/10.1002/0470841834.ch8

[71] D. Meyer and H. Mayer, *Radar target detection: handbook of theory and practice*. Academic Press, 1973.

[72] Y. Meyer, "Orthonormal wavelets," in *Wavelets. Time-Frequency Methods and Phase Space*, J.-M. Combes, A. Grossmann, and P. Tchamitchian, Eds., 1989, p. 21.

[73] D. Middleton, "New physical-statistical methods and models for clutter and reverberation: the KA-distribution and related probability structures," *IEEE Journal of Oceanic Engineering*, vol. 24, no. 3, pp. 261–284, Jul 1999.

[74] G. P. Nason and B. W. Silverman, "The stationary wavelet transform and some statistical applications," in *Wavelets and Statistics*. Springer-Verlag, 1995, pp. 281–300.

[75] B. Ng, L. Rosenberg, and S. T. N. Nguyen, "Target detection in sea clutter using resonance based signal decomposition," in *IEEE Radar Conference*, 2016.

[76] N. S. T. Nguyen, "Design of bi-orthogonal rational discrete wavelet transform and the associated applications," Ph.D. dissertation, University of Adelaide, 2014.

[77] S. Nguyen and W. Al-Ashwal, "Sea clutter mitigation using resonance-based signal decomposition," *IEEE Geoscience and Remote Sensing Letters*, vol. 12, no. 11, pp. 2257–2261, Nov 2015.

[78] R. Palamà, M. Greco, and F. Gini, "Multistatic CFAR detection in non-Gaussian clutter," in *IEEE Radar Conference*, 2016.

[79] R. Pathak, *The Wavelet Transform*. Atlantis Press/World Scientific, 2009, vol. 6.

[80] J. Pesquet, H. Krim, and H. Carfantan, "Time-invariant orthonormal wavelet representations," *IEEE Transactions on Signal Processing*, vol. 44, no. 8, pp. 1964–1970, Aug 1996.

[81] P. Piotr and L. Agnieszka, "The Haar-wavelet transform in digital image processing: Its status and achievements," *Machine Graphics & Vision*, 2004.

[82] S. Quegan, "Unified algorithm for phase and cross-talk calibration of polarimetric data: Theory and observations," *IEEE Transactions on Geoscience and Remote Sensing*, vol. 32, no. 1, pp. 89–99, 1994.

[83] M. Rangaswamy, J. H. Michels, and B. Himed, "Statistical analysis of the non-homogeneity detector for STAP applications," *Digital Signal Processing*, vol. 14, no. 3, pp. 253 – 267, 2004.

[84] M. A. Richards, *Fundamentals of Radar Signal Processing*. The McGraw Hill Companies Inc, USA, 2005.

[85] M. Ritchie, W. Al-Ashwal, A. Stove, K. Woodbridge, and H. Griffiths, "Coherent analysis of horizontally-polarized monostatic and bistatic sea clutter," in *IET International Conference on Radar Systems*, 2012.

[86] M. Ritchie, A. Stove, A. Woodbridge, and H. Griffiths, "NetRAD: Monostatic and bistatic sea clutter texture and Doppler spectra characterization at S-band," *IEEE Transactions on Geoscience and Remote Sensing*, vol. 54, no. 9, pp. s 5533–5543, September 2016.

[87] L. Rosenberg, "Sea-spike detection in high grazing angle X-band sea-clutter," *IEEE Transactions on Geoscience and Remote Sensing*, vol. 51, no. 8, pp. 4556–4562, 2013.

[88] ——, "Coherent detection with non-stationary high grazing angle X-band sea-clutter," in *European Radar Conference*, 2014.

[89] L. Rosenberg and S. Bocquet, "The Pareto distribution for high grazing angle sea-clutter," in *IEEE Proceedings on Geoscience and Remote Sensing*, 2013, pp. 4209–4212.

[90] ——, "Radar detection performance in medium grazing angle X-band sea-clutter," Defence Science and Technology Group, Technical Report DST-Group-TR-3193, December 2015.

[91] L. Rosenberg, D. J. Crisp, and N. J. Stacy, "Analysis of the KK-distribution with medium grazing angle sea-clutter," *IET Proceedings of Radar Sonar and Navigation*, vol. 4, no. 2, pp. 209–222, April 2010.

[92] L. Rosenberg and S. Watts, "Model based coherent detection in medium grazing angle sea-clutter," in *IEEE Radar Conference*, 2016.

[93] L. Rosenberg, S. Watts, and S. Bocquet, "Application of the K+Rayleigh distribution to high grazing angle sea-clutter," in *International Radar Conference*, vol. 36, no. 5, France, 2014, pp. 961–1005.

[94] L. Rosenberg and S. Watts, "High grazing angle sea-clutter literature review," Defence Science and Technology Organisation, Technical Report DSTO-GD-0736, March 2013.

[95] J. S. Sandenbergh and M. R. Inggs, "A common view GPSDO to synchronize netted radar," in *IET International Conference on Radar Systems*, Oct 2007, pp. 1–5.

[96] J. S. Sandenbergh, M. R. Inggs, and W. A. Al-Ashwal, "Evaluation of coherent netted radar carrier stability while synchronised with GPS-disciplined oscillators," in *IEEE Radar Conference*, May 2011, pp. 1100–1105.

[97] L. R. Sbastien Angelliaume and M. Ritchie, "Modelling the amplitude distribution of radar sea clutter," 2018.

[98] M. Schmidt, "Least squares optimization with L1-norm regularization," 2005. [Online]. Available: http://citeseerx.ist.psu.edu/viewdoc/summary?doi=10.1.1.186.3602

[99] I. W. Selesnick, "Resonance-based signal decomposition: A new sparsity-enabled signal analysis method," *Signal Processing*, vol. 91, no. 12, pp. 2793–2809, 2011.

[100] ——, "Wavelet transform with tunable Q-factor," *IEEE Transactions on Signal Processing*, vol. 59, no. 8, pp. 3560–3575, aug. 2011.

[101] ——, "Introduction to sparsity in signal processing," *Connetions*, May 27 2012.

[102] C. Shannon, "A mathematical theory of communication," *Bell System Technical Journal*, vol. 27, 1948.

[103] D. A. Shnidman, "Radar detection probabilities and their calculation," *IEEE Transactions on Aerospace and Electronic Systems*, vol. 31, no. 3, pp. 928–950, 1995.

[104] M. I. Skolnik, *Radar Handbook*, 3rd ed. McGraw-Hill, 2008.

[105] J.-L. Starck, J. Fadili, and F. Murtagh, "The undecimated wavelet decomposition and its reconstruction," *IEEE Transactions on Image Processing*, vol. 16, no. 2, pp. 297–309, Feb 2007.

[106] J.-L. Starck, Y. Moudden, J. Bobin, M. Elad, and D. Donoho, "Morphological component analysis," in *Optics & Photonics*. International Society for Optics and Photonics, 2005, pp. 59 140Q–59 140Q.

[107] G. W. Stimpson, *Introduction to Airborne Radar*, 2nd ed. SciTech Publishing, 1998.

[108] G. Strang and T. Nguyen, *Wavelets and Filter banks*. Wellesley, MA: Wellesley-Cambridge, 1996.

[109] P. Swerling, "Probability of detection for fluctuating targets," *IEEE Transactions on Information Theory*, vol. IT-6, pp. 269–308, 1960.

[110] R. Tibshirani, "Regression shrinkage and selection via the LASSO," *Journal of the Royal Statistical Society, Series B*, vol. 58, pp. 267–288, 1994.

[111] C. Torrence and G. P. Compo, "A practical guide to wavelet analysis," *Bulletin of the American Meteorological Society*, vol. 79, pp. 61–78, 1998.

[112] J. Torres, P. Cabiscol, and J. Grau, "Radar chirp detection through wavelet transform," in *Proceedings of the 5th Biannual World Congress on Automation*, vol. 13, 2002, pp. 227–232.

[113] G. Trunk and S. F. George, "Detection of targets in non-Gaussian sea clutter," *IEEE Transactions on Aerospace and Electronic Systems*, vol. AES-6, no. 5, pp. 620–628, Sept 1970.

[114] S. Tugac and M. Efe, "Continuous wavelet transform and hidden Markov model based target detection," *Radio Engineering*, vol. 23, no. 1, pp. 96–103, April 2014.

[115] G. R. Valenzuela and M. B. Laing, "Study of Doppler spectra of radar sea echo," *Journal of Geophysical Research*, vol. 75, pp. 551–563, 1970.

[116] G. R. Valenzuela, M. B. Laing, and J. C. Daley, "Ocean spectra for the high-frequency waves as determined from airborne radar measurements," *Journal of Marine Research*, vol. 29, pp. 69–84, 1971.

[117] M. Vetterli and C. Herley, "Wavelets and filter banks: theory and design," *IEEE Transactions on Signal Processing*, vol. 40, no. 9, pp. 2207–2232, Sep 1992.

[118] J. Ville, "Theorie et Applications de la Notion de Signal Analytique," *Cables et Transmission*, vol. 1, pp. 61–74, 1948.

[119] D. Walker, "Doppler modelling of radar sea clutter," *IEE Proceedings of Radar, Sonar and Navigation*, vol. 148, no. 2, pp. 73–80, April 2001.

[120] K. F. Wallis, "A note on the calculation of entropy from histograms," *Review Literature And Arts Of The Americas*, October 2006.

[121] N. Wang, Y. Zhang, and S. Wu, "Radar waveform design and target detection using wavelets," in *CIE International Conference on Radar*, China, 2001, pp. 506–509.

[122] X. Wang, J. Liu, and H. Liu, "Small target detection in sea clutter based on Doppler spectrum features," in *CIE International Conference on Radar*, Oct 2006, pp. 1–4.

[123] K. D. Ward, "Compound representation of high resolution sea clutter," *Electronic Letters*, vol. 17, no. 16, pp. 561–563, 1981.

[124] K. D. Ward, R. J. A. Tough, and S. Watts, *Sea Clutter: Scattering, the K-Distribution and Radar Performance*, 2nd ed. The Institute of Engineering Technology, 2013.

[125] S. Watts, "The performance of cell-averaging CFAR systems in sea clutter," in *International Radar Conference*, 2000, pp. 398–403.

[126] ——, "Modeling and simulation of coherent sea clutter," *IEEE Transactions on Aerospace and Electronic Systems*, vol. 48, no. 4, pp. 3303–3317, October 2012.

[127] S. Watts, L. Rosenberg, and M. Ritchie, "Characterising the Doppler spectra of high grazing angle sea clutter," in *International Radar Conference*, 2014.

[128] B. O. Werle, "Sea backscatter, spikes and wave group observations at low grazing angles," in *IEEE International Radar Conference*, 1995, pp. 187–195.

[129] M. V. Wickerhauser, *Adapted wavelet analysis from theory to software.*, ser. Ak Peters Series. Taylor & Francis, 1994.

[130] E. Wigner, "On the quantum correction for thermodynamic equilibrium," *Physical Review*, vol. 40, pp. 749–759, Jun 1932.

[131] World Meteorlogical Organization, "Guide to wave analysis and forecasting," Technical Report WMO-No.702, 1998.

[132] J. W. Wright, "A new model for sea clutter," *IEEE Transactions on Antennas and Propagation*, vol. 16, no. 2, pp. 217–223, 1968.

[133] S. Zhang, J. Fan, L. Shou, and J. Dong, "A detection method of radar signal by wavelet transforms," in *Fourth International Conference on Fuzzy Systems and Knowledge Discovery*, vol. 2, Aug 2007, pp. 710–714.